공학박사학위논문

직교류 내 고체입자 포함 제트 유동에서의 입자 분산에 대한 실험연구

Experimental study on the particle dispersion in a particle-laden jet with a crossflow

2023년 8월

서울대학교 대학원
기계항공공학부
박주연

직교류 내 고체입자 포함 제트 유동에서의 입자 분산에 대한 실험연구

Experimental study on the particle dispersion in a particle-laden jet with a crossflow

지도교수 박 형 민

이 논문을 공학박사 학위논문으로 제출함

2023년 4월

서울대학교 대학원
기계항공공학부
박 주 연

박주연의 공학박사 학위논문을 인준함

2023년 6월

위 원 장: 김 호 영 (Signature)
부위원장: 박 형 민 (Signature)
위 원: 황 원 태 (Signature)
위 원: 고 한 서 (Signature)
위 원: 유 재 영 (Signature)

Experimental study on the particle dispersion in a particle-laden jet with a crossflow

Jooyeon Park, Doctor of Philisophy
Mechanical and Aerospace Engineering
Seoul National University, 2023

Advisor: Prof. Hyungmin Park

Abstract

A particle-laden jet with a crossflow is a common phenomenon in industrial sites, such as manufacturing facilities, and in nature, such as volcanoes and fires. Since complex vortex structures are generated in the jet with crossflow, an understanding of the mechanisms of solid particle dispersion by these vortex structures is applicable to lots of different types of flow structures. In the present study, particle dispersions (concentrations) through vortical interactions are experimentally investigated for a particle-laden upward jet, with a horizontal crossflow covering a vertical range partially near the jet exit (Reynolds numbers of 1170–5550). In summary, this paper consists of a comprehensive analysis of the 'interaction between solid particles and air flow', including 1) various solid particle

dispersion patterns occurring in the particle-laden jet with crossflow, and 2) a methodology for changing particle behavior based on the mist droplet content in the flow. Firstly, solid particle dispersion patterns and dispersion mechanisms were observed for various flow velocity ratios (jet/crossflow = R = 1.0 - 3.5) and particle Stokes numbers (St = 0.01 - 27.42). Without crossflow, there is no dominant vortical structure along the horizontal direction; thus, the particles are not dispersed significantly out of the jet core in most cases. With crossflow, on the other hand, counter-rotating vortex pairs appear above the jet exit and become stronger as the velocity ratio decreases. The smaller R increases the magnitude of the drag force exerted on the particles by the CVP, and especially for very small particles with St less than 1, this drag force is the most important factor in particle behavior. Therefore, during the period of CVP development, a large amount of particles are dispersed out of the jet center by the CVP. When St is close to 1, the particles are kept inside the CVP (especially in the jet center) by a change in drag direction. The observed dispersion patterns for various Stokes numbers and R were finally categorized into three regimes, and the dispersion mechanisms were extended to empirical particle dispersion models. Following this study, we experimentally observed the changes in particle dispersion patterns that occur when particles with $St < 1$ interact with mist droplets in the air. In these experiments, the changes in the behavior of hydrophilic (Si) and hydrophobic (PTFE) particles were analyzed for different mist droplet volume fraction conditions (0%, 0.014% & 0.03%) in the crossflow. For R = 2.85, both Si and PTFE particles always exhibited constant behavior regardless of the amount of mist droplets. This is because at high velocity ratio flow, the less entrainment crossflow into the jet causes weak CVP, which significantly reduces the probability of particles interacting with mist droplets. On the other hand, for R = 1.1, when the mist droplet fraction in the flow is the highest, Si particles are preferentially concentrated at the center of the jet, increasing the amount of particles dispersed to

distant locations. This occurs because the interaction between the particles and the droplets causes the particles to be dragged towards the center of the jet, so they disperse very little outside the CVP. The PTFE particles were not affected by the mist droplets even at low *R* flow.

Keyword : particle-laden jet, crossflow, vortical structure, Stokes number, velocity ratio, humidity
Student Number : 2017-24246

To my family for their love and support

Table of Contents

List of Tables

List of Figures

Nomenclature

Roman letters:

a, b	Coefficient of the fitting equation (model)
B	Jet decay constant
*C**	Correction constant for PN
C_D	Drag coefficient
$\bar{c}_p$	Time-averaged pressure coefficient
D	Square jet pipe effective diameter (a side length)
D/Dt	Material derivative
$\bar{d}_p$	Mean solid particle diameter
F_A	Added mass force
F_B	Basset history force
F_{FA}	Fluid acceleration force
F_{Drag}	Drag force
F_G	Gravitational force
F_{LM}	Magnus lift force
F_{LS}	Saffman lift force
G_1	Backward differential value of $\hat{\theta}_m$ at the P_d
G_2	Forward differential value of $\hat{\theta}_m$ at the P_d

g	Gravitational acceleration
L	Jet pipe length
M	Magnification factor
m_f	Mass of the fluid (gas) corresponding to a particle volume
m_p	Mass of a particle
n	The coordinate in the axis perpendicular s-axis
n_p	The coordinate in the axis perpendicular s_p-axis
P_d	Division point
P_o	Position where the particle out-of-(center)plane movement occurs
p_{cr}	Pressure at the crossflow free stream
$\bar{p}$	Time-averaged pressure field of the airflow
Q	Jet flux ($Q = \int_{N_j} \bar{u}(s,n)\, dn$)
R	Flow velocity ratio ($R = U_j/U_{cr}$)
Re_D	Reynolds number of the flow based on jet pipe diameter ($Re_D = \bar{u}_m D/\nu$)
Re_p	Particle Reynolds number ($Re_p = \rho_p \bar{d}_p \lvert v - u \rvert/\mu$)
R_{crit}	Critical velocity ratio
S_{laser}	Laser light intensity value of each IW
S_{md}	Median value of S_{laser}
St	Stokes number ($St = \tau_p/\tau_f$)

s	Jet centerline length from the jet origin (a coordinate in jet centerline)
s_p	local particle concentration maxima line length from the jet origin (a coordinate in the concentration maxima line)
U_j	Jet bulk velocity
U_{cr}	Crossflow bulk velocity
u	Airflow velocity
u_{cr}	Airflow velocity at the crossflow free stream
u'	Airflow velocity fluctuation
$u'_{z,c_{rms}}$	Vertical velocity fluctuation of airflow along the jet centerline
$\bar{u}_m$	Time-averaged maximum airflow velocity
$\bar{u}_{z,c}$,$\bar{u}_{x,c}$	Time-averaged vertical and horizontal velocity along the jet centerline
$\bar{u}_{zo,c}$	Time-averaged vertical velocity along the jet centerline at the jet origin
$\bar{V}_{flux}$	Crossflow volume flux near the fan outlet
V_j	Bulk particle velocity measured at the jet exit
V_s	Particle settling velocity
v	Particle velocity
v'	Particle velocity fluctuation
$\bar{v}_{exit}$	Time-averaged local particle velocity near the jet exit
x,y,z	Horizontal, transverse and vertical direction, respectively

Greek letters:

Δs	Particle displacement during Δt
Δt	Time interval between successive images
$\Delta\hat{\Theta}$	Concentration discrepancy
Θ	Particle concentration
Θ_l	Mist droplet concentration
Θ_{cc}	Corrected particle concentration ($\Theta_{cc} = \Theta * C^*$)
$\Theta_{l,cc}$	Corrected mist droplet concentration ($\Theta_{l,cc} = \Theta_l * C^*$)
$\bar{\Theta}_b$	Bulk concentration by time-averaged concentration field
$\bar{\Theta}_{exit}$	Time-averaged local concentration near the jet exit
$\hat{\Theta}$	Non-dimensional particle concentration ($\hat{\Theta} = \bar{\Theta}_{cc}/\bar{\Theta}_b$)
$\hat{\Theta}_m$	Local maximum concentration along the jet centerline at the side-view
$\bar{\Phi}_b$	Target bulk crossflow droplet volume fraction at the crossflow outlet
Ψ	CVP strength ($\Psi = \int_A \lvert\bar{\omega}_z^*\rvert\, dA$)
Ω_p	Particle rotation velocity
Ω_r	Relative rotation between the particle and fluid
δ	Percentage errors for PIV
μ	Dynamic viscosity of air
ν	Kinematics viscosity of air

ρ_g	Gas (air) density
ρ_p	Particle density
σ_n	Local standard deviation $\hat{\Theta}$ profile along the *n*-axis
σ_y	Local standard deviation $\hat{\Theta}$ profile along the *y*-axis
τ_f	Background flow characteristic time scale
τ_p	Particle relaxation time scale
ϕ	Particle volume fraction
ω	Airflow vorticity
$\bar{\omega}_y^*$	Time-averaged transverse vortical structure
$\bar{\omega}_z^*$	Time-averaged vertical vortical structure
∇	Spatial-gradient

Superscripts

$(\bar{\ })$	Time-averaged data
$(\hat{\ })$	Normalization
$(\ \ '')$	Non-dimensional force term

Abbreviations:

BD	Backward differential

CFD	Computational fluid dynamics
CVP	Counter-rotating vortex pair
FD	Forward differential
FoV	Field of view
IW	Interrogation window
PIV	Particle-image velocimetry
PN	Planar nephelometry
RH	Relative humidity

Chapter 1
Introduction

1.1 Solid particle preferential concentration in vortical structure

Regardless of the scale of the phenomenon, the dispersion of solid particles in a fluid flow is a significant issue in nature and industrial applications (Guha 2008). As the dispersion of toxic pollutants and hazardous biological particles (such as infectious viral aerosols dispersion through sneezing or breathing) in the atmosphere becomes a major concern, monitoring and predicting particle trajectories and concentrations are receiving more attention. In solid-gas two-phase flows, solid particles interact with a carrier-phase flow (airflow), which results in their preferential concentration or dispersion. Therefore, it is essential to predict particle behaviors based on their interactions with vortical structures in the flow in order to devise countermeasures (Marchioli & Soldati 2002; Gibert, Xu & Bodenschatz 2012). In general, particles preferentially aggregate in regions with a lower vorticity and higher strain rate, corresponding to the edges of vortices and converging flows. This is referred to as the preferential concentration (Maxey 1987; Squires & Eaton 1991; Anderson & Longmire 1995). A comprehensive investigation of how particles disperse on a relatively larger scale as a result of vortical interactions has not been conducted (Abdelsamie & Lee 2012; Tagawa *et al*. 2012; Liu *et al*. 2020), in contrast to studies on the local (sub-millimeter scale) clustering of particles affected by turbulence structures.

It is generally accepted that the preferential concentration of particles is greatest when the particle Stokes number (*St*), i.e. the ratio of particle relaxation time scale (τ_p) to background flow characteristic time scale (τ_f), is close to 1.0. This phenomenon has been studied for a small-scale flow structure, where τ_f corresponds to the Kolmogorov scale or Taylor microscale, where high-vorticity gradients and dissipative motions are predominant (Squires & Eaton 1991; Abdelsamie & Lee 2012). Using Voronoï tessellation, Liu *et al*. (2020) analyzed the necessary conditions for the particle cluster ($St \gtrsim 1.0$) to sustain, and demonstrated that particles with greater inertia and gravitational settling enable the cluster to survive longer (up to 40 times the Kolmogorov time scale). Bassenne, Moin, and Urzay (2018) demonstrated the scale-dependent properties of the preferential concentration through a scale-wise analysis utilizing wavelet decomposition. When the *St* (according to the Kolmogorov scale) is approximately 1.0, particles accumulate along specific streaks as narrow clusters, and the total energy of the concentration fields peaks in the high-wavenumber (small-scale) portion of the spectrum. For $St \simeq 10.0$, the apex of the total energy is skewed toward the low-wavenumber (large-scale) portion of the spectrum, with the highest value occurring in regions with less preferentially concentrated broad clouds.

The particle dispersion pattern resulting from vortical interactions on a reasonably large scale needs more research, and comprehension of its causes is crucial, despite the fact that earlier contributions have provided insights into particle behaviors. Few investigations have been conducted on simpler flow geometries. Longmire and Eaton (1992) found that convection of coherent vortex structures influences particle dispersion more than diffusion in a low-velocity particle-laden air jet. Observing the self-organizing dispersion process in a plane wake, Tang *et al*. (1992) demonstrated that particles concentrate at the boundaries of large vortices when *St* = 1.0 and that the particle trajectories are highly dependent on *St*. Only

vortex stretching exists and affects particle migration in this wake topology. Wen et al. (1992) observed, for a mixing layer, that even at St = 1.0, the vortex folding process forces particles to migrate into the vortex cores. Wang, Zheng & Tao (2017a) studied the transport of PM10 particles (with sizes less than 10 μm) in a turbulent boundary layer. In the upper logarithmic layer, high-velocity motions (with a higher shear stress) transported particles in the vertical direction, whereas low-velocity motions with a lower shear stress transported particles in the streamwise direction.

1.2 Flow characteristics in a jet with crossflow

Reviewing previous studies, it appears that small-scale eddies or vortices have been mainly employed to study local preferential concentration. Only simple vortical structures such as jet shear layers have been observed while focusing on particle behavior by large structures. In this regard, an attractive challenge for advancing our understanding of this issue is a particle-laden upward jet with crossflow. The particle concentrations and dispersions are determined by the well-defined large-scale vortical structures that are created downstream when a vertical jet interacts with a horizontal crossflow. Additionally, according to Steinfeld (2005) and Nathan *et al*. (2006), this phenomenon is frequently observed in the combustion of solid fuels, volcanic ash dispersions, fine dust pollution generated by smokestacks, air conditioners and gas burners in indoor environments, and solar thermal reactors. In a gas turbine, a jet in crossflow is applied to the blades and in the primary combustor. The efficiency of a gas-turbine engine increases with the higher temperature of the combustions gas. Meanwhile, hot combustion gas can deform the turbine blades (Mahesh 2013). Therefore, many previous researchers drilled small air holes on the

surface of the blades and ejected cool air jets to form a cooling insulation film on the surface of the blades (Peterson & Plesniak 2002; Sakai *et al*. 2014; Ye *et al*. 2019; Ahn 2022). Since there is also hot fuel flowing inside the primary combustor, the cool dilution (air) jet is sprayed from the combustor wall to reduce the temperature inside the combustor and make the temperature distribution uniform. At the same time, the nitrogen-oxide level also decreases. In addition, the air discharged through this exhaust contains many metallic fine particles and moisture (Wen *et al*. 2020; Izadi *et al*. 2022). Air discharged perpendicular to the ground transports moisture and pollutants away when the wind blows, which is the role of crossflow.

The interaction of a jet with crossflow, one of the canonical flows, has been extensively studied in a variety of configurations (Plesniak & Yi 2002; Sau *et al*. 2004; Plesniak & Cusano 2005; Mahesh 2013). In terms of physical behaviors such as flow kinematics, vortical structures, and entrainment, for instance, a single-phase upward jet with crossflow has been extensively studied. The velocity ratio (R) of the jet velocity (U_j) to that of the crossflow (U_{cr}) determines the overall flow characteristics when the fluid densities of the jet and crossflow are equal (Fric & Roshko 1994; Kelso, Lim & Perry 1996; Su & Mungal 2004; Sau & Mahesh 2008; Chauvat *et al*. 2020). Mahesh (2013) claims that the critical velocity ratio (R_{crit}) of 1.0 to 2.0 causes a change in the vortical structures resulting from the jet-crossflow interaction. In general, an adverse pressure gradient develops on the windward side of the vertical jet and lessens as R increases because of the crossflow-induced higher-pressure zone above the jet exit (Andreopoulos 1982; Kelso *et al*. 1996). As a result, when R is greater (> 2.0), the jet flow slows down at the jet exit, whereas when R is lower (< 2.0), the jet flow separates earlier. The crossflow boundary layer is forced to separate upstream of the jet by the adverse pressure gradient, and it transforms into shear-layer vortices that resemble Kelvin-Helmholtz rollers. At a higher R (between 2.0 and 6.0), it also contributes to the development of horseshoe, wake,

and counter-rotating vortex pairs (CVPs) (Fric & Roshko 1994; Sau *et al*. 2004; Muppidi & Mahesh 2005). Figure 1.1 shows a simplified schematic of the vortical structures. According to Kelso *et al*. (1996), the shear-layer instability causes the jet vortex sheets to tilt and fold, which results in the creation of the CVP. The horseshoe vortices (spanwise vortices traveling around the jet) interact with the wake vortices (with opposite signs) and lift away from the wall to the leeside of the jet, resulting in the CVP persisting downstream (Fric & Roshko 1994). The flow fields are dominated by hairpin vortices for a lower R (< 2.0) because the crossflow boundary-layer vorticity is significantly stronger than the leading-edge vorticity inside the jet (their signs are opposite) (Acarlar & Smith 1987; Sau & Mahesh 2008). The dynamics of solid particles as produced by the vortical interactions in a solid-gas two-phase flow have not been thoroughly studied, despite the fact that the dependency of a vortical structure on R is well understood for a single-phase flow.

1.3 Particle concentration influenced by mist droplets

After observing the changes in particle dispersion patterns over a wide range of particle inertia (Stokes number), we attempted to observe the particle concentration change based on environmental conditions. Mist droplets were selected as the material to change the particle concentration. Previous studies have recommended spraying small-sized droplets into the background flow (airflow) as an efficient dust collection method. Micro-sized mist droplet clouds formed by air atomizing nozzles are commonly used in dust-intensive applications such as industrial mineral mining (Swanson & Langefeld 2015). Importantly, the diameter of the mist droplets should be comparable to the diameter of the solid particles to be controlled, increasing the

probability that the particles will contact the droplets (Cecala *et al*. 2012; Swanson & Langefeld 2015). As the number of contacts increases, a large amount of water is coated on the particle surface and the weight of the particle increases, causing it to quickly sink out of the air. Thus, to prevent particle suspension, it is necessary to generate droplets that are similar in size to solid particles. In addition to mineral mining, heavy-metal fine dust and yellow sand are also expected to alter particle concentrations or behavior by contact with airborne mist droplets due to the hydrophilic surface of the particles. Indeed, a large drop in fine dust concentration has been observed in summer during high humidity (Yu *et al*. 2010). Conversely, in medical applications, hydrophobic particles are more necessary. Patients with respiratory diseases use dry powder inhalers (DPIs) to deliver drug powders through the airways to the lungs, but the humidity in the airways is very high, close to 100%, and the dry powders are all deposited in the airways and the patients do not get the medicinal benefits. Therefore, many researchers have proposed a methodology to make the surface of the powders hydrophobic by mixing the powders with hydrophobic additives to improve the delivery of the powders to the lungs (Hickey & Martonen 1993; Levy *et al*. 2019).

Meanwhile, the interaction between micro-sized solid particles and droplets within a complex flow structure has not been observed so far. For more efficient dust collection, how the particle dispersion characteristics change when droplets and solid particles coexist in a complex vortical structure should be observed and analyzed based on physics theory.

1.4 Main purposes

The present study presents a comprehensive overview of the dispersion characteristics of micro-sized solid particles in a flow with complex vortical structures known as a 'jet with crossflow' and the solid particle behavior changed by water mist droplets (particle dispersion pattern alteration). Therefore, this dissertation is divided into two parts; Chapter 3 describes the experimental observations of the particle dispersion mechanism in a particle-laden jet with crossflow for various Stokes numbers and velocity ratios, and Chapter 4 compares hydrophilic and hydrophobic particles with respect to their dispersion characteristics in contact with micro-sized droplets. The present study is different from many previous studies based on the Kolmogorov scale since the bulk scale observation was performed based on a large vortical structure (CVP). In addition, this study provides the first observation of bulk scale particle behavior change by mist droplet contact in Chapter 4. Therefore, our results contribute significantly to the prediction of particle behavior when controlling particle concentration or considering environmental conditions.

In Chapter 3, it is discussed that an experimental investigation of the particle distribution in a vertically ejected particle-laden jet with and without crossflow, focusing on the combined effects of St and R on the dispersion characteristics. The Reynolds number of the vertical jet with crossflow is 1170 – 5200 based on jet exit size, and we use silicon particles (sizes of 6, 53.6 and 205.5 μm, respectively) as the solid phase. The range of considered St is 0.01 – 27.42, and R is classified as 1.0 – 1.2 (strong crossflow), 3.0 – 3.5 (weak crossflow) and ∞ (no crossflow). Since we are interested in the interaction of particles with the larger-scale vortices (of spatially varying coherency) in the jet, the flow timescale to calculate St corresponds to the bulk flow scale rather than the turbulence scale used in previous studies. Details of the definition of St are explained in Chapter 2.3.1.

In Chapter 4, we explain how the hydrophilic and hydrophilic solid particle

behavior changes by the contact with micro-sized droplets for R = 1.1 and 2.85. The Reynolds number of the flow is 1975 – 5550 based on the jet exit size. In the experiments, Silicon was chosen as a hydrophilic substance, while PTFE was chosen as a hydrophobic material. The particle size of both particles under 10 μm (nominal diameter 6 μm and 10 μm for Si and PTFE, respectively) for setting $St \ll 1$. The droplets are introduced into the crossflow to increase the humidity of the flow. Therefore, the target crossflow droplet volume fraction (Φ_b) in this study is 0, 0.014 and 0.03%. As the droplets evaporate and produce water vapor, the humidity of the crossflow also increases simultaneously with the target Φ_b, so the target crossflow relative humidity is 30, 50 and 70%.

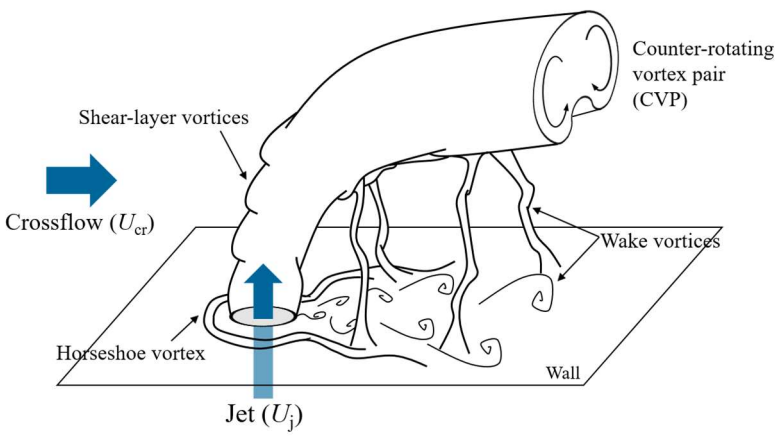

Figure 1.1. Schematic of the vortical structure in an upward jet in crossflow (Smith & Mungal 1998; Su & Mungal 2004; Plesniak & Cusano 2005; Mahesh 2013).

Chapter 2
Experimental setup and procedure

2.1 Flow facility for an upward jet with a partial crossflow

The all experimental procedures were carried out within the confines of a wind tunnel, which had dimensions of 2075 mm × 600 mm × 800 mm in the horizontal (x), transverse (y) and vertical (z) directions, as illustrated in figure 2.1. The test section was comprised of transparent acrylic plates with a thickness of 10 mm. A high-efficiency particulate air (HEPA) filter was installed at the test section exit to eliminate particles (or seeders for particle image velocimetry) and prevent flow distortions caused by backflow. The upward jet with varying bulk velocity (U_j = 1.0 – 4.0 m/s) was released through a lengthy stainless square pipe with a length (L) of 400 mm and a side length (D) of 22.5 mm, from the pipe exit located at the tunnel floor (the aspect ratio of which is large enough to have a fully developed flow at the jet exit). The Reynolds number of the vertical jet with crossflow was determined to be within the rage of 1170 – 5550, as calculated by $Re_D = \bar{u}_m D/\nu$, where $\bar{u}_m$ is the time-averaged maximum air velocity measured directly above the exit and ν is the kinematic viscosity of air under conditions of room temperature and relative humidity 30%. In the present study, it is noted that the time-averaged value is represented by an upper bar. In order to achieve uniformity in the jet and crossflow, a stainless mesh screen (wire diameter and opening size of 0.5 mm and 2.67 mm, respectively) was mounted at the exits. The test section was designed such that the distance between the pipe and the side walls was 300 mm. Considering a similar Reynolds number, it was estimated that the sidewalls interference did not impact the

spreading rate of the jet (Kwon & Seo 2005; Fellouah, Ball & Pollard 2009). A brushless DC blower fan (maximum air volume = 7.7 m^3/min) located close to the wind tunnel floor was used to blow the horizontal crossflow perpendicular to the vertical jet through a rectangular duct. Figure 2.2 displays the velocity profiles obtained at the exit of the vertical jet (at $z/D = 0$) and the horizontal crossflow (at $x/D = -13.3$). The crossflow exhibits a nearly symmetrical pattern and displays a velocity maximum at $z/D \simeq 2.0$, as shown. The characteristic of a parabolic profile is commonly seen in the jet exit fluid velocity (Mi, Nobes & Nathan 2001; Zhang *et al*. 2013; Lau & Nathan 2014, 2016). The velocity of particles at the jet exit has a profile that adheres to the fluid velocity when the Stokes number (*St*) is significantly less than 1.0. However, as the *St* increases, the effect of gravity on the particle velocity also grows (particles tend to fall down near the edge of the exit). It is important to note that the crossflow did not provide complete coverage of the cross-sectional area of the test section. Instead, the fan outlet size was limited to a range of $-3.7 \leq y/D \leq 3.7$ and $0 \leq z/D \leq 2.93$, indicating that the crossflow only partially covered the *y*-*z* plane of the test section. The corresponding crossflow turbulence level is from 15% to 30%. The crossflow streamwise turbulence intensity in previous studies spans a wide range from 0.5% to 12% for crossflow Reynolds number ~ $\boldsymbol{O}(10^2 \sim 10^5)$ (Fric & Roshko 1994; Muppidi & Mahesh 2007; Zong & Kotsonis 2019). On the other hand, if the crossflow only increases the turbulence intensity with fixed Re, the dissipation of vortical structures would be accelerated. This has been observed in other flow structures of previous studies (Zhang *et al*. 2021).

The present study focuses on a specific situation wherein the wind flow is generated in a region of limited extent close to the particle source. This approach is motivated by the observation that natural and industrial environments typically exhibit non-uniform wind patterns. By adopting this approach, we aim to investigate

the dispersion of particles in relation to their interaction with the spatially varying vortical structures. The crossflow's bulk velocity (U_{cr}) varied up to 3.0 m/s. Consequently, the velocity ratio, represented as $R = U_j/U_{cr}$, spanned across three ranges: 1.0 – 1.2, 3.0 – 3.5 and ∞.

2.2 Airflow moisture control in the wind tunnel

To investigate the effect of humidity in the airflow on solid particle behavior (see Chapter 4), we introduced mist droplets into the crossflow. As shown in figure 2.3(a), the humidity of the crossflow was increased by raising the mist droplet fraction in the crossflow by spraying dry fog mist droplets with a mean diameter of 10um near the blower. This crossflow enters the wind tunnel and injects mist droplets into the wind tunnel while also increasing the relative humidity; i.e., there are a few micro-sized droplets in the wind tunnel that are in the process of evaporating and water vapor that has already evaporated. Dry fog mist atomization was performed using an air-atomizing nozzle (SU4.5N, Spraying Systems Co.), which requires air (figure 2.3b). In other words, since the nozzle is designed with an air load and a water load, the water load sucks water from a water tank located more than 1 m below the nozzle position with a volume flux of 4.5 L/h when air of 0.3 MPa is injected into the nozzle using an air compressor. The sucked water is atomized by the compressed air and converted into a fog mist spray. This fog mist spray is directed toward the floor near the side of the blower, and some of the droplets are sucked into the blower and eventually into the wind tunnel.

In this study, two humidity sensors (RH - USB sensors, OMEGA Engineering Inc.) were used to measure the relative humidity inside the tunnel. Among the

measured data, the experimental conditions were defined based on the humidity value measured by relative humidity (RH) sensor 1 placed in the center of the rectangular crossflow outlet (see figure 2.3a). The initial relative humidity inside the lab, where the fog mist droplets have not yet occurred, is 30%. However, once droplet atomization begins, the amount of droplets accumulating in the wind tunnel increases over time, so the relative humidity value measured by sensor 1 also increases (figure 2.3c). In other words, the fan continuously injects a fixed droplet volume flow rate, whereas the crossflow outlet accumulates droplets over time, increasing the droplet volume fraction. In Chapter 4 of this paper, solid particle dynamics are analyzed at relative humidity values of 30%, 50%, and 70% measured by the sensor 1. That is, in the RH 50% and 70% cases, raw images were taken 20 and 130 seconds after the start of droplet atomization, respectively.

2.3 Solid particle characteristics

2.3.1 For particle inertia comparison

In Chapter 3, we analyzed the characteristics of particle dispersion as a function of particle inertia. The inertia of a particle is generally proportional to the particle size. Taking into account the characteristics (density, chemical compositions, etc.) of fine dust pollutants frequently seen in nature (Li *et al*. 2010; Hu *et al*. 2012), we consider 99.9% silicon particles with a density ρ_p = 2.33g/cm^3 to be dispersed phase. These particles were fed in the vertical jet using an in-house fluidized-bed type seeding device (figure 2.1). As shown in figure 2.4, the mean particle diameter ($\bar{d}_p$) was varied as 6, 53.5, 205.5 μm, respectively. The particle's equivalent

spherical diameter distribution was determined through employment of a particle size analyser (Mastersizer 1000, Marvern Panalytical Ltd.) on a 10 gram sample for each size group. The device uses a laser diffraction methodology that is grounded on the fundamental principles of static light and Mie scattering theory. Specifically, the light is scattered at larger angles by smaller particles, while larger particles scatter the light at smaller angles. Each particle size distribution depicted in figure 2.4 exhibits no variation in the range of Stokes number across orders. Thus, it can be anticipated that particles of the same size group ought to show consistent dynamics when subjected to flow-induced interactions. Furthermore, previous studies have used particles with a standard deviation (9 – 17%) in particle size similar to ours (Anderson & Longmire 1995; Hwang & Eaton 2006; Dou *et al*. 2018). In a multiphase flow, the modulation of the airflow turbulence caused by the interaction with the dispersed phase is also a significant issue (Hwang & Eaton 2006; Abdelsamie & Lee 2012; Kim, Lee & Park 2016; Lee & Park 2020), while this was not the focus of our work. We concentrated on the particle dynamics resulting from the influence of the surrounding airflow (i.e. one-way coupling). The study determined the particle volume fraction (ϕ) by calculating the total solid particle volume relative to the test section volume. The amount of particles used per measurement trial was approximately 0.3 (±0.03) grams, resulting in a ϕ value of approximately 2×10^{-7}. Based on this value, it can be assumed that the impact of the particles on the airflow and particle-to-particle collisions was negligible (Elghobashi 2006).

We took into account $St = \tau_p/\tau_f$., the particle Stokes number, to describe the dynamics of the particles. The time scale of the fluid flow was defined as $\tau_f = D/\bar{u}_m$, and the particle relaxation time scale (τ_p) was the ratio of particle settling velocity (V_s) to gravitational acceleration (g). A comparable characterization of the

flow time scale, which relies on the bulk flow scale, was also utilized to look into the dispersion of particles on a larger scale. (Fessler & Eaton 1997; Lau & Nathan 2014, 2016). As the drag force (F_{Drag}) becomes balanced with the gravitational force (F_G), the relative velocity ($v - u$) of the particle reaches to a settling velocity. Here, u and v represent the velocity of the airflow and particle, respectively. The equation for single particle motion in a balanced state is given by the following: $m_p(dv/dt) = F_G - F_D = 1/6\left(\rho_p - \rho_g\right)\pi\bar{d}_p^3 g - F_{Drag} = 0$, where m_p is the mass of a particle, ρ_p and ρ_g are the density of the particle and gas (air), respectively. The drag force exerted on a particle is contingent upon the particle Reynolds number (Re_p), which is determined by the relative velocity and be expressed as $Re_p = \rho_p \bar{d}_p |v - u|/\mu$ (μ: dynamic viscosity of air) (see table 2.1). When $Re_p < 1$, which occurs in the majority of the present cases, the viscous effect is significantly higher than the inertia, and the Stokes' drag is fixed as $F_{Drag} = 3\pi\mu(v - u)\bar{d}_p$. As the Re_p exceeds 1.0, the drag force undergoes a transition to become directly proportional to the square of the relative velocity. This can be expressed as $F_{Drag} = C_D(\pi/8)\rho_g \bar{d}_p^2 (v - u)^2$. For the drag coefficient, we selected $C_D = \left(24/Re_p\right) \cdot \left(1 + 0.15 Re_p^{0.687}\right)$ which has been verified for $1 < Re_p < 800$ (Schiller & Neumann 1933). In the present condition of ϕ, the interactions between particles were deemed insignificant, and thus the aforementioned equation for a single particle was applied without any alterations (Fessler & Eaton 1997; Lau & Nathan 2016). Therefore, the Stokes number was calculated as

$$St = \frac{\tau_p}{\tau_f} = \begin{cases} \sqrt{\dfrac{4\rho_p \bar{d}_p}{3\rho_g C_D g}} \dfrac{\bar{u}_m}{D} & \text{for } 1 < Re_p < 800, \\ \dfrac{\rho_p \bar{d}_p^2}{18\mu} \dfrac{\bar{u}_m}{D} & \text{for } Re_p \leq 1. \end{cases} \tag{2.1}$$

As demonstrated, the gravitational effect is incorporated in cases with high particle

Reynolds number. The experiments were conducted within the *St* range of 0.01 to 27.42 by altering the jet velocity and particle size simultaneously. The detailed flow variables considered in the present study are listed in table 2.1.

2.3.2 For particle surface condition comparison

In Chapter 4, we observed differences in solid particle dispersion characteristics under various relative humidity conditions in airflow for hydrophilic and hydrophobic particle groups with different particle surface conditions. As described in the previous chapter, the humidity value of a flow is proportional to the amount of mist droplets in the airflow. For this investigation, we chose 99.9% Si as the hydrophilic material and 99.9% PTFE as the hydrophobic material of the solid particles; the details of both particles are shown in figure 2.5 and table 2.2. The contact angle of Si (such as a bare wafer) to water is about 33 degrees (Kibria *et al*. 2010; Portuguez *et al*. 2017), and the contact angle of PTFE is 106 degrees (Portuguez *et al*. 2017; Martinez-Urrutia *et al*. 2018). The Si and PTFE particles have similar densities, ρ_p = 2.33g/cm^3 and 2.2g/cm^3, respectively. The mean particle diameter of the two particles was also measured with the particle size analyser (Mastersizer 1000, Marvern Panalytical Ltd.) and found to be 6 μm and 10 μm, indicating similar particle inertia. This means that the particle Reynolds number and Stokes number of both particles are much smaller than 1. Although the standard deviation of the PTFE particle size distribution is 30%, which is larger than that of Si particles, it is difficult to view it as a poly-disperse particle group in terms of particle behavior characteristics because there are more particles with smaller than average particle size (since Re_p and *St* of most particles are still very small than 1).

Similar to the observations in Chapter 3, we also set the ϕ of both particles to about 2×10^{-7} to satisfy the one-way coupling condition in the study of particle behavior under various humidity conditions. To summarize, in Chapter 4 we set the particle physical properties involved in particle inertia to be unchanged between the two groups of particles and focused only on the particle surface conditions.

2.4 Measurement techniques

2.4.1 Particle-image velocimetry (PIV)

In the present setup, distinction between silicon particles and tracers for particle image velocimetry (PIV) was unattainable in the optically captured images for the purpose of measuring the velocity of each phase. Thus, the velocity fields of solid particles and background airflow were separately measured. This methodology was considered appropriate given that the solid-gas flow under a one-way coupling regime (Fessler & Eaton 1997; Fu, Wang & Gu 2013) and that the vortex structures identified in a single-phase flow were also responsible for influencing the movement of particles in the two-phase flow. To figure out the PIV of the airflow, a high-purity liquid polyol (fog fluid standard, Dantec Dynamics) was utilized. This substance was atomized into oil droplets with a nominal diameter of 1um by smoke generators (Safex, Dantec Dynamics). These droplets were then introduced into both the vertical jet and crossflow openings as tracers (figure 2.1). The measurement plane was illuminated using a 10 W continuous wave (CW) laser (RayPower 5000, Dantec Dynamics) with a wavelength of 532 nm, which served as the light source. We applied the same setup to measure the velocity of the solid particles, substituting

silicon particles for the seeders for PIV. The utilization of a particle tracking method (PTV) would be a more suitable approach for the measurement of individual particle velocity. Nevertheless, its application can be challenging in cases where the particle size is significantly smaller than the pixel size and the solid fraction is high, as observed in the present study. According to Poelma, Westerweel, and Ooms' (2007) explanation, the application of PTV is appropriate when an image contains fewer than 100 particles, a criterion that is not met in the present investigation. In situations where Particle Tracking Velocimetry (PTV) is not a viable option, Particle Image Velocimetry (PIV) has been frequently employed to measure the velocity of solid particles in the study of particle-laden flows (Anderson & Longmire, 1995; Tóth, Anthoine & Riethmuller, 2009; Lau & Nathan, 2014, 2016; Liu *et al*., 2016). Raw images were captured at a rate of 3200 frames per second using a high-speed camera (SpeedSense M310 camera, Dantec Dynamics) with a 50 mm Nikon lens. The velocities and particle distributions were measured at identical locations. For the three-dimensional analysis, we perform the measurements on multiple *x-z* (side-view; at *y/D* = 0, 0.5, 1.0 and 2.0) and *x-y* (top-view; *z/D* = 0.5, 1.5, 2.5, 5.0 and 10.0) planes. For the side-view measurement, the size of the field of view (FoV) was $-4.0 \leq x/D \leq 4.0$ and $-6.0 \leq z/D \leq 34.0$ for the cases without crossflow, and $-2.3 \leq x/D \leq 15.0$ and $-0.7 \leq z/D \leq 14.0$ for the cases with crossflow. To account for the large side view FoV without crossflow, the FoV was measured in three segments. For the *x-y* plane measurement, the FoV covers $-5.0 \leq x/D \leq 5.0$, and $-7.0 \leq y/D \leq 7.0$. The spatial resolution of the velocity measurement was $0.01D$ – $0.014D$ or $37.5\bar{d}_p^2$ – $52.5\bar{d}_p^2$, based on the smallest solid particle ($\bar{d}_p = 6\mu$m). This was regarded as sufficient for comprehending the vortex-induced particle dispersion because we neglected to focus on particle gathering in the turbulence scales. With an interrogation window (IW) of 32 × 32 pixels (50% overlap), a

cross-correlation algorithm based on a fast Fourier transform was used to estimate the velocity vectors for each pair of tracer (or particle) images. The normalized median test (Westerweel & Scarano, 2005) was employed to identify spurious vectors, which were then exchanged for the average of the surrounding vectors in a 3×3 grid.

Various factors contribute to experimental uncertainties in velocity measurement (Raffel, Willert & Kompenhans 2007). When the velocity determined using the PIV technique is expressed in terms of M (magnification factor), Δt (time interval between successive images) and Δs (particle displacement during Δt), the uncertainty in the measured velocity can be calculated as $\delta(u) = \sqrt{(\delta(M)^2 + \delta(\Delta t)^2 + \delta(\Delta s)^2}$; percentage errors ($\delta$) in obtaining each variable are combined (Lawson et al. 1999; Kim, Kim & Park 2015; Choi & Park 2018). During the calibration, we employed a two-dimensional calibration target, and $\delta(M)$ was estimated to be approximately 0.3 – 0.4%, with M = 266 – 499 μm/pixel. For the time separation, the inter-frame time was 500 ns, and the corresponding $\delta(\Delta t)$ was 0.15%. The estimated value of $\delta(\Delta s)$ was approximately 0.7% for $\Delta s = 6.6$ pixels, taking into account the effect of a pixel resolution of 0.1 pixels. Thus, the total uncertainty in the measured velocity was close to 1.0%.

2.4.2 Planar nephelometry (PN)

The measurements of particle and mist droplet concentration were conducted through the quantification of light intensity in the Mie scattering signal that originated from the solid particles and droplets. The number density of the particles or droplets is exactly proportional to this signal. This method is commonly referred

to as planar nephelometry (PN) (Birzer, Kalt & Nathan 2012; Lau & Nathan 2014). A planar laser sheet, which is identical to the one employed in PIV, was used as the light source. The relative light intensity (proportional to the particle concentration) appears as a distinct grey-scale level of each pixel in the images; these are therefore quantified as indices for relative particle concentrations in post-processing for noise removal (Birzer *et al*., 2012), as depicted in figure 2.6(a). Initially, the grey-level value in each pixel was estimated and subsequently normalized in a range of 0 (representing black) to 1.0 (white). Given that the grey-level (light intensity) reflects the relative particle concentration, we subtracted the grey-level distribution of the background image (taken under the identical conditions as the raw images, but without the particles) from that of the raw images in order to remove noise (typically, the normalized noise grey-level values below 0.1). Then, the concentration (Θ) per IW was calculated as an area fraction, where Θ = (sum of the grey-level values contained in IW) / (IW area) (figure 2.6a). Here, the size and shape of the IW were consistent with those of the PIV measurement, both measuring 32 $\times$ 32 pixels.

The spatial non-uniformity of the incident laser intensity could have an impact on the results as we optically assessed the particle concentration based on light scattering in a very large FoV (Kalt & Nathan 2007). It is widely acknowledged that the attenuation of light power caused by particle shadows is insignificant when the volume fraction of solid particles is less than approximately 10^{-5} (2×10^{-7} for the present cases) (Kalt, Birzer & Nathan 2007; Cheong, Birzer & Lau 2016). Nevertheless, we attempted to compensate for any potential distortions caused by particles and the quality of the laser sheet. Initially, the level of light attenuation was measured along the beam direction, and then, the impact of the laser sheet profile was evaluated. We injected uniformly dispersed oil particles into the FoV and measured the intensity of the reflected light (i.e. the grey-level). The uniform distribution of the smoke provided us with information about the power intensity

irregularity in the laser sheet. The correction constant (C^*) per IW was determined based on the image of the measured oil droplet field; C^* was defined as $C^*(i,j) = 1.0 + S_{md} - S_{laser}(i,j)$, where S_{laser} is the laser light intensity value of each IW and S_{md} is the median value of S_{laser}. Here S_{laser} field was obtained by the same methodology to obtain Θ, and was normalized by its own maximum value in the FoV. In this study, (i, j) denoted the coordinates of the IW. As illustrated in figure 2.6(b), the concentration value was corrected for positions with power intensity higher (lower) than S_{md}. Upon obtaining the correction factor, it is applied to the raw particle concentration (Θ) values in each IW. This results in the calculation of the corrected concentration (Θ_{cc}), which is determined by multiplying the $\Theta(i,j)$ by the correction factor $C^*(i,j)$. Figure 2.6(c) shows an example. In conjunction with previous studies (Kalt and Nathan 2007), this correction methodology effectively mitigated the issue of excessive data distortion in areas where the laser power intensity exhibited significant bias.

For the corrected (calibrated) raw images, we evaluated the solid particle concentration distribution, which was further normalized ($\hat{\Theta} = \bar{\Theta}_{cc}/\bar{\Theta}_b$) by the bulk concentration ($\bar{\Theta}_b$), defined as follows (Lau & Nathan 2014):

$$\bar{\Theta}_b = \frac{1}{D^2 V_j} \int_{-D/2}^{D/2} \int_{-D/2}^{D/2} \bar{\Theta}_{exit}(x,y) \bar{v}_{exit}(x,y)\, dxdy. \tag{2.2}$$

Here, $\bar{\Theta}_{exit}$ and $\bar{v}_{exit}$ are the time-averaged local concentration and velocity of the particle, respectively, and V_j is the bulk particle (solid-phase) velocity, measured at the jet exit ($z/D = 0$)

In addition, corrected mist droplet concentration ($\Theta_{l,cc}$) by C^* field was used to estimate the relative humidity field. In order to take an instantaneous mist droplet raw image, as shown in figure 2.7(a), we mixed a small amount of glycerin (1% volume fraction of water) in the water to enhance visibility of the water mist droplets.

Subsequently, the corrected droplet concentration field of the raw images were obtained and the relative humidity was monitored at one-second intervals through the utilization of two humidity sensors concurrently. The measured $\Theta_{l,cc}$ and relative humidity values at the two sensor locations show a linear correlation (figure 2.7b). In other words, a rise in $\Theta_{l,cc}$ denotes an elevation of the humidity value. The correlation coefficients in this study between RH value and $\Theta_{l,cc}$ value are a = 9 and b = 30; however, these values may change based on the light source or the water's glycerin content. Therefore, the relative humidity field was obtained applying this linear correlation equation. (detailed images in Chapter 4).

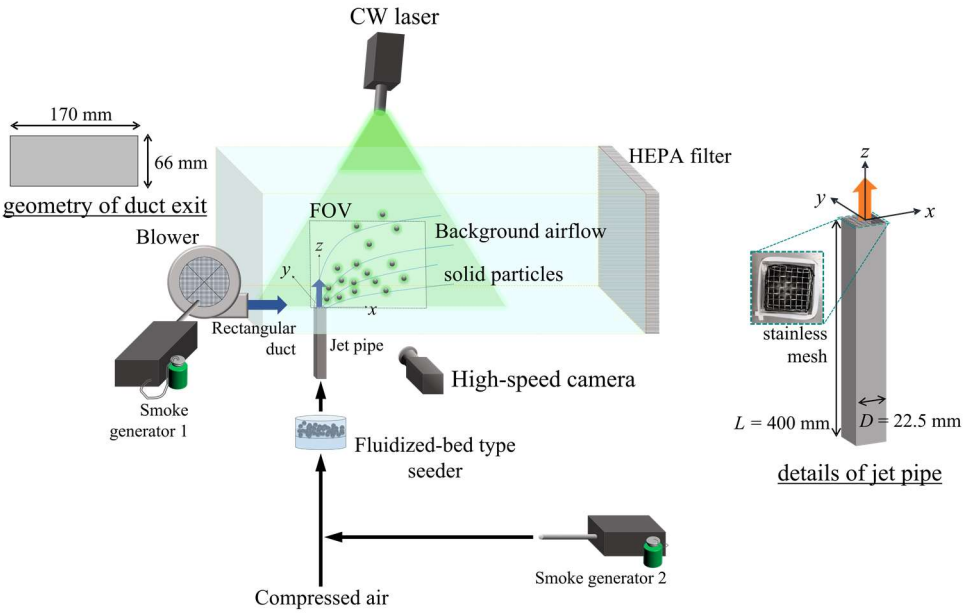

Figure 2.1. Experimental set-up for measuring the airflow structure and dispersed solid particle concentration in *x-z* and *x-y* planes with a particle image velocimetry and high-speed imaging (camera and laser are shown for *x-z* plane measurement).

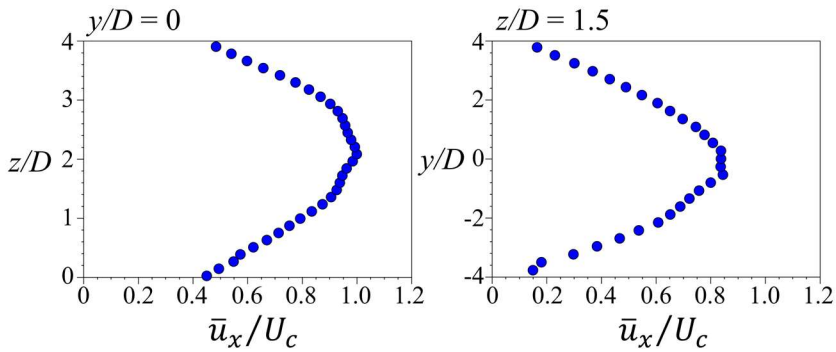

crossflow profile at the duct exit

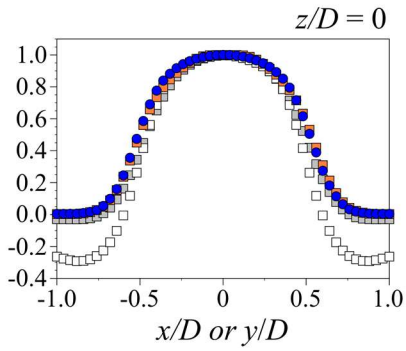

jet profile at the pipe exit

Figure 2.2. Time-averaged velocity profiles for the crossflow and vertical jet measured at the exit of the crossflow duct (*x/D* = -13.3) and jet pipe (*z/D* = 0), respectively; ●, airflow velocity; ■, particle velocity (*St* = 0.013); ■, particle velocity (*St* = 1.07); □, particle velocity (*St* = 15.71)

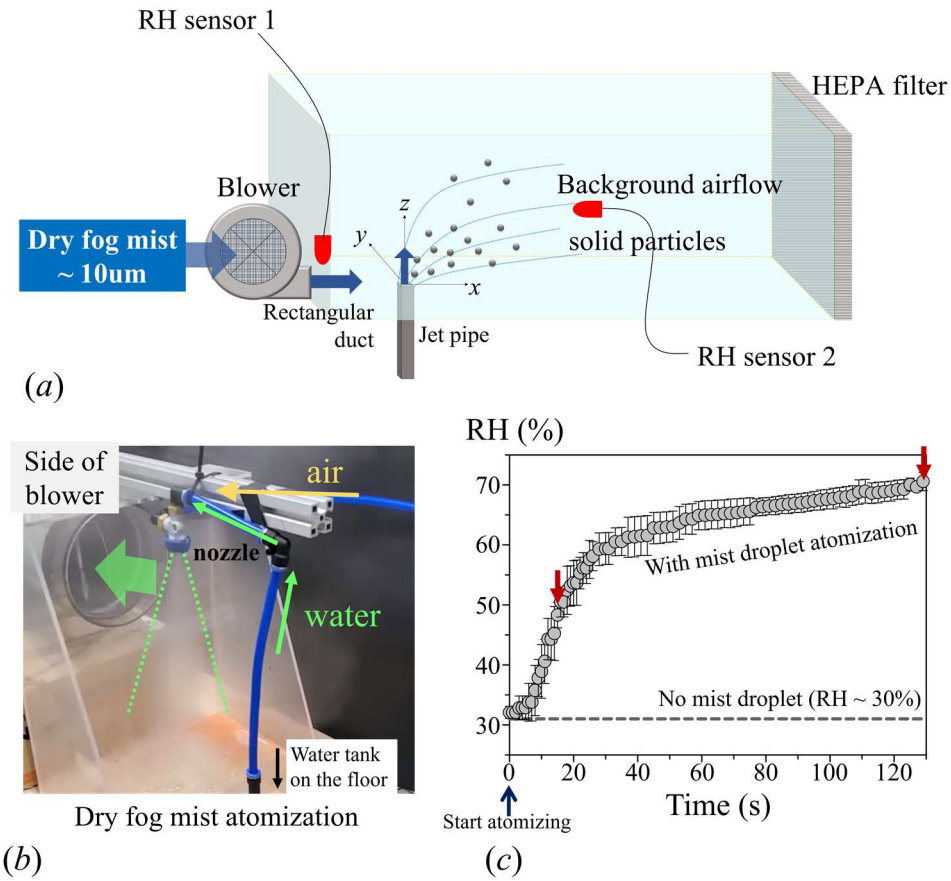

Figure 2.3. Experimental set-up for introducing the mist droplets into the crossflow and measurement of relative humidity (RH): (*a*) A schematic of set-up indicating two sensor locations (when performing PN for mist concentration measurement, the same laser and camera are used as in figure 2.1); (*b*) Air-atomizing nozzle at the side of blower; (*c*) Relative humidity evolution over time near the crossflow outlet as measured by sensor 1.

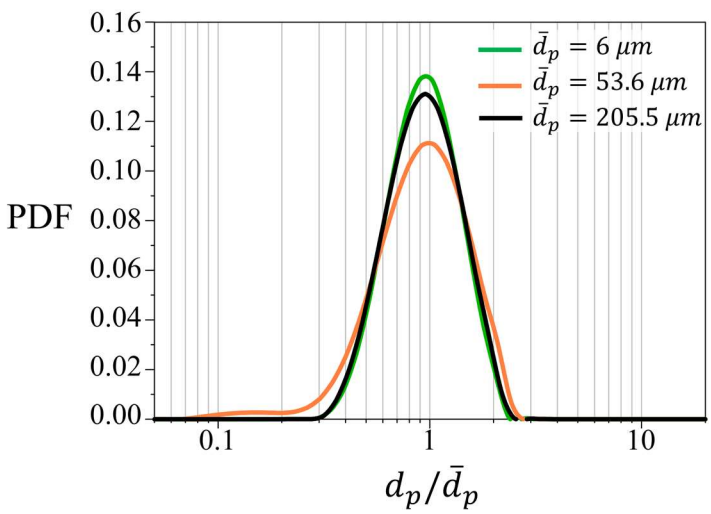

Figure 2.4. Probability density function (p.d.f.) of particle size considered in Chapter 3.

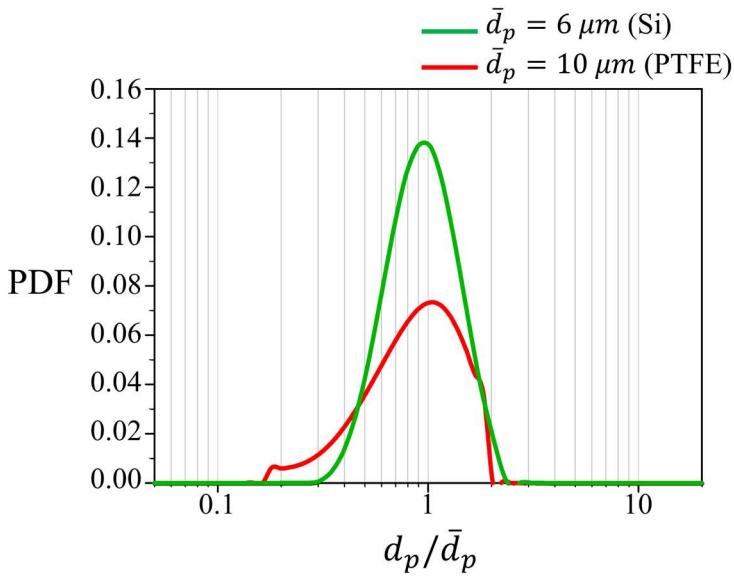

Figure 2.5. Probability density function (p.d.f.) of particle size considered in Chapter 4.

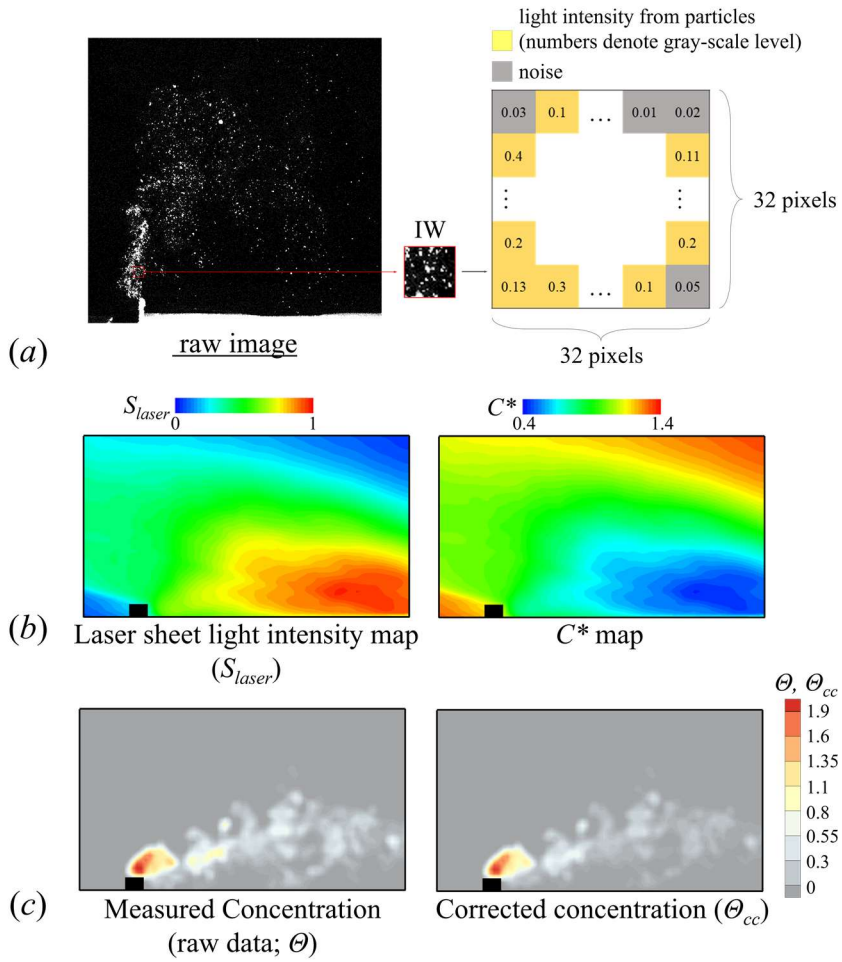

Figure 2.6. Particle concentration measurement by PN: (*a*) raw image of solid particles and a schematic diagram to calculate light intensity of an IW (yellow color: pixels identified as being occupied by solid particles; grey color: noise); (*b*) correction of non-uniform laser light sheet; (*c*) correction of measured particle concentration.

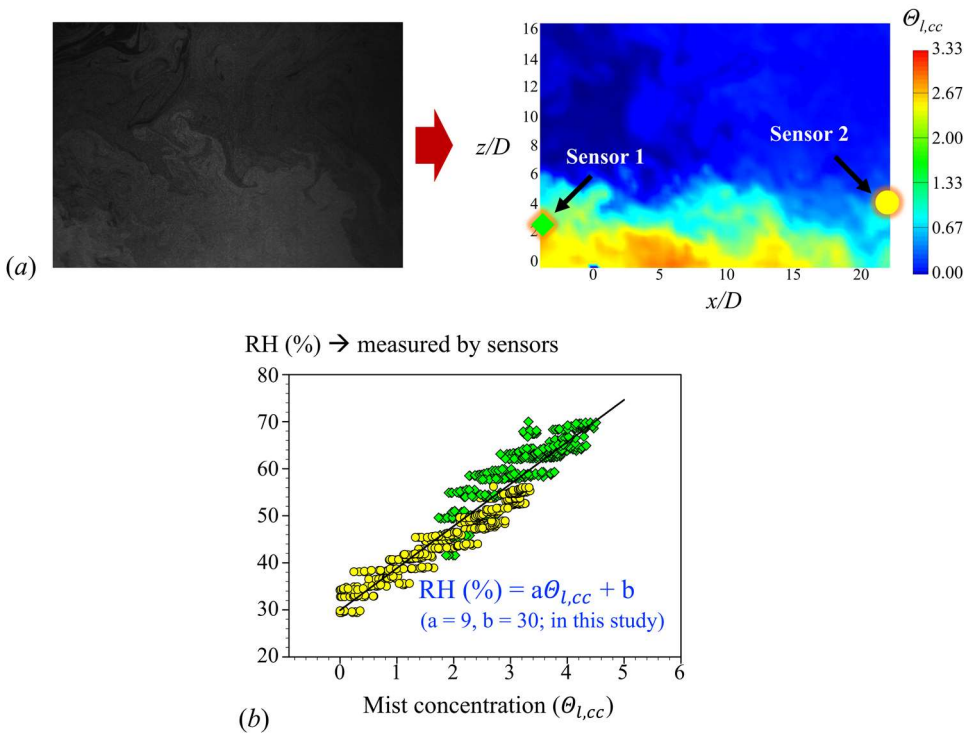

Figure 2.7. Mist droplet concentration measurement: (*a*) Conversion from mist droplet raw image to concentration field (two sensor locations shown); (*b*) a linear correlation between the measured RH value and mist concentration ($\Theta_{l,cc}$) at sensor locations; ●, sensor 1; ● (yellow), sensor 2.

R	St	$\bar{d}_p$ [μm]	Re_D	Re_p
∞ (No crossflow)	0.013	6	1740	0.060
	1.07	53.6	1740	0.173
	1.5	53.6	2450	0.120
	3.18	53.6	5200	0.849
	15.71	205.5	1740	0.578
	21.59	205.5	5200	18.30
3.3	0.012	6	1640	0.014
3.3	0.905	53.6	1640	0.693
3.0	1.485	53.6	2440	0.380
3.3	3.11	53.6	5120	0.259
3.5	14.18	205.5	1640	0.770
3.5	10.13	205.5	5120	2.660
1.0	0.01	6	1320	0.005
1.0	0.771	53.6	1320	0.201
1.1	0.965	53.6	1170	1.826
1.0	1.972	53.6	3220	0.090
1.2	11.33	205.5	1320	1.182
1.2	27.42	205.5	3220	0.732

Table 2.1. Summary of the considered experimental parameters of gas and solid phases at Chapter 3.

R	Particle	Contact angle[°]	St	$\bar{d}_p$ [μm]	Re_D	Re_p
2.85	Si	33	0.036	6	5550	0.118
	PTFE	106	0.095	10		0.161
1.1	Si	33	0.015	6	2000	0.036
	PTFE	106	0.033	10		0.056

Table2.2. Summary of the considered experimental parameters of gas and solid phases at Chapter 4.

Chapter 3
The particle dispersion mechanism by various *St*

3.1 Airflow structures

Before investigating into the specifics of particle dispersion, the key characteristics of continuous-phase flow in terms of time-averaged fields are described. In comparison to the information found in the literature, figure 3.1 displays the kinematics of the jet centerline with or without crossflow. The trajectories of the time-averaged jet centerline on the *x–z* plane show a streamline starting at the center of the jet exit (Yuan & Street 1998; Su & Mungal 2004) (figure 3.1a). As shown, they follow the typical tendency of the decay (diffusion) characteristics of a jet. With crossflow, the jet centerline trajectory tilts toward the leeward side of the exit, which becomes stronger as R decreases. Compared with previous studies, the deflection of the present jets is less, in spite of the lower R. This is because the crossflow blows from a local region near the wind tunnel floor (not covering the entire *y–z* plane, as in previous studies). It is further noted that the deflection of the jet depends on Re_D and R. The jet centerline trajectory can be fitted with a power law of $z/D = a(x/D)^b$, where a and b are empirical constants (Mahesh 2013), and it is found that the exponent b (= 0.60 – 0.66) in larger R cases is larger than that (= 0.17 – 0.40) in smaller R cases. This indicates that the jet evolves farther downstream with a higher R. Likewise, the constant a (= 1.5 – 2.1) in smaller R cases is smaller than that (a = 6.5–8.9) in larger R cases. In detail, the jet in the lower R cases is not affected by the Reynolds number (Re_D), but the jet deflection is

determined by the combined effect of R and Re_D in the cases of higher R (weak crossflow). That is, as the Reynolds number increases to Re_D = 4030 (R = 3.5), the jet is tilted more than that of Re_D = 1640 (R = 3.3), despite the slightly higher R (so that the constant a (= 6.8) is smaller than the latter (= 8.9)). In the same vein, Muppidi & Mahesh (2005) explained that it is difficult for a jet to penetrate a stronger crossflow even with the same R because of the thinner crossflow boundary layer, so the jet deflects toward the crossflow-streamwise direction.

Figure 3.1(b) shows the time-averaged vertical velocity ($\bar{u}_{z,c}$) profiles along the jet centerline, normalized by $\bar{u}_{zo,c}$ at the jet exit. Here, the position of the jet centerline is expressed as the 's coordinate' from the jet exit (s = 0); the s coordinate denotes the jet centerline length from the jet origin. For a typical straight jet (without crossflow), the velocity does not undergo a decay up to $z/D \simeq 5.0$ (Fellouah *et al.* 2009; Mi *et al.* 2013). This is because the effective mixing by the issued jet does not spread sufficiently wide to penetrate the centerline near the jet exit, and the entrainment of ambient flow is not substantial there, i.e. inducing a 'potential core' (Namer & Ötügen 1988). Unlike previous studies, the jet flow in this study begins to decelerate immediately after the jet exit, with a small peak at the z/D range of ~1.0 – 2.0; this is attributed to the encouraged entrainment of the surrounding air to the jet center (at z/D < 5.0) from the enhanced turbulence, via the mesh screen installed at the jet exit. At z/D > 10.0, the decay of $\bar{u}_{z,c}$ along the radial distance has no significant variation with Re_D, and is similar to the others. Nevertheless, it is possible to model the decay of the jet velocity along the vertical (z) direction as $\bar{u}_{z,c}(z)/\bar{u}_{zo,c} = B/(z/D - z_o/D)$, with the reference position denoted as z_o (Pope 2003); this model holds for the region of monotonically decaying behavior. For the present cases, the decay constant (B) is empirically determined as 4.97 – 6.2 (Re_D = 1740 – 5220), approximately agreeing with the values from previous studies

(5.04 and 5.9 at Re_D = 4000 and 6000, respectively (Mi *et al*. 2013); 5.59 at Re_D = 10000 (Fellouah *et al*. 2009)). This implies that the present flows follow the self-similar characteristics of a fully developed jet. With crossflow, the $\bar{u}_{z,c}$ decays faster as R decreases. For a higher R (~ 3.0), the decaying rate of $\bar{u}_{z,c}$ is similar to that of jets without crossflow up to s/D = 5.0 – 6.0, and becomes slightly faster downstream. Compared with the previous studies (R $\simeq$ 4.0 – 5.7) with a round jet in crossflow (Keffer & Baines 1963; Muppidi & Mahesh 2007), $\bar{u}_{z,c}$ decreases more slowly despite a smaller R ~ 3.0. That is, $\bar{u}_{z,c}$ decays at a rate of $(s/D)^{-1.3}$ for a transverse jet with crossflow (Smith & Mungal 1998; Muppidi & Mahesh 2007), but it decays at a rate of $(s/D)^{-0.4}$ – $(s/D)^{-0.3}$ for the present cases of R ~ 3.0. Then, the decaying rate of $\bar{u}_{z,c}$ changes at $s/D \simeq$ 10.0 in the previous studies, but it is quite constant for the present cases. This is because the mass flux of the locally blown crossflow is too small to sufficiently bend and separate the jet toward the leeside of the jet. Rather, the sudden change of the decay rate in $\bar{u}_{z,c}$ appears for the cases of R ~ 1.0. As the crossflow becomes stronger (R ~ 1.0), the centerline jet velocity experiences a sharp decrease earlier (up to s/D = 3.0 − 4.0), and then the decaying slope becomes similar to that of a vertical jet. Here, $\bar{u}_{z,c}$ decays at a rate of $(s/D)^{-1.4}$ – $(s/D)^{-0.7}$ for the upstream jet with a strong crossflow, which is similar to the cases of higher R in previous studies. Although the jet evolution at a certain value of R does not match with the previous studies, due to the partial crossflow specific to the present study, the trend in the change of jet velocity with R agrees with each other. Compared with Re_D, the velocity ratio is more influential in determining the decaying pattern of the jet; within a similar range of R, the decay rate becomes slower with increasing Re_D.

The fluctuating nature of the jet (the root-mean-square of the vertical velocity ($u'_{z,c_{rms}}$) along the centerline) is shown in figure 3.1(c). In general, the turbulence

intensity is measured to be higher than that in previous studies, especially near the jet exit, owing to the mesh screen at the jet exit. In the self-similarity region ($z/D >$ 10.0), the turbulence intensity tends to be saturated for a vertical jet (Tong & Warhaft 1994; Fellouah *et al*. 2009; Mi *et al*. 2013); this is also found for the present case of $Re_D = 5200$. When Re_D is lower, the turbulence intensity continues to increase, even after $z/D \simeq 10.0$ (Namer & Ötügen 1988; Suresh *et al*. 2008; Xu *et al*. 2013). Suresh *et al*. (2008) explained that this is because the large-sized vortices, mostly forming in a lower Re_D jet, cause more entrainment and jet decay, preventing the jet from approaching the fully developed state. With crossflow, the turbulence intensity increases with decreasing R and Re_D; it is affected more by the change in R than by that in Re_D. This is because the flow characteristics including the turbulence along the centerline are governed by the dynamics of CVP. When the velocity ratio is small (strong crossflow effect on the jet), $u'_{z,c_{rms}}$ stars to increase sharply at $s/D = 2.5$, owing to the wake vortices near the floor (Fric & Roshko 1994). A slight decrease in R increases the effect of the wake vortex, causing $u'_{z,c_{rms}}$ to increase more rapidly downstream (detailed vortical structures are discussed below). As R increases (weak crossflow effect), however, the influence of Re_D becomes stronger. Up to $s/D = 6.0$, a stronger turbulence is induced with a higher Re_D, which is reversed downstream. Meanwhile, $u'_{z,c_{rms}}$ of a previous study (R = 4.0, Keffer & Baines 1963) approaches the same value as that in the potential cores of a jet (without crossflow), and increases dramatically in the downstream, showing a much higher value than those of $R \sim 3.0$ cases. These phenomena will be theoretically discussed further in regards to the pressure distribution (mechanism of CVP formation).

Figure 3.2 and 3.3 show the time-averaged non-dimensional vorticity contours and velocity vector fields (normalized by D and $\bar{u}_m$) for different R values (without and with crossflow, respectively) on the x-z and x-y planes. Without crossflow (R =

∞), the vortical structure in the *x-z* planes simply shows a pair of time-averaged transverse vortical structure ($\overline{\omega}_y^*$) that gradually dissipate along the vertical direction (figure 3.2a). In the top-view planes the flow structure is much less coherent, and the vertical vorticity ($\overline{\omega}_z^*$) component, much smaller than $\overline{\omega}_y^*$ in the *x-z* planes, is scattered and dispersed out of the jet center (figure 3.2b). The strength of $\overline{\omega}_z^*$ does not decay much along the vertical direction, as it is driven by the diffusive spreading motion, rather than the jet inertia. In contrast, in the *x–z* planes, the vortical structures become wider along the vertical (up to z/D = 20.0) and transverse (up to y/D = 1.0) directions, and are mostly driven by the jet inertia.

When the jet encounters the crossflow, the vortical structures on the *x–z* planes are deflected to the leeward side and a coherent flow structure, i.e. the CVP is observed on the *x–y* planes. Its dynamics is governed by the velocity ratio. For a higher velocity ratio (R = 3.0 at Re_D = 2440, for example), the negative $\overline{\omega}_y^*$ on the windward side is slightly larger than the positive one on the leeward side, owing to the development of jet shear-layer vortices (figure 3.3a). The shear-layer vortices contribute to the folding of the jet vortex sheets and the tilting of its trajectory, such that a structured CVP is induced (figure 3.3b). Owing to these 'tilting and folding' behaviors, the contours of the transverse vorticity and the vectors of the jet velocity are bent more to the leeward side near the jet exit on the jet shear plane (y/D = 0.5 and 1.0) than on the jet-center plane (y/D = 0) (figure 3.3a) (Kelso *et al*. 1996; Cortelezzi & Karagozian 2001). Although the magnitude of the $\overline{\omega}_z^*$ contained in the CVP increases, it is still lower than $\overline{\omega}_y^*$. In the x-z planes the transverse vortices with opposite signs move away from each other at z/D of approximately 5.0; at this location, the CVP disturbed, and disappears. Rigorously speaking, it is more adequate to say that the coherency of the CVP disappears, based on the vorticity measurements; however, for the concise expression, we will use 'collapse of CVP'

in the below. This is related to the local crossflow that covers the partial area; the formation of shear-layer vortices outside of the crossflow area is not observed and $\overline{\omega}_z^*$ contained in the CVP drastically decreases. As R becomes as low as 1.1, however, the positive $\overline{\omega}_y^*$ on the leeward side is significantly enhanced in the x-z planes (figure 3.3c). This is caused by the stronger crossflow boundary-layer vortices, which play a role in bending the jet significantly toward the leeward side. Owing to the bending, a large hairpin vortex is created near the jet exit (Mahesh 2013). The head of the hairpin vortex is represented as a positive transverse vortex at the x–z planes (y/D = 0 and 0.5) (figure 3.3c) and two legs are shown as a large CVP at x-y planes of z/D = 0.5 and 1.0 (figure 3.3d). At this smaller R, the magnitudes of $\overline{\omega}_z^*$ and $\overline{\omega}_y^*$ are comparable to each other (the vorticity contained in the CVP is slightly higher than that in the hairpin head). The distance between the counter-rotating vortices on the x–y plane increases as well.

Figure 3.4 shows the instantaneous CVP structure in x–y planes, comparing the cases of R = 3.0 and 1.1. Similar to the time-averaged flow fields, it is observed that the CVP forms near the jet exit and evolves (deflected horizontally) depending on the velocity ratio. The integrity and size of the instantaneous CVP are greater for the lower R and the distance between the vortex pair is also larger than that of the higher R case. For higher R, the crossflow passes around the CVP above the jet exit and is entrained into the jet at the leeside of the jet exit. Along the vertical direction, the CVP is developed by the entrained crossflow up to $z/D \simeq 5.0$ (figure 3.4a). On the other hand, for lower R (= 1.1), the strong counter-rotating vortices are further distanced from each other along the lateral direction because the jet and crossflow are separated at the windward side of the jet near the jet exit ($z/D < 2.0$) (figure 3.4b). The separation of jet and crossflow is attributed by an adverse pressure gradient above the jet exit (see below) which is the cause of CVP formation proposed by

previous studies (Fric & Roshko 1994; Sau *et al*. 2004; Muppidi & Mahesh 2005). The time-averaged and instantaneous vortical structures in the present square jet with a partial crossflow matches with previous studies (Sau *et al*. 2004; Plesniak & Cusano 2005), which explained that the square jet also interacts with the crossflow like the behavior of the round jet and forms the same vortical structures, the CVP. This is important because our major focus is the experimental and theoretical establishment of a particle dispersion pattern resulting from the interaction between the particles and spatially developing coherent vortical structure like the CVP.

In addition to CVP, we also observed the characteristics of horseshoe vortex, which is one of the main vortical structures in 'jet with crossflow'. Figure 3.5 shows the instantaneous vorticity and velocity field of the case flow with R = 3.3 & Re_D = 1640. As shown in this figure, a horseshoe vortex is generated near the bottom of the jet pipe leading edge location. This vortex is caused by the crossflow boundary layer experiencing an adverse pressure gradient in front of the jet pipe, meaning that the crossflow separates from the jet pipe leading edge and forms spanwise vortices that pass around the jet pipe. In a conventional jet with crossflow, where the jet is ejected directly from the floor, the horseshoe vortex and the Kelvin-Helmholtz vortices located in the jet shear layer interact with each other, causing the horseshoe vortex to entrain a portion of the jet flow. However, since the horseshoe vortex in this study does not encounter the jet shear layer, it does not entrain the jet flow and is not able to influence the behavior of particles dispersing inside the jet. Therefore, this paper focuses on the effect of CVP on the behavior of particles in the jet.

The dynamics of the CVP can be understood by analyzing the pressure distribution in the flow (Muppidi & Mahesh 2005). To achieve this, we estimate the pressure distribution based on the time-averaged velocity field. By taking the divergence of the Reynolds-averaged Navier–Stokes equation in the Cartesian coordinate system, we can obtain an elliptic equation for the pressure (called the

Poisson equation), expressed as

$$\nabla^2\bar{p} = \rho_g \frac{\partial}{\partial x_i}\left(-\frac{\partial}{\partial x_i}(\bar{u}_i\bar{u}_j) + \nu\nabla^2\bar{u}_j - \frac{\partial}{\partial x_i}\overline{u'_i u'_j}\right). \quad (3.1)$$

By solving this equation based on the measured velocity field, we obtain the pressure field; equation (3.1) is spatially integrated using a Poisson solver based on a differential matrix with a fractional step (central difference scheme) and bi-conjugate gradient stabilized method (Rosenfeld, Kwak & Vinokur 1991; Vuorinen & Keskinen 2016). This is a common way of obtaining pressure fields from velocity field data and has been adopted in experimental and numerical studies (Choi & Park 2018; Ferreira & Ganapathisubramani 2020). Figure 3.6 shows the time-averaged pressure coefficient ($\bar{c}_p$) calculated as $\bar{c}_p = (\bar{p} - p_{cr})/(0.5\rho_g u_{cr}^2)$, where u_{cr} and p_{cr} are the velocity and pressure at the crossflow free stream (*x/D* = -2.2 and *z/D* = 1.5), respectively, with the trajectories of the jet and vortex. As illustrated in figure 3.6(a), the vortex trajectory is tracked as the positions of the local vorticity maxima on the n-coordinate, perpendicular to the s-coordinate along the centerline.

When the velocity ratio is small, the pressure field in the flow is found to be similar to that in previous studies (Sau *et al*. 2004; Muppidi & Mahesh 2005). That is, an adverse pressure gradient is induced above the jet exit (figure 3.6b), by which the jet is separated early, and the hairpin vortex (shows up as CVP in *x–y* planes) forms thereafter. Simultaneously, the separated crossflow is entrained into the hairpin vortex and center strengthens it. Owing to the jet separation, the entrained flow moves out of the jet-plane (*y/D* = 0), as shown in figure 3.4(b). Thus, the jet velocity and turbulence intensity along the centerline decline drastically before the hairpin vortex collapses (figure 3.1b & c). As the hairpin vortex is formed near the jet exit and collapses immediately owing to a sufficiently higher Re_D (> 600; see Sau & Mahesh 2008), the wake trajectory starts at the lower pressure region formed immediately above the exit, and staggers unstably following the centerline after *z/D*

= 2.0. Figure 3.7(a) shows the trajectories of the jet centerline and vortex for three cases with lower R. As shown, a similar phenomenon is measured regardless of the difference in Re_D. When the jet is deflected the most (R = 1.0), the vortex trajectory oscillates quite unstably, and moves toward the bottom, owing to the wall vortices (highlighted with an arrow in figure 3.3c). This contributes greatly to enhancing the turbulence level downstream (figure 3.1c). Also, as R becomes slightly smaller from 1.2 to 1.0, the magnitude of the adverse pressure gradient becomes larger, so that the jet is further bent to the floor (figure 3.1a), increasing the influence of wall vortices. As a result, the jet velocity further decreases downstream after the collapse of CVP, and conversely, the turbulence intensity increases more (figure 3.1b, c). Wall vortices induced by the larger flux of crossflow and stronger collapsed CVP enhance the turbulence level downstream much more than that of higher R cases. Thus, for lower R cases, the jet is separated earlier near the jet exit; as such, the hairpin vortex is formed subsequently regardless of Re_D, and collapses near z/D = 2.0 (figure 3.7b).

When the velocity ratio is large (weak crossflow), the pressure distribution is considerably different from the typical case of a strong crossflow (figure 3.6c). As shown, there is no higher-pressure region (adverse pressure gradient) above the jet exit; thus, the jet evolves without being separated by the crossflow. Rather, a very low-pressure region is formed on the jet exit so that the crossflow is entrained into the jet, by which the CVP is formed. As the flux of the crossflow in this condition is not large, the CVP is not stronger than in cases with lower values of R. In addition, the vortex trajectory represents the center of the CVP (Muppidi & Mahesh 2007). Accordingly, the boundary of the lower pressure zone corresponds to the location where the CVP starts to collapse. As shown in figure 3.6(c), the low-pressure region formed by the crossflow ends approximately at z/D = 5.0, after which the vortex trajectory deviates and spreads along the x-axis. Moreover, the level of crossflow entrainment is affected by Re_D. Figure 3.8(a) illustrates the jet centerlines and vortex

trajectories for cases with higher R. For all cases, the vortex trajectory initially follows the jet centerline and then starts to separate at some downstream location. As Re_D increases, more mass flux is entrained into the jet, and the point at which the CVP collapses is gradually pushed downstream, as indicated by the arrows in the figure. Figure 3.8(b) clearly shows the state of the collapsed or collapsing CVP as measured at $z/D = 5.0$ for each case. Interestingly, this location matches the position where the dependency of the turbulence intensity on Re_D is reversed (figure 3.1c). When the crossflow is not strong, the flux of entrained crossflow is dependent on the Reynolds number; the higher the Re_D, the more crossflow entrained in the jet. The greater entrained flux generates a higher vorticity and turbulence intensity in the CVP. After the CVP collapses, the effect of crossflow disappears and simple jet vortices are created in the lower Re_D cases, further decaying the jet centerline velocity and increasing the turbulence intensity. On the contrary, Muppidi & Mahesh (2007) explained that CVP is continuously developed as the crossflow entrains into the jet at the downstream, which supports the sudden increase of turbulent intensity (figure 3.1c). The entrained flow is concentrated to the jet center in the present cases (see figure 3.4), so that it hardly reduces the upstream jet centerline velocity. On the other hand, the CVP with a lower R was fully evolved entraining the separated crossflow, so that the jet velocity decay rate became faster from $(s/D)^{-0.6}$ to $(s/D)^{-1.3}$ (figure 3.1b); most of the entrained flux moved out of the jet-center plane owing to the separated jet (Mahesh 2013). The velocity decay rates of previous studies are comparable to those of lower R cases of the present study. In this context, the factors that dominate the evolution of the flow characteristics along the centerline is related to the mechanism of CVP formation. Below, we explain the dispersion behaviors of particles in interactions with the above-mentioned flow structures.

3.2 Particle dispersion patterns

3.2.1 Particle concentration decay away from the jet exit

In this section, we evaluate the characteristics of the three-dimensional particle dispersion depending on R and St. Figure 3.9 shows typical instantaneous particle distributions (raw images) for selected cases of lower R (~ 1.0) and higher R (~ 3.0) values, in which the CVP is generated in the flow (figures 3.3, 3.7 and 3.8). The most prominent feature in this figure is the distinguishable difference in the particle distribution characteristics near the jet exit (z/D = 0.5) with R. When R ~ 1.0, the solid particles of St = 0.01 and 0.965 are dispersed by the coherent vortex structure near the jet exit, but the detailed pattern is different (figure 3.9a). When $St \lesssim 1.0$, we observe a C-shaped particle cluster whose leading edge is located at the jet exit, owing to a strong CVP. As the jet develops, the particles with $St \ll 1.0$ are transported along not only the transverse (y) direction, but also the crossflow-streamwise (x) direction at z/D = 2.0, where the CVP starts to collapse. Nevertheless, a large number of particles still gather at the leading edge of the C-shaped cluster when the Stokes number is close to 1.0. When $St \gg 1.0$, the particles tend to spread independently of the vortex structure; they are clustered only above the jet exit and disperse uniformly along the streamwise and transverse directions.

On the other hand, for higher R cases (~ 3.0), most of the particles are detected on the jet exit, as the particle movement is less affected by the CVP (figure 3.9b). Rather, after the CVP collapses, a relatively vague C-shaped particle cluster is observed for $St \lesssim 1.0$ away from the exit (z/D value of ~ 5.0). Unlike the lower R cases (figure 3.9a), the particles gather at the leading edge of the C-shaped cluster, even at $St \ll 1.0$. For St $\gg$ 1.0, the particles move independently of the vortex

structures, and tend to spread in the transverse direction above the jet exit. As shown in this representative data, it is clear that the responses of the particles to the coherent vortex structure change mainly according to St as the velocity ratio decreases. As discussed in Chapter 3.1, the vertical jet (without crossflow) does not change substantially with Re_D. With crossflow, the global pictures of the vortical structures are not affected drastically by Re_D, but it needs to be considered when the crossflow is weak (higher R cases). The effect of Re_D (inertia) on the particle dispersion (if any) is reflected in St.

To quantitatively analyze the particle dispersion, we calculated the probability density function (p.d.f) for the particle concentration values in the top-view planes. In figure 3.10, as concentration data, time-averaged concentration fields in the area where CVP develops among the top-view planes are considered; for $R \sim 1$ cases, concentration fields at $z/D = 0.5$; for $R \sim 3$ cases, $z/D = 2$. The corrected local concentration values are normalized by the bulk concentration as $\hat{\Theta} = \bar{\Theta}_{cc}/\bar{\Theta}_b$ (see Chapter 2.4). Comparing the p.d.f bar graph and the raw image inset in figure 3.10, we can notice that they show the same tendency of particle dispersion. When $St \ll 1$ with $R \sim 1$ (figure 3.10a), the frequency of low concentrations is high because the particles spread evenly in the crossflow direction. As the St increases near 1, the frequency of low concentrations decreases slightly and the frequency of high concentrations increases because the particles are concentrated towards the jet center. When St becomes very large, above 10, the p.d.f bars are uniform for all concentration values because many particles are concentrated in the jet center and there are also scattered particles in the periphery. For $R \sim 3$ cases (figure 3.10b), the p.d.f profile shape in the low R cases (figure 3.10a) is reversed as a function of St. For cases with $St \lesssim 1$, the p.d.f shapes are similar to each other because the particles almost gather at the jet center, such as the case with low velocity ratio $St = 0.965$. However, for $St \gg 1$, the probability of low concentration values is overwhelmingly

high because the particles are not affected by CVP and are scattered upwards, spreading evenly in the top-view plane.

A p.d.f of particle concentration values can describe the particle dispersion pattern observed in the raw image, but lacks detailed location coordinate data. This approach to concentration pdf analysis is useful in cases where particle dispersion characteristics are similar regardless of location within the field of view, such as in homogeneous and isotropic chambers (Wood *et al*. 2005; Monchaux *et al*. 2010). However, the flows observed in this study exhibit different vortical structure characteristics depending on their location in three-dimensional dimensions, and thus location information for specific concentrations is essential. Therefore, the radial (*r/D*) distribution of the particle concentration is evaluated for the time-averaged solid-phase fields on each of the four *x-z* planes (*y/D* = 0, 0.5, 1.0 and 2.0). Figure 3.11 shows the concentration distributions for selected cases, and the data in each *x-z* plane are distinguished with different colors. In figure 3.11, the border of the data indicates the maximum concentration ($\hat{\Theta}_m$), as measured at the radial distance from the jet exit (particle source). For all cases, it is found that the maximum value begins to decrease steeply from the particle source (*r/D* = 0); subsequently, the decay rate becomes quite slow away from the origin. We define the location at which the decaying rate changes as a division point (P_d). To determine P_d consistently, forward (FD) and backward (BD) differentials of the maximum concentration are calculated as $FD_i = (\hat{\Theta}_{m,N} - \hat{\Theta}_{m,i})/((r/D)_N - (r/D)_i)$ and $BD_i = (\hat{\Theta}_{m,i} - \hat{\Theta}_{m,1})/((r/D)_i - (r/D)_1)$, where $i = 1, \ldots, N$ (N: last position with the data of $\hat{\Theta}$). The position of the maximum BD is designated as P_d. The values of BD and FD at the position of P_d are referred to as G_1 and G_2, respectively, indicating a representative decaying rate in each realm. As noted in figure 3.11, the position of P_d moves toward the source as R decreases. Accordingly, without crossflow, P_d appears

at $r/D > 20.0$, with a slower decaying slope (figure 3.11a); however, with crossflow, the particle concentration decreases at a faster rate, and the position of P_d occurs at $r/D < 10.0$ (figure 3.11b, c). On the other hand, the trend of the concentration peak (distribution) changes across the plane of $y/D = 1.0$, and we think this is because the $y/D = 1.0$ plane corresponds to the edge of coherent vortical structure; jet shear-layer vortex and CVP for the cases without and with crossflow, respectively (figure 3.2 and 3.3).

Figure 3.12 shows the variation in the location, P_d, and corresponding concentration decay rates (G_1 and G_2) when varying St and R. As explained above, with a stronger crossflow, P_d tends to move toward the particle source (figure 3.12a), and the decaying slope (G_1) in the fast-decaying region becomes steeper (figure 3.12b). Downstream after P_d, the slope G_2 is approximately equal to 0.1, irrespective of R and St. It is noted that G_1 and G_2 show similar values in the cases without crossflow, whereas the difference between G_1 and G_2 becomes larger with decreasing R for cases with crossflow. It is thus understood that the region ($r/D < P_d$) where most of the particles gather preferentially is confined closer to the jet exit with decreasing R, in a close relation to the dynamics of the CVP. This is also supported by our observation that the coherent vortical structures disappear at $r/D > P_d$.

Without crossflow, P_d generally appears farther from the jet exit than in cases with crossflow (figure 3.12a), owing to the weaker and less structured streamwise (vertical) vortices in the jet (figure 3.2). In addition, particles with a smaller St are dispersed further (P_d increases), as the particles are more readily attracted by the jet. Moreover, regardless of the position of P_d, the decay rates of G_1 and G_2 are quite similar (figure 3.12b), indicating that particle movements spread more or less uniformly along the radial direction from the source; they do not concentrate at specific locations, and simply disperse away at a constant rate. With crossflow, the position of P_d becomes closely connected to the location where the CVP is

substantially dissipated (figures 3.3 and 3.6). The particles interact with the CVP actively, and most of them are confined inside the vortices. Thus, the locations of P_d do not show a stronger dependency on St than on R. However, when the velocity ratio is high, the effect of Re_D appears in a few cases, as explained above. For example, for St = 14.18, P_d (= 6.5D) appears a little further than the position (= 4.0 – 5.0D) of the CVP collapse. As the Re_D is low (Re_D = 1640) in this case, the entrained flux contributing to the CVP formation is small, and the particles with large inertia (St > 10 .0) are not confined in the CVP, but rather spread along the jet.

Unlike P_d, the decaying slope G_1 varies quite widely depending on St, in both lower and higher R cases (and also on Re_D, to some extent, in higher R cases) (figure 3.12b). For the lower R cases, the slope G_1 becomes steeper as the Stokes number increases. As shown in figures 3.3(c) and (d), the coherency of the CVP is enhanced, but it spans a narrow region near the jet exit when the velocity ratio is low. As the particles with St < 1.0 are captured by the vortical structures and those with a higher St are driven mostly by the inertia gained from the jet momentum, the particle concentration decays slowly when St is smaller. In contrast, the slope G_1 becomes milder as the velocity ratio increases to ~ 3.0, as the CVP is further elongated from the jet exit (figure 3.3a, b), and carries the particles away from it. Interestingly, the influence of St is now reversed as compared with the cases of R near 1.0. The particles with a smaller St experience a sharper decay of particle concentration away from the source (figure 3.12b). This is because the upward elevation of the particles by the jet is stronger than that captured by the CVP. Slope G_1 is now more dependent on Re_D; G_1 increases as Re_D decreases. As more flux of the crossflow is entrained to the jet, it strengthens the growth of the CVP and the particles are swept over a wider area.

To further understand the localized particle concentration relative to the evolution of the CVP, we investigated the correlation between vortex trajectory and

particle concentration in the center plane. Figures 3.13 and 3.14 show the particle concentration profiles along the *n*-axis, following the *s*-axis (see figure 3.6(a) for the definition of axes). It is noted that each profile is shifted to locate the *n*-axis origin ($n/D = 0$) on the position of the CVP center, by which the relative position of the particle cluster to the vortex can be compared consistently. When the velocity ratio is high ($R \sim 3.0$), the concentration peaks are located on the windward side of the CVP center, regardless of *St*, up to $s/D = 2.0$ (figure 3.13). After the collapse of the CVP at $s/D \simeq 5.0$, the particles with $St \lesssim 1.5$ migrate toward the CVP center, showing a blunt and lower concentration peak. That is, the particles disperse along the *n*-axis in the center plane after the collapse of the CVP. For $St > 1.5$, however, the peak location is almost the same along the s-axis. After the CVP collapses, the peak value decreases but still shows a sharp profile. This is because the larger particle inertia causes a weak interaction between the particles and CVP. In all cases except for $St = 1.485$, the magnitude of the peak is significantly reduced (up to 25%) after the collapse of the CVP at $s/D \simeq 5.0$; in contrast, the peak magnitude is decreased by approximately 50% for $St = 1.485$. Given this occurrence, the particles with $St = 1.485$ are dragged more by the developing CVP to the windward side, and move to the CVP center with a reaction after the CVP collapse. Recalling figure 3.9(b), it is noted that the leading edge of the C-shaped cluster, which is more conspicuous than that of $St \ll 1$, is located on the leeside of the jet exit.

For lower *R* cases ($R \sim 1.0$), the concentration peak location moves slightly toward the CVP center as *St* (especially for $St < 1.0$) decreases, at $s/D < 2.0$ (figure 3.14). As shown in figure 3.6(b), the CVP is generated by the jet separation, forming a lower-pressure zone along the CVP center, and resulting in the accumulating of particles. After the collapse of the CVP ($s/D \simeq 2.0$), the peaks of $St < 1.0$ match the CVP center, and the peaks of $St > 1.0$ are located at the same position along the *s*-axis. The magnitude of the peak ($St < 1.0$) decreases significantly after CVP collapse,

but that of $St > 1.0$ is reduced less. This is because the particles with low inertia are transported uniformly along the n-axis by a stronger CVP. For $St = 0.965$, similar to the case of $St = 1.485$ ($R \sim 3.0$), the concentration peak of approximately half the magnitude of that at the jet exit ($s/D = 0.5$) moves to the CVP center in the center plane. This phenomenon is observed in figure 3.9(a); the particles are transported along the x and y directions, but remain concentrated on the leading edge of the C-shaped cluster (leeward side of the jet exit).

From the radial distribution of particle distribution in figure 3.11, we can define the specific position (P_o) where the out-of-plane movement (along the y-direction) of the particles is encouraged, such that the radial position of $\hat{\theta}_m$ m appears away from the center ($y/D = 0$) plane (figure 3.15). The position of P_d provides information on the range in which the particles are concentrated; P_o shows how fast the particles are swept by the vortical structures. As shown in figure 3.15(a), it is clear that the CVP plays a dominant role in the early sweeping of particles away from the center plane. When there is no crossflow, or $R \sim 3.0$ (higher R cases), P_o becomes longer (it takes longer from the jet exit) with decreasing St. As the velocity ratio decreases to ~ 1.0 (lower R cases), the trend is reversed. Without crossflow, the flow along the vertical direction is so strong that it forces most of the particles to move upward. Once the particles lose their initial momentum, they tend to spread laterally. Therefore, the transition of the transverse plane with $\hat{\theta}_m$ with a smaller St occurs farther from the jet exit. This is similar to the cases with higher R (with crossflow) at which the CVP develops; however, the jet shear layer in the vertical velocity is stronger than ω_z in the CVP (figure 3.3a, b). In this case, P_o is shorter than that without crossflow, owing to the existence of the CVP upstream of the jet. For $R \sim 1.0$, the CVP becomes sufficiently strong such that the out-of-plane movement of particles is more dominant than the elevation from the upward jet momentum, resulting in a decrease in P_o with a smaller St. Thus, it is understood that the particle

movements and range at which they are preferentially gathered are controlled through the combination of R and St; the stronger and more coherent the vortices in the flow, the more particles ($St < 1.0$) swept out of the center plane.

In addition, when examining all cases with and without crossflow, the particle concentration at P_o shows a correlation (exponential decay) with P_o, as shown in figure 3.15(b). The particle concentration at P_o is quite low for the cases without crossflow, as it appears much farther from the jet exit. As the velocity ratio decreases, the particle concentration at P_o increases exponentially. This also supports our understanding of the particle transportation by the CVP in an upward jet with crossflow. As shown in figure 3.15(a), the position of P_o tends to be saturated, as the Stokes number is higher than approximately 10.0 for the cases with crossflow, indicating the influence of the CVP. Without crossflow, P_o approaches the jet exit quickly with increasing values of St.

3.2.2 Dispersion regime classification based on *St* and *R*

From the particle concentration characteristics identified above, it is possible to classify particle dispersion regimes based on the dependency of P_o/P_d on St and R (figure 3.16). As explained above, P_d corresponds to the location where the CVP is significantly dissipated, and its coherency disappears. Therefore, at $P_o/P_d > 1.0$ (denoted as regime 1), the particles tend to stay on the jet-center plane, even after the CVP has collapsed. In contrast, at $P_o/P_d < 1.0$ (regime 2), the particles are dispersed along the lateral direction (out-of-plane movement) before the CVP is dissipated. Finally, regime 3 denotes when $P_o/P_d \simeq 1.0$, indicating that the particles are distributed between the vortex pair, but are transported outward as soon as they

disappear. As shown in figure 3.16(a), with a higher R (~ 3.0), P_o/P_d is inversely proportional to St; it transitions from regime 1 to 2 with increasing St. This is because P_o increases with decreasing St, owing to the jet shear layer. We observed that the particles with $St \ll 1.0$ were concentrated on the leading edge of the C-shaped cluster after the CVP started to dissipate (figures 3.9b and 3.13). For $St \gg 1.0$, the concentration peak exists above the jet exit at the center plane, but many more particles are dispersed along the transverse (y) direction (resulting in a smaller P_o). For lower R cases, the dispersion pattern changes from regime 1 to 2 as St decreases (figure 3.16a), due to the stronger particle sweeping by the CVP. When $St < 1.0$, the particles are dispersed to the edges of the earlier CVP, and showing the C-shaped cluster (regime 2), but those particles with larger inertia ($St > 1.0$) do not interact with CVP, and stay at the center plane independent of the presence of the CVP (regime 1) (figure 3.9a). Notably, regime 3 approximately corresponds to $St \simeq 1.0$, regardless of R, showing that particles with $St \simeq 1.0$ respond most faithfully to the vortices. Irrespective of R, the particles are captured between the CVP, and then are scattered as soon as it disappears. The particles are still concentrated at the leading edge of the C-shaped cluster even after the CVP collapses (owing to the residual effect), and most of the particles are simultaneously transported in the transverse (y) direction within the leading edge (figures 3.9a and 3.14).

As there is no structure vortex evolution in the cases without crossflow, most of the particles are transported gradually along the jet centerline, and are not swept substantially out of the center plane before the position of P_d is reached (figure 3.16b). When the particles lose their kinetic energy and begin to descend at P_d, only a small number of particles spread out of the jet center. Thus, P_o is measured to be similar to P_d so that Po/P_d is close to 1.0 (regime 3), except for the case of the largest St of 21.59. When $St \gg 1$, the ratio becomes considerably smaller (regime 2), owing to the large particle inertia and Re_d, even though the corresponding mechanism is

different from that in the cases with crossflow (from the interaction with the CVP).

3.2.3 Empirical models of particle dispersion

To describe and predict the particle dispersion caused by the interactions with CVP, we suggest empirical particle dispersion models. The empirical models are defined on two planes; one along the jet centerline (*s*-axis; see figure 3.6(a)) in the jet-center ($y/D = 0$) plane, and another along the *x*-axis in $x - y$ planes ($z/D = 0 - 5.0$ for $R \sim 3.0$ and $z/D = 0 - 2.0$ for $R \sim 1.0$) where the CVP exists. First, we quantitatively evaluate the extent to which the particles disperse along the *n*- and *y*-axis against the *s*- and *x*-axis, respectively. Figure 3.17(a) shows the example of particle concentration distribution (probability density function, p.d.f.) along the *n*-axis for the case of $R = 1.1$ and $St = 0.965$, measured at $s/D = 1.0$. The particle concentration is nicely characterized by the p.d.f., so that the standard deviation (σ_n) of the p.d.f. is a good parameter to assess dispersion level. A smaller σ indicates that the particles are preferentially (locally) concentrated. The result is shown in figure 3.17(b) and it is found that the variation of σ_n along the *s*-axis can be curve-fitted using a power-law equation in the form of $\sigma_n = a_s(s/D)^{b_s}$. Similarly, the standard deviation (σ_y) of the concentration distribution p.d.f. along the *y*-axis is obtained at each position along the *x*-axis, and modelled as $\sigma_y = a_x(x/D)^{b_x}$ (figure 3.17c).

Figure 3.18 shows the variation of coefficients with *St* in the power-law modelling of σ_n and σ_y.When $R \sim 3.0$, the coefficient as increases linearly along St ($a_s \simeq 0.037St + 0.53$) while b_s decreases following $b_s \simeq -0.026St + 0.36$ (figure 3.18a). This agrees with our explanation that the CVP with a weak crossflow

is caused by the entrained flow to the jet-center plane, and thus, the small entrained flux induces the particles of lower *St* to gather more locally within the CVP (along the *n*-axis), as described in Chapter 3.1. On the other hand, the model coefficients of lower *R* (~ 1.0) cases are roughly constant as $a_s \simeq 0.15$ and $b_s \simeq 0.53$, respectively. This is consistent with the fact that the flow around the jet is entrained mostly in the vortices outside the jet-center plane, forming a large CVP, and the particle dispersion pattern in the jet-center plane does not change with *St*. For the model on the $x-y$ planes, it is also found to agree with our understandings. As shown in figure 3.18(b), the coefficient σ_x of σ_y model increases with *St* in the form of a power law ($a_x \simeq 0.34St^{0.06}$) and b_x decreases as $b_x \simeq 0.27St^{-0.07}$ for lower *R* cases. This indicates that the particles barely exist in the leeside area of the jet exit; σ_y increases quite gently along the x-axis while showing a relatively large value. For *R* ~ 3.0 (weak crossflow), the force to push the particles downstream is weaker than that of the lower *R* cases, so that relatively fewer particles spread uniformly downstream. This is well expressed by the models: a_x of higher *R* is larger in all *St*'s and σ_y increases more slowly along the *x*-axis (smaller b_x). They are modelled as $a_x \simeq 0.48St^{0.03}$ and $b_x \simeq 0.22St^{-0.11}$, respectively.

Collecting the above results, we have plotted the modelled σ_n and σ_y for the selected cases in figure 3.19. For *R* ~ 3.0, first of all, a large σ_n is induced up to *s/D* = 5.0 by the weak crossflow entrainment with increasing *St*, which is reversed after the CVP collapses (figure 3.19a). Since σ_n represents the amount of dispersed particles in the jet center plane, this agrees with our observation that the smaller (or larger) the *St*, the particles tend to predominantly gather (or be dispersed more or less uniformly) between the counter-rotating vortices until the collapse of the CVP. After the CVP collapses, σ_n of *St* = 0.012 increases most dramatically, indicating that most of the particles stay in the center plane (corresponding to regime 1) and disperse

much evenly therein. For $R \sim 1.0$, the value of σ_y is larger for the case of higher St and they get closer along the x-axis (figure 3.19b). Although the reversal of σ_y is not clearly observed, it can still explain the particle dynamics under the interaction with the CVP. Particles of $St \ll 1.0$ are swept inside the strong counter-rotating vortices caused by early separation of the jet and crossflow, moving outside of the jet-center plane, and most of the particles are dispersed downstream by the separated flows. Thus, the σ_y increases sharply along the x-axis. As St increases, the particle inertia rapidly grows, so that the particles are preferentially gathered inside the CVP and less are dispersed (σ_y increases slowly along the x-axis). In particular, particles of $St \gg 1.0$ are hardly dragged downstream by the crossflow, and most of them fall immediately near the jet exit.

3.3 Force analysis for understanding the particle dispersion mechanism

3.3.1 Scale analysis of force components on the particles

So far, we have explained the particle dispersion behavior in connection with the dynamics of the coherent vortical structures existing in the upward jet, with and without crossflow. In this section we add to this discussion by estimating the relative order of dominant forces acting on the particles. To estimate the contributions from each force potentially affecting particle movement, we start with force components introduced in a well-known equation for spherical particle motion in a non-uniform flow, as suggested by Maxey & Riley (1983). They considered drag (F_{Drag}), basset

history (F_B), added mass (F_A), fluid acceleration (F_{FA}) and gravitational (F_G) forces. For the drag force, we use the drag coefficient relation of $C_D = (24/Re_p) \cdot (1 + 0.15Re_p^{0.687})$, modified from the Stokes drag law of $C_D = (24/Re_p)$. As explained in Chapter 2.3.1, this relation was drawn based on the experimental data at $1 < Re_p < 800$ (Schiller & Neumann 1933). Thus, in the present analysis, the drag force is calculated as follows:

$$F_{Drag} = \begin{cases} 3\pi\mu\bar{d}_p(u-v) & \text{for } Re_p \leq 1 \\ 3\pi\mu\bar{d}_p(u-v)(1+0.15Re_p^{0.687}) & \text{for } 1 < Re_p < 800. \end{cases} \quad (3.2)$$

In contrast, the added mass ($F_A = 0.5m_f\, d(u-v)/dt$, m_f: mass of the fluid (gas) corresponding to the particle volume) and fluid acceleration ($F_{FA} = m_f\, Du/Dt$, D/Dt: material derivative) forces are assumed to be negligible, as the fluid mass m_f is much smaller than m_p, i.e. $\boldsymbol{O}(m_f/m_p) = 10^{-3}$. The Basset history force contributed by the relative acceleration between the fluid and particles owing to the viscous effect (important for highly viscous or dense particle-laden flows) can also be neglected for relatively dilute (one-way coupling for the present cases) flows where particle collisions are not considered (Coimbra & Rangel 1998). It is noted that the Faxen correction term (including $\nabla^2 u$) is not considered in calculating the drag and added mass forces, as it is important only when the forces are induced by the flow disturbance in a dense non-uniform flow (Bagchi & Balachandar 2003). The gravitational body force is calculated as $F_G = (m_p - m_f)g \simeq m_p g$. In addition, there are additional forces that may act on the particles in a complex fluid flow. Given the strong shear (velocity gradient) flows around the particle, the shear-induced Saffman lift force (F_{LS}) (Saffman 1965) and the Magnus lift force (F_{LM}) by particle rotation (particle inertia) (Rubinow & Keller 1961) are candidates. The Saffman lift force is expressed as $F_{LS} = 1.61\mu\bar{d}_p^2[(u-v)\omega]/\sqrt{\nu/\omega}$, where ω is the vorticity of the continuous-phase flow (background flow). The Magnus lift force is defined as

$F_{LM} = (\pi/8)\rho_g \bar{d}_p^3[\Omega_r(v-u)]$, where Ω_r is the relative rotation of the particle as $\Omega_r = \Omega_p - 0.5\omega$ (Ω_p= particle rotation velocity). These lift forces are estimated based on the velocity fields of the single-phase jet flow. Finally, the turbophoresis force (Reeks 1983), acting in the direction of decreasing particle turbulent kinetic energy, is also meaningful to consider. In general, the turbophoresis force transports particles towards a solid wall via eddies in the flow. It is proportional to the gradient of the turbulent kinetic energy and is modelled as $F_{Turb} = -\rho_p \bar{d}_p^3\, \partial(\Gamma u'u')/\partial x = -\rho_p \bar{d}_p^3\, \partial(v'v')/\partial x$, where $\Gamma = \tau_f/(\tau_f + \tau_p)$ and τ is the time scale (Slater, Leeming & Young 2003).

Before we calculate the force components addressed above, we estimate their orders of magnitude to identify the dominant components in the present configuration. For the Reynolds number range of $Re_p = \boldsymbol{O}(10^{-3} - 10^{-1})$, it is estimated that $F_G/F_{Drag} = \boldsymbol{O}(10^{-1})$, $F_{LS}/F_{Drag} = \boldsymbol{O}(10^{-0.5})$, $F_{LM}/F_{Drag} = \boldsymbol{O}(10^{-5})$ and $F_{Turb}/F_{Drag} = \boldsymbol{O}(10^{-2})$. Thus, it is considered that the drag force (F_{Drag}) is the most dominant force. For cases of $Re_p = \boldsymbol{O}(1-10)$, however, the ratios are estimated as $F_G/F_{Drag} = \boldsymbol{O}(10^{1})$, $F_{LS}/F_{Drag} = \boldsymbol{O}(10^{-0.5})$, $F_{LM}/F_{Drag} = \boldsymbol{O}(10^{-3})$ and $F_{Turb}/F_{Drag} = \boldsymbol{O}(10^{-2})$, so that the gravitational force (F_G) is dominant, owing to the larger particle size. For all cases, the other forces such as F_{LS}, F_{LM} and F_{Turb} are estimated to be considerably smaller than F_{Drag} and F_G in our configuration. Similarly, previous studies have generally ignored the contributions of lift forces in analyzing particle dynamics (Zaichik & Alipchenkov 2005; Goswami & Kumaran 2011; Wang, Zheng & Wang 2017b; Liu *et al*. 2020). In the following, we focus on the variation of F_{Drag} and F_G to explain the particle dispersion mechanisms according to *St* and *R*. We calculate the local particle forces ($F'_{Drag} = \hat{\Theta} F_{Drag}$ and $F'_G = \hat{\Theta} F_G$) by multiplying each force model (F_{Drag} and

F_G , being assumed to act on a single particle) with the dimensionless local concentration ($\hat{\Theta}$). Thus, the forces are weighted by the local particle concentration, by which we can compensate for the particle density differences among the IWs. Finally, the local particle forces are normalized as $F'' = F'/(\rho_f \bar{u}_m^2 \bar{d}_p^2)$ to determine the effect of particle inertia (the *St* effect) alone, i.e. not complicated by the fluid flow (the Re_D effect).

3.3.2 Dominant force terms depending on *St* and *R*

Figure 3.20 shows the time-averaged horizontal distribution of the vertical drag force ($\bar{F}''_{Drag,z}$) and gravitational force ($\bar{F}''_G$) along the vertical direction (in the centre plane) for the cases without crossflow. The particle forces exerted along the *z*-direction are larger than those in other directions, as the particle movements (or velocities) in the *x*- and *y*-directions are comparatively negligible. When the Stokes number is quite small (*St* = 0.013), a strong drag force is applied near the jet exit, which sustains up to *z/D* = 5.0 (figure 3.20a). The gravitational force is negligible throughout the measurement domain. As the particles are momentarily ejected in the jet, the particle velocity in the *z*-direction is slightly higher than that in the fluid near the jet exit, and is lessened away from it. When *St* is ~ $\boldsymbol{O}(1)$, the gravitational force becomes comparable to the drag force, whereas the drag force remains slightly larger (figure 3.20b, c). Interestingly, the direction of the drag force changes in the positive *z*-direction at *z/D* > 5.0, where the particle velocity is drastically decelerated by losing its inertia. For *St* = $\boldsymbol{O}(10)$, $\bar{F}''_G$ becomes much greater than $\bar{F}''_{Drag,z}$ (figure 3.20d, e). As mentioned above, the heavy particles are dragged in the downward direction while being decelerated, and, thus, the positive drag force acts on the

particle in the entire region of the jet flow (figure 3.20e). As the crossflow complicates the flow, the strength and direction(s) of $\bar{F}''_{Drag,z}$ and $\bar{F}''_{G}$ are affected by the evolution of the vortical structure. Figure 3.21 show the distribution of the $\bar{F}''_{Drag}$ vectors, together with the contours of particle concentration for the selected cases of $St \ll 1.0$ (figure 3.21a, c and e) and $St \simeq 1.0$ (figure 3.21b, d and f) at the center plane. It is clearly shown that the region of higher particle population is related to the deflection of the upward jet owing to the crossflow. For $St \ll 1.0$ and $R = 3.3$ (weaker CVP), the drag force acts along the downward direction up to z/D of ~ 3.0, by which a larger particle concentration is measured (figure 3.21a). This results in particle gathering near the jet exit and does not contribute to the dispersion along the transverse direction (figures 3.9b and 3.11). As the CVP becomes stronger ($R \simeq 1.0$), it is found that the drag force is also directed more toward the horizontal (x) direction at $z/D \simeq 0.8$ (figure 3.21c). Although the Stokes number approaches 1.0, unlike in the cases without crossflow ($\bar{F}''_{Drag} \sim \bar{F}''_{G}$), the drag force remains dominant. With $R = 3.0$, the drag force mostly acts in the downward direction, as in the case of $St \ll 1.0$, but it reverses its direction at $z/D \simeq 2.0$, at which the jet shear-layer vortices develop and the jet is deflected (figure 3.21b). As the velocity ratio is reduced ($R = 1.1$), a larger $\bar{F}''_{Drag}$ is exerted on the particles along the downward direction following the hairpin vortex (figure 3.21d), which is different from the case of $St \ll 1.0$. To understand this difference in detail, we compare the vortical structures with the velocity vectors of the two phases in figures 3.21(e) and (f), for the same conditions of figures 3.21(c) and (d), respectively. As shown, the particle ($St = 0.01$) velocity near the jet exit is quite similar to the fluid velocity (figure 3.21e). In this case, the particles follow the hairpin vortex head perfectly, so that the difference between the solid and gas velocities is negligible. Thus, owing to $\bar{F}''_{Drag}$, the particles are pushed into the hairpin vortex, so that the concentration peak appears

there (leading edge of C-shaped cluster), only near the jet exit (at *s/D* = 0.5) (figures 3.9a and 3.15a). As the Stokes number is closer to 1.0, the particles' response reflects more of their larger inertia, such that the particle velocity becomes larger than the fluid velocity (figure 3.21f). Here, the $\bar{F}''_{Drag}$ drives the particle to the leading edge of the hairpin vortex, and the particles gather at the windward side (leading edge) of the CVP center. Although the CVP is weakened at *s/D* = 2.0, a similar phenomenon is still observed (figure 3.9a).

To understand the lateral movements of the particles, responding to the CVP, the particle concentrations with drag force vectors on the *z/D* = 0.5 plane are plotted for the case of *R* = 1.0 – 1.2, while varying the Stokes number (figure 3.22). When *St* = 0.01, the drag force acts in the two directions, i.e. toward the side edge of the CVP (figure 3.22a). For *St* = $\boldsymbol{O}(1)$, the $\bar{F}''_{Drag}$ generally acts toward the leading edge of the CVP (*C*-shaped cluster) (figure 3.22b-d). In particular, a larger $\bar{F}''_{Drag}$ is exerted on the particles for *St* = 0.965. Thus, the particle concentration on the leading edge of the *C*-shaped pattern, even after the CVP collapse, is attributed to this large drag force. As *St* increases, the particle concentration is higher near the jet exit (figure 3.22e, f). At this location, the particles do not react to the CVP owing to their large inertia, and most fall immediately by gravity.

To verify the validity of the force analysis we performed in this study, we reconstructed the trajectory of a single particle based on the particle movement equation (Maxey & Riley 1983) (figure 3.23). As previously discussed, only the drag force and gravitational body force are considered in the observed flow, so the particle motion equation is simplified as:

$$m_p \frac{d\mathbf{v}}{dt} = -3\pi\mu d_p(\mathbf{v} - \mathbf{u}) + m_p\mathbf{g}. \tag{3.3}$$

Integrating equation (3.3) over time yields the particle velocity vector as a function of time (equation 3.4), and integrating equation (3.4) again yields the particle

position coordinates as a function of time (equation 3.5):

$$\mathbf{v}(t_2) = \mathbf{v}(t_1) - (3\pi\mu d_p/m_p)(\mathbf{v}(t_1) - \mathbf{u}(t_1))dt + \mathbf{g}dt \tag{3.4}$$

$$\mathbf{s}(t_2) = \mathbf{s}(t_1) + \mathbf{v}(t_1)dt - (3\pi\mu d_p/m_p)(\mathbf{v}(t_1) - \mathbf{u}(t_1))dt^2 + \mathbf{g}dt^2. \tag{3.5}$$

Since this study mainly observes CVP effects, we targeted low velocity ratio ($R \sim 1$) flows where the particle behavior changes a lot with St due to CVP, and considered the $z/D = 0.5$ plane (figure 3.22), where the particle behavior changes are clearly observed even among the top-view planes. Since the particle trajectories were computed numerically, the time step size was set to 0.2 s and the number of iterations to 50. Only the airflow time-averaged velocity field ($\boldsymbol{u}(x, y)$) was used as input data. The initial particle location was set to multiple locations inside the jet pipe exit, and the initial velocity was set to 0 for both the x and y axes. Since the particle's motion along the z-axis is not considered, the gravity term is ignored in equations 3.3 through 3.5.

We computed particle trajectories for the $St = 0.01$ and 0.97 cases (figure 3.22a and c), where the drag force is dominantly applied to the particles. In the $St \ll 1$ case, the drag force acts in the crossflow direction, causing the particles to disperse rapidly in the crossflow direction as well as inside the CVP, regardless of the particle starting point (Figure 3.23a). In the $St \approx 1$ case, particles originating near the jet leading edge disperse relatively quickly into the CVP. However, particles originating from the jet center and near the jet trailing edge showed a more jet-centered or poorly dispersed pattern. Since the particle trajectories reconstructed by numerical methods show the same particle dispersion pattern as the particle mean concentration field described in this study, the particle force analysis described in this paper is considered to be sufficiently validated.

Finally, we describe the out-of-plane migrations of the particles, based on the concentration distributions overlapped with the drag force vectors on various x–z and

x–y planes. Figures 3.24 and 3.25 show cases of R = 3.0 and 1.1, respectively, when the Stokes number is approximately 1.0. When R = 3.0 (St = 1.485), most of the articles reside on the center plane, as the strength of $\overline{\omega}_z^*$ is less than half of that of $\overline{\omega}_y^*$ (figure 3.24). As shown in figure 3.24(b), the particles are pushed asymmetrically to the center of the jet by the drag force from the edge of the CVP, along the vertical range of z/D = 0 – 2.0. Thus, as combined with $\overline{\omega}_y^*$, the particles are more concentrated at the windward side of the CVP center (approximately at x/D = 0). After the vortices in the flow dissipate beyond a z/D of ~ 4.0, $\hat{\Theta}$ decreases drastically, and shows a relatively uniform distribution in the domain. When the CVP becomes stronger, the particles are affected by both the transverse (figure 3.25a) and vertical (figure 3.25b) vortices, whose strengths are more or less comparable. Thus, it is found that the drag force acts primarily toward the leading edge of the CVP (hairpin vortex). After the CVP disappears downstream of z/D = 2.0, regardless of R, the drag force that drives the particle migration becomes negligible. The particles are concentrated on the CVP center (leading edge of *C*-shaped cluster) by the reaction of the drag force, and are uniformly transported in the transverse direction with the collapse of the CVP (regime 3) (figures 3.9, 3.13 and 3.14).

3.3.3 Summary of particle dispersion pattern

Our understanding on the particle dispersion is graphically summarized in figure 3.26. Without crossflow, there are no coherent vortices along the z-direction, and thus, the typical vertical jet velocity profile determines the overall particle dynamics. That is, the drag and gravitational forces (two forces identified as dominant in the present configuration) act along the negative z-direction, so that the

concentration is not dispersed out of the center plane, and the concentration decays gradually along the jet centerline. In most cases considering *St*, the particle dispersion belongs to regime 3, as forced by the balance in the gravity and jet inertia, and is not induced by the vortex-induced flow (figure 3.26a). For the highest St = 21.59, the particles start to spread earlier from the jet exit to the lateral direction, owing to the heavy particles; thus, they approximately belong to regime 2.

With crossflow, the CVP formation leads to different components of vorticity in the flow becoming dominant, so that $\overline{\omega}_z^* \sim 0.5\overline{\omega}_y^*$ at $R \sim 3.0$, and $\overline{\omega}_z^* \gtrsim \overline{\omega}_y^*$ at $R \sim 1.0$. As the velocity ratio decreases, the drag force along the *x*- and *y*-directions becomes larger than that along the *z*-direction, so that the particles are transported out of the jet center, following the movements of the CVP. For R of ~ 3.0, the particles are initially confined in the CVP regardless of *St*, but it takes longer for more particles (with a lower *St*) to spread out of the center plane, owing to the effects of the transverse vortices; $St < 1.0$ (> 1.0) belongs to regime 1 (2) (figure 3.26b). Although the particles with $St \lesssim 1.0$ disperse according to the *C*-shaped cluster after the CVP collapses, the particles are preferentially concentrated at the center plane for $St < 1.0$ by the entrained crossflow into the jet center which contributed to form the CVP, but a number of particles with $St \simeq 1.0$ move along the transverse direction. For $R \sim 1.0$, owing to the large hairpin vortex, most of the particles gather inside the vortex structure. Contrary to the higher R cases, the particles follow the movement of the CVP faithfully for lower *St*, and the particles are swept out of the center plane earlier, so that the case of $St > 1.0$ (< 1.0) represents regime 1 (2) (figure 3.26c). Finally, the particles with $St \simeq 1.0$ are dragged toward the leading edge of the CVPs by the vortex structures, regardless of R. Therefore, the particles are preferentially concentrated at the leading edge of the vortex pairs, but only before the CVP is destroyed (regime 3). In this context, we suggest that particle dispersion behavior is influenced by the evolution process of the CVP rather than the CVP itself.

This agrees with the finding that two R-classes ($R \sim 1.0$ and 3.0) with different development mechanisms and coherence (strength) of the CVP result in the opposed particle dispersion patterns according to St. Although the level of coherency of the CVP decreases faster under the partial crossflow, which is a specific condition compared with the interaction with a full crossflow, the CVP development in the near field shares the same mechanism. Smith & Mungal (1998) also affirmed that the CVP itself does not enhance the mixing compared with the free jet, since the CVP is in the far-field region. Rather it is the structural formation of the CVP that corresponds to the enhanced mixing in the near field. Thus, we believe that the particle dispersion patterns established in the present study could be applied to other types of flows sharing the configuration of 'jet in crossflow', in which the CVP develops.

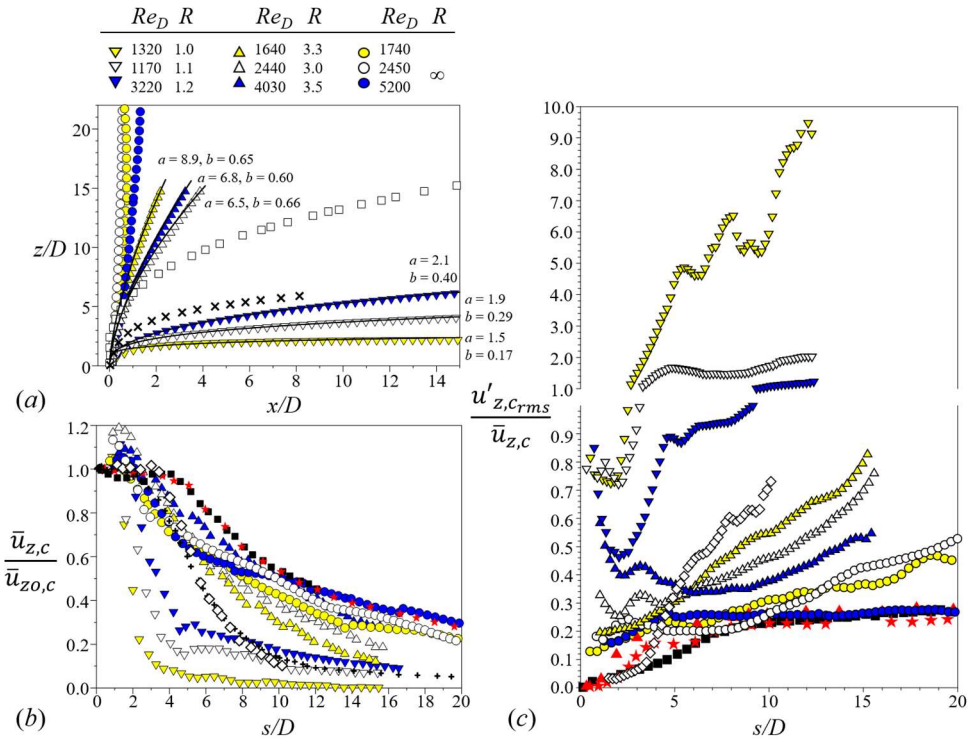

Figure 3.1. Jet centerline characteristics of the airflow: (*a*) jet centerline trajectory; (*b*) jet vertical velocity ($\bar{u}_{z,c}/\bar{u}_{zo,c}$) decay along the jet centerline; (*c*) vertical turbulence intensity ($u'_{z,c_{rms}}/\bar{u}_{z,c}$) along the centerline. In (a), ×, Yuan & Street (1998) (R = 3.3); □, Su & Mungal (2004) (R = 5.7). In (b, c), ■, Fellouah *et al*. (2009) (Re_D = 10,000); ★, Mi, Xu & Zhou (2013) (Re_D = 6000); ▲, (Tong & Warhaft 1994) (Re_D = 140,000) for a vertical jet flow, and ♦, Keffer & Baines (1963) (R = 4.0); +, Muppidi & Mahesh (2007) (R = 5.7) for a round jet in crossflow.

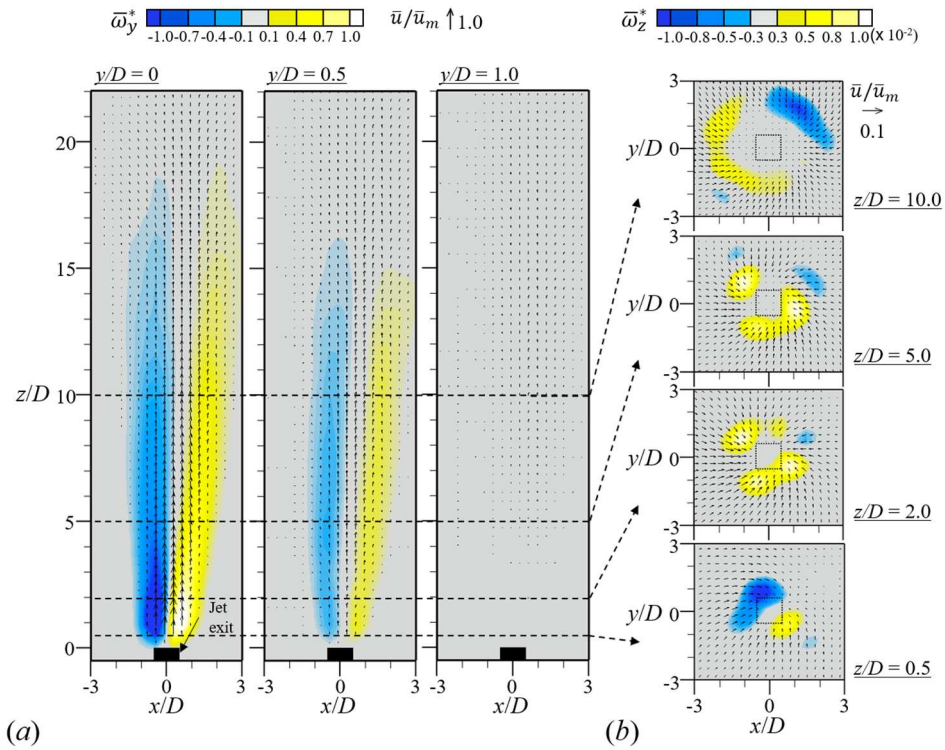

Figure 3.2. Vorticity ($\bar{\omega}_y^* = \bar{\omega}_y D/\bar{u}_m$ or $\bar{\omega}_z^* = \bar{\omega}_z D/\bar{u}_m$) contours and velocity vectors in a time-averaged air jet flow without crossflow (Re_D = 2450): (*a*) *x-z* planes at *y/D* = 0, 0.5 and 1.0; (*b*) *x-y* planes at *z/D* = 0.5, 2.0, 5.0 and 10.0. Velocity vectors are normalized by $\bar{u}_m$.

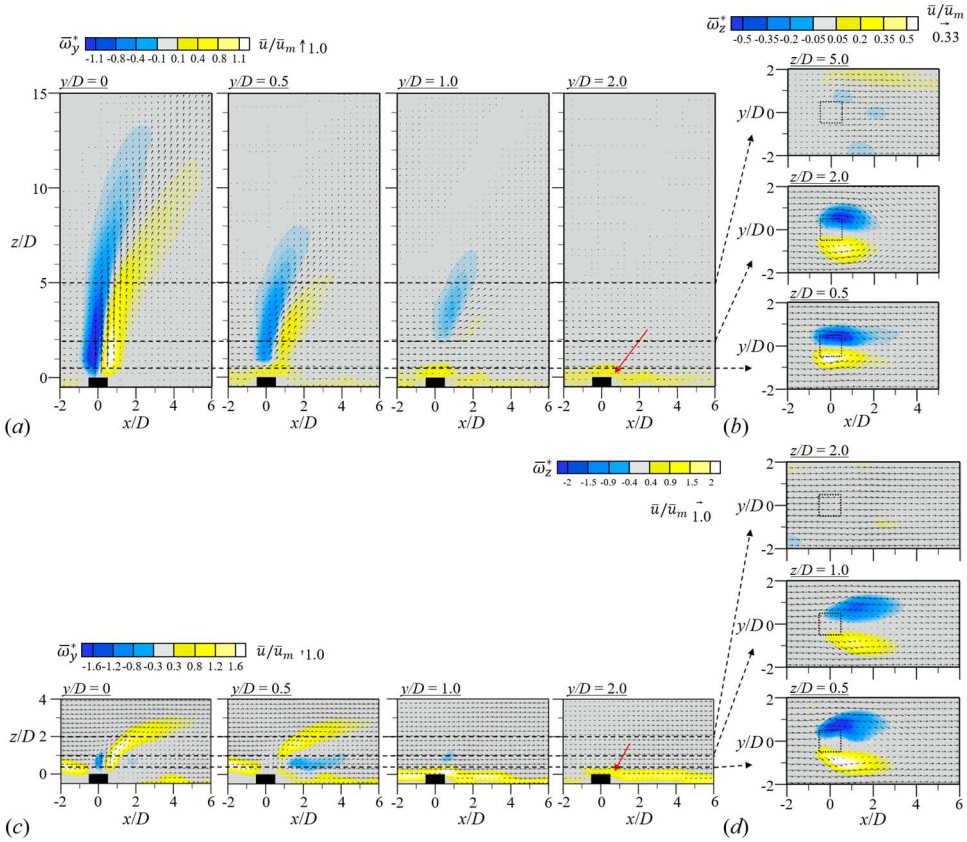

Figure 3.3. Vorticity ($\bar{\omega}_y^* = \bar{\omega}_y D/\bar{u}_m$ or $\bar{\omega}_z^* = \bar{\omega}_z D/\bar{u}_m$) contours and velocity vectors in a time-averaged air jet flow with crossflow ($Re_D = 2450$): (*a,b*) $R = 3.0$ ($Re_D = 2440$); (*c,d*) $R = 1.1$ ($Re_D = 1170$). Velocity vectors are normalized by $\bar{u}_m$.

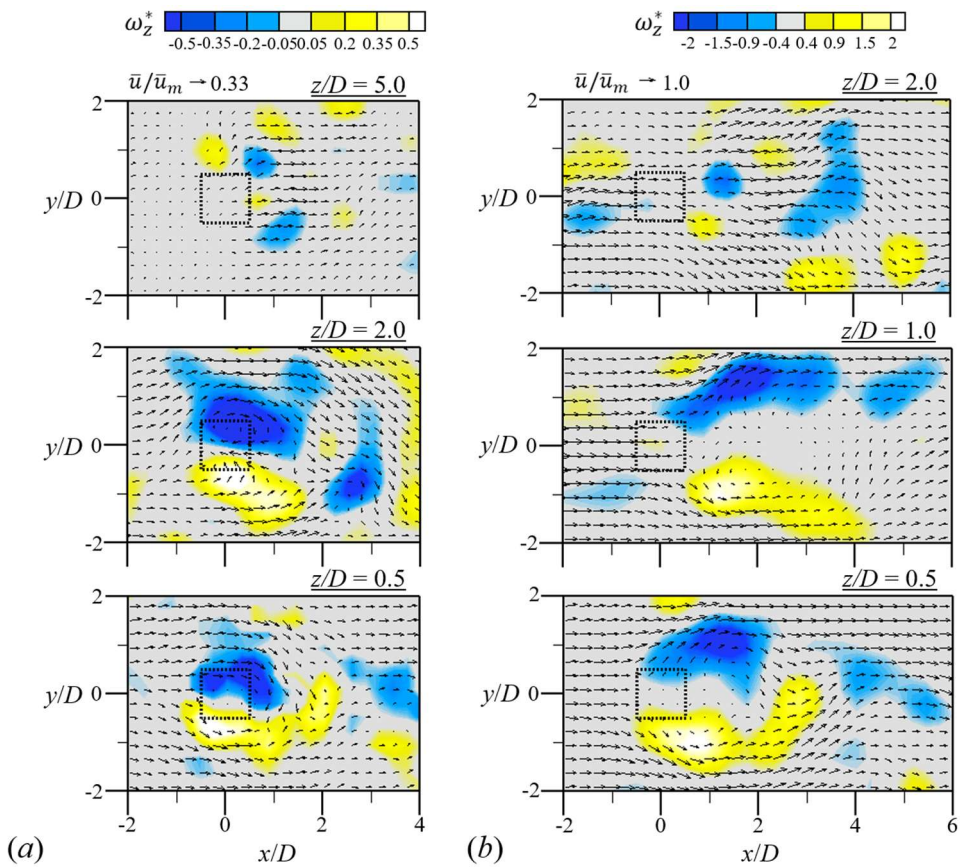

Figure 3.4. Instantaneous vorticity ($\omega_z^* = \omega_z D/\bar{u}_m$) contours and velocity vectors in an instantaneous air jet flow with crossflow in *x*-*y* planes at various *z* coordinates: (*a*) $R = 3.0$ ($Re_D = 2440$); (*b*) $R = 1.1$ ($Re_D = 1170$). Velocity vectors are normalized by $\bar{u}_m$.

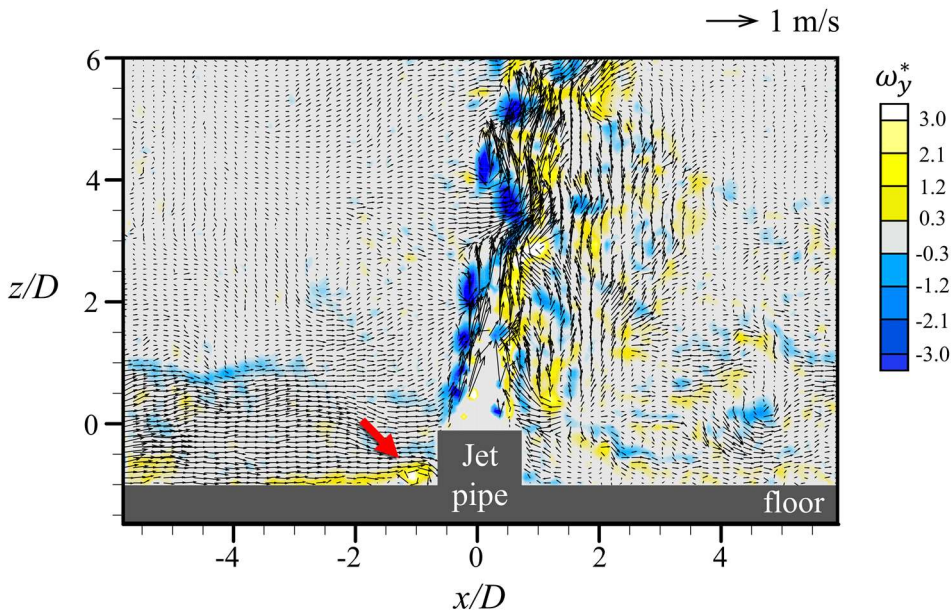

Figure 3.5. Instantaneous vorticity ($\omega_y^* = \omega_y D/\bar{u}_m$) contours and velocity vectors in an instantaneous air jet flow with crossflow in an *x*-*z* plane at *y/D* = 0. A red arrow denotes the horseshoe vortex.

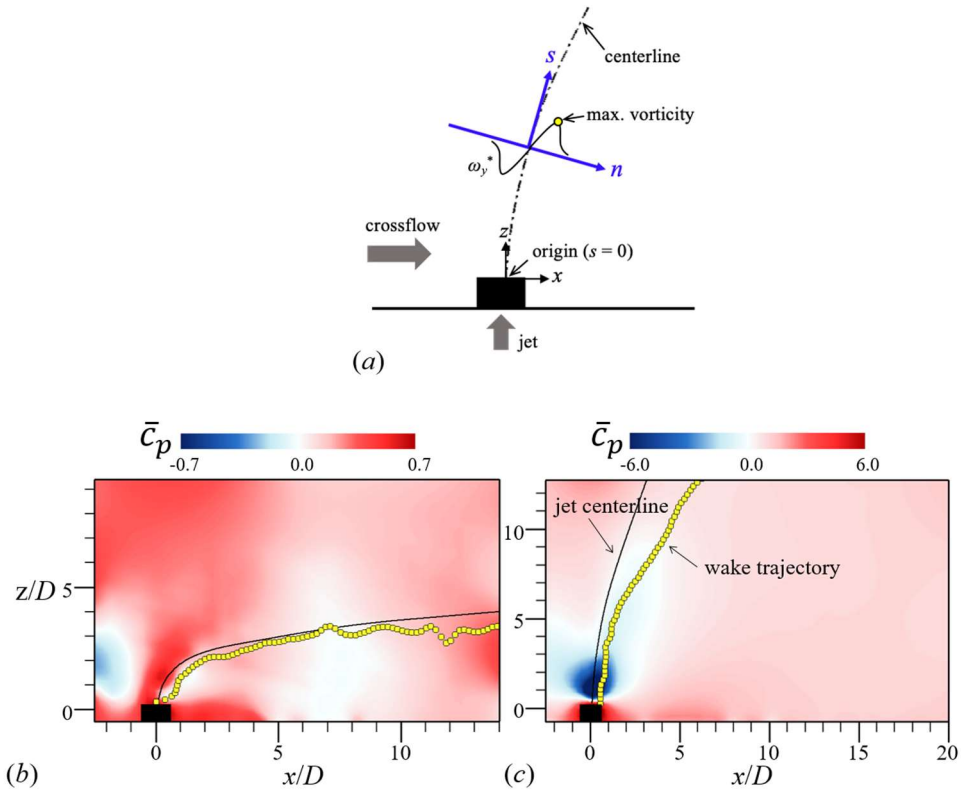

Figure 3.6. (*a*) Schematics of $s - n$ coordinates along the jet centerline. (*b,c*) Time-averaged pressure coefficient ($\bar{c}_p$) contours of airflow with crossflow at the center plane ($y/D = 0$): $R = 1.1$ and $Re_D = 1170$ (*b*); $R = 3.0$ and $Re_D = 2440$ (*c*). In (*b,c*), the solid line and circles denote the centerline and vortex trajectory.

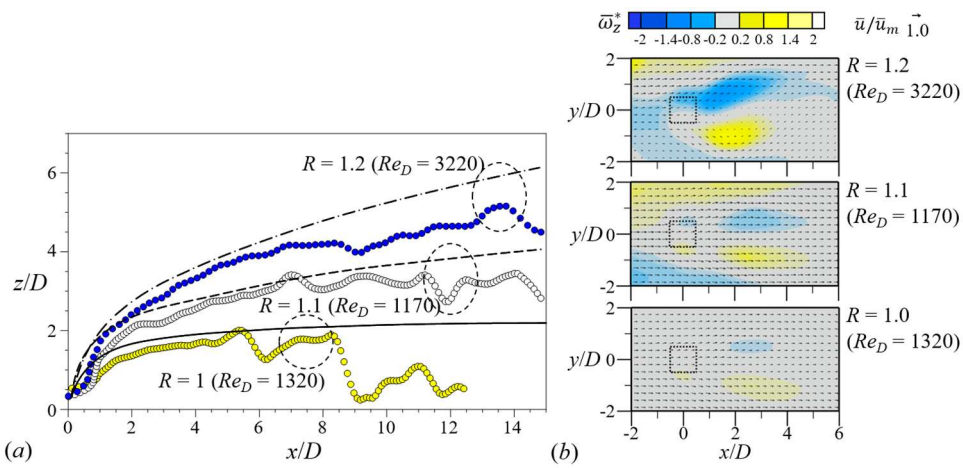

Figure 3.7. Dynamics of the CVP for lower R cases: (a) trajectories of the jet centerline (lines) and vortex (symbols) at the center-plane ($y/D = 0$); (b) vorticity contours ($\overline{\omega}_z^*$) and velocity vectors on the x-y plane (at $z/D = 2.0$).

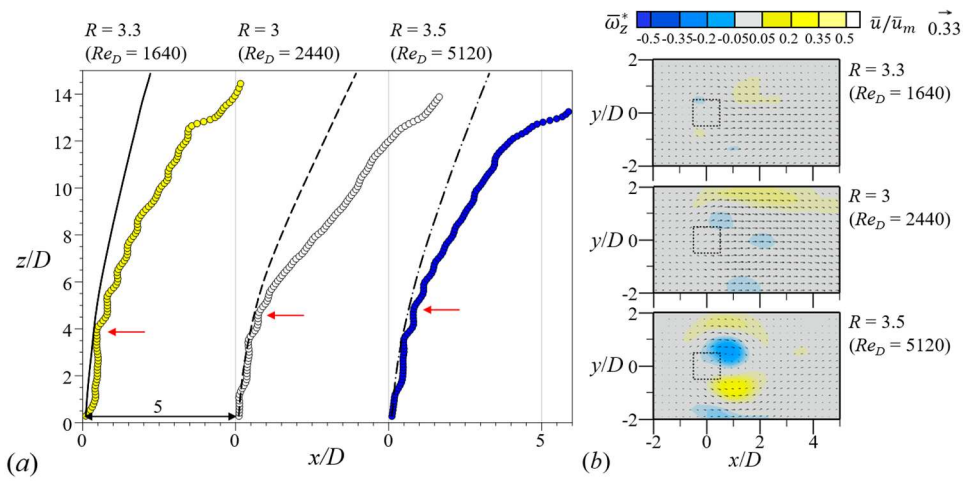

Figure 3.8. Dynamics of the CVP for higher R cases: (a) trajectories of the jet centerline (lines) and vortex (symbols) at the center-plane ($y/D = 0$); (b) vorticity contours ($\overline{\omega}_z^*$) and velocity vectors on the x-y plane (at $z/D = 5.0$).

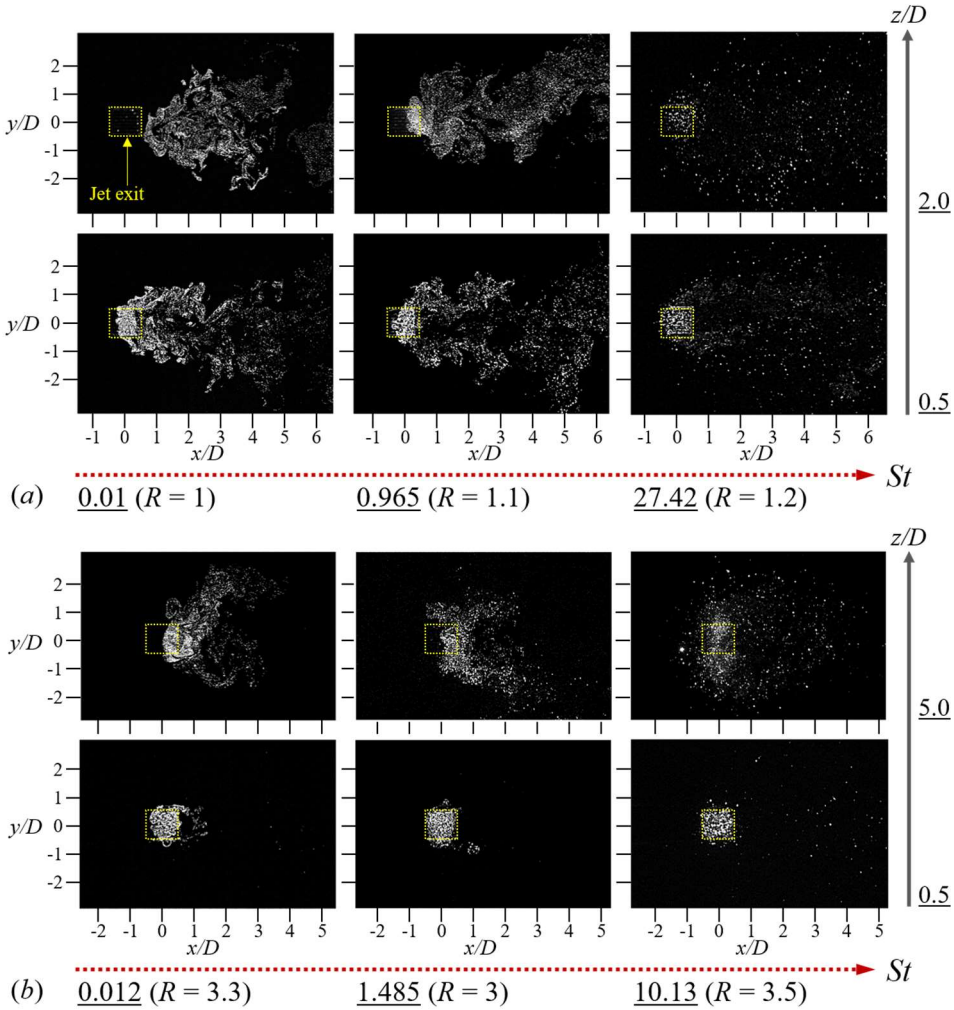

Figure 3.9. Raw images measured for the solid particle dispersion on *x–y* planes for selected cases with crossflow: (a) $R \sim 1.0$. (b) $R \sim 3.0$.

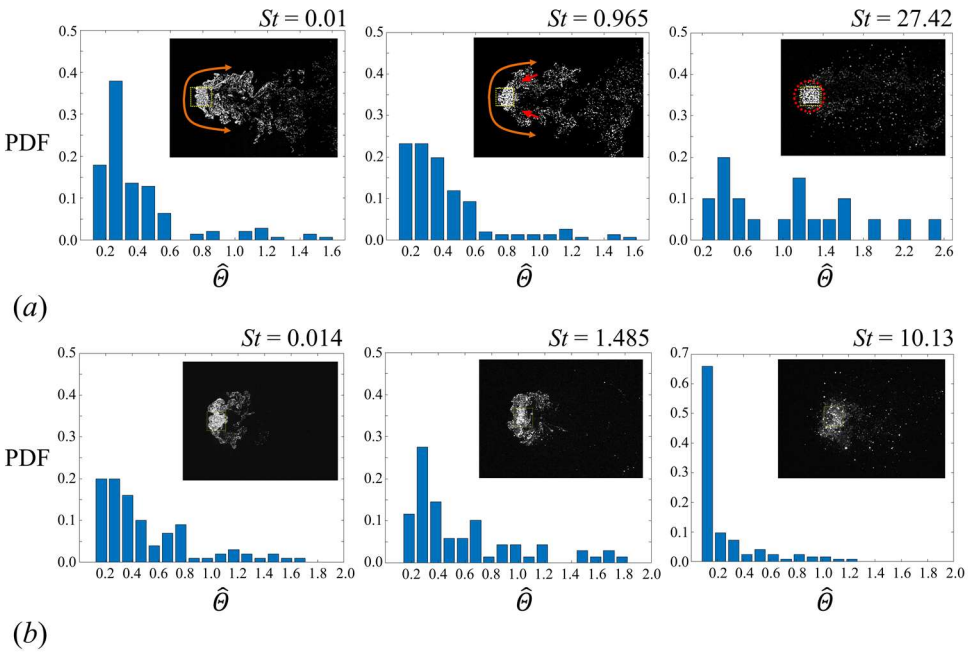

Figure 3.10. Probability density function bar graphs of the time-averaged top-view concentration data: (a) $R \sim 1.0$ (at $z/D = 0.5$). (b) $R \sim 3.0$ (at $z/D = 2.0$). Insets show raw images of the solid particles.

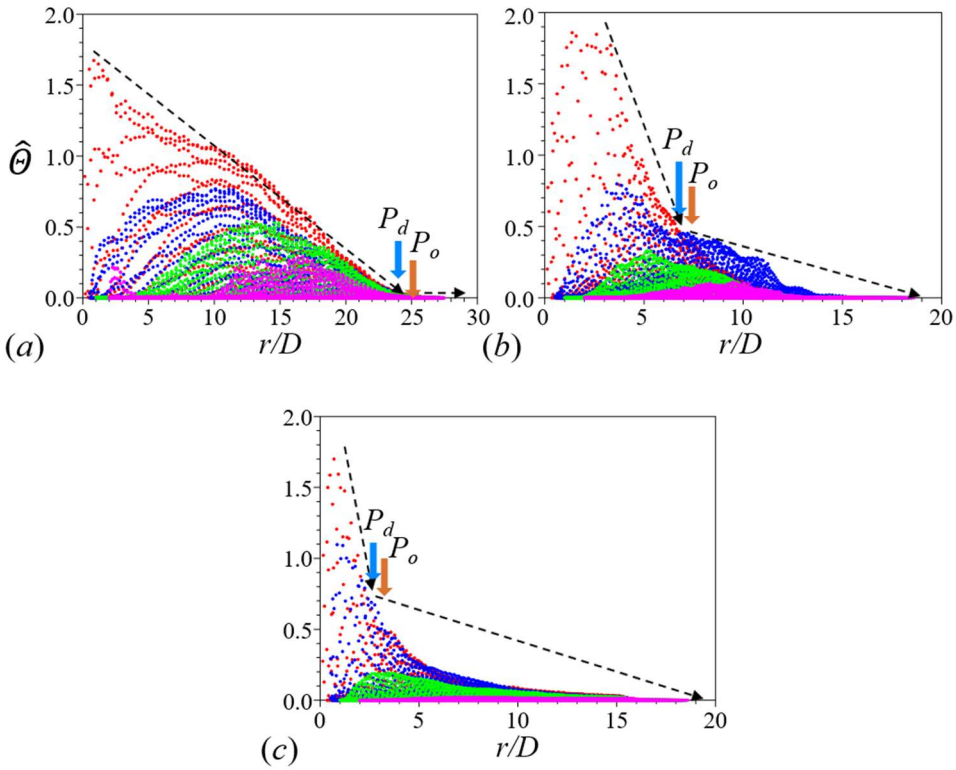

Figure 3.11. The normalized particle concentration ($\hat{\Theta}$) on *x-z* planes along the radial (*r*) direction, with the locations of P_d and P_o denoted: (*a*) without crossflow (Re_D = 2450 and St = 1.5); (*b*) R = 3.0 (Re_D = 2440 and St = 1.485); (*c*) R = 1.0 (Re_D = 1170 and St = 0.965). ●, at y/D = 0; ●, 0.5; ●, 1.0; ●, 2.0.

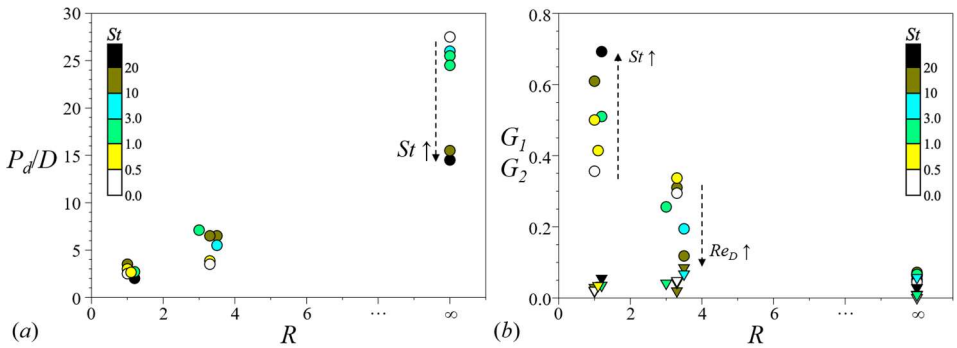

Figure 3.12. Characteristics of particle concentration decay depending on R: (a) location (P_d) where the decaying slope changes; (b) steep (G_1, ●) and slow (G_2, ▼) decaying rate of particle concentration. The colors of the symbols represent the corresponding St.

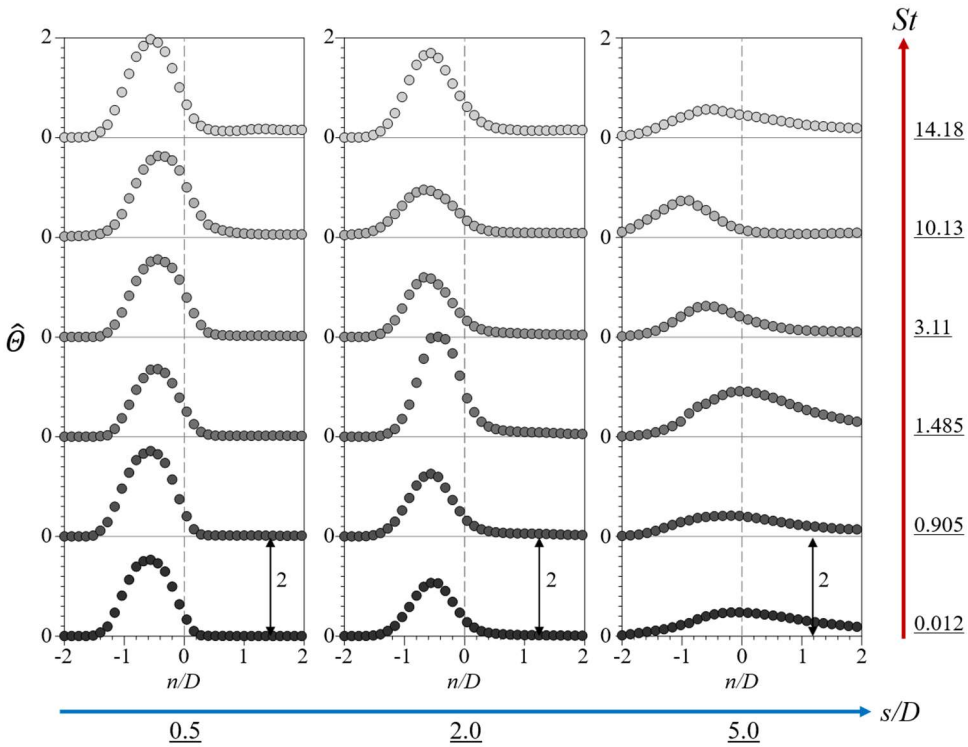

Figure 3.13. Particle concentration profiles along the *s*-axis for R = 3.0 – 3.5, depending on *St*.

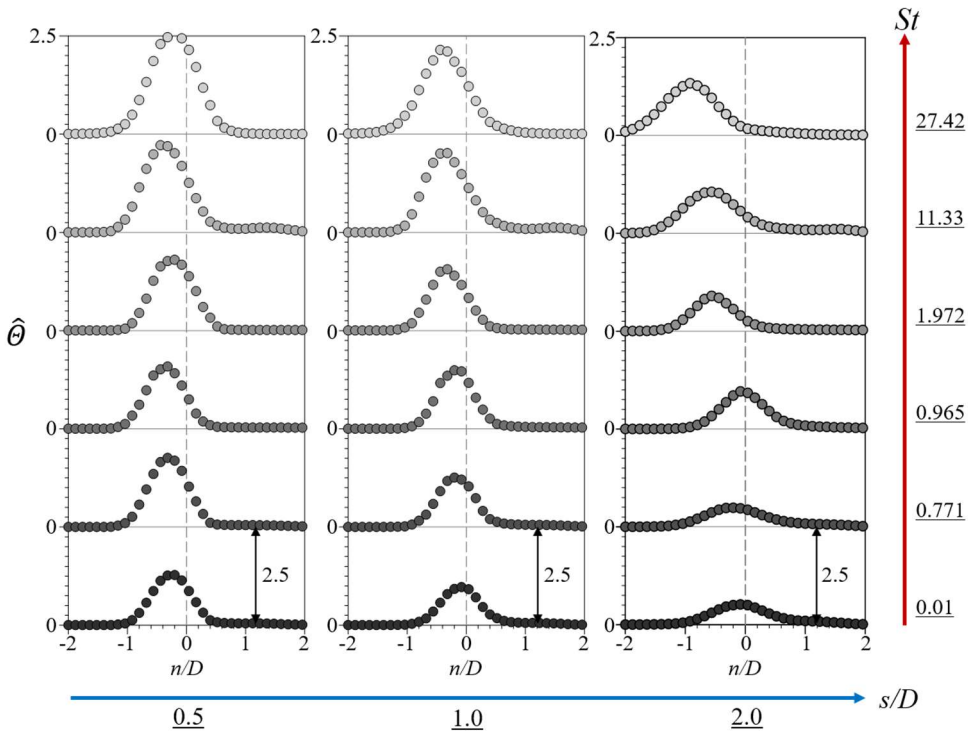

Figure 3.14. Particle concentration profiles along the *s*-axis for R = 1.0 – 1.2, depending on *St*.

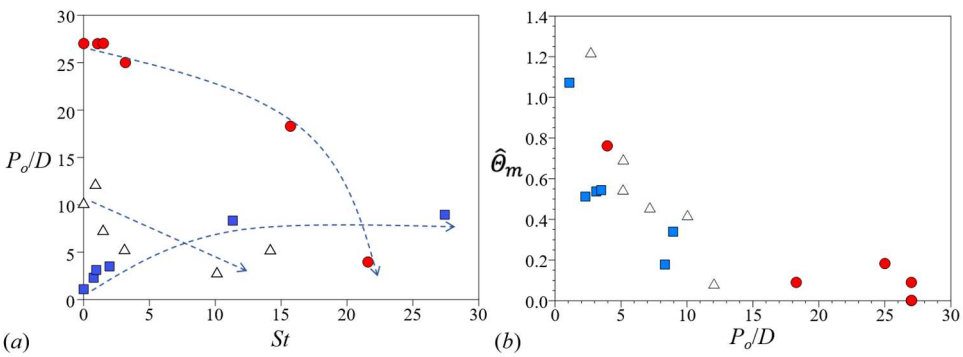

Figure 3.15. Characteristics of the particle sweeping by vortex: (*a*) variation of P_o with R and St; (*b*) particle concentration at P_o. ●, $R = \infty$ (no crossflow); △, $R \sim 3.0$ (higher R cases); ■, $R \sim 1.0$ (lower R cases). In (*a*) the dashed lines denote the trend of P_o variation along St.

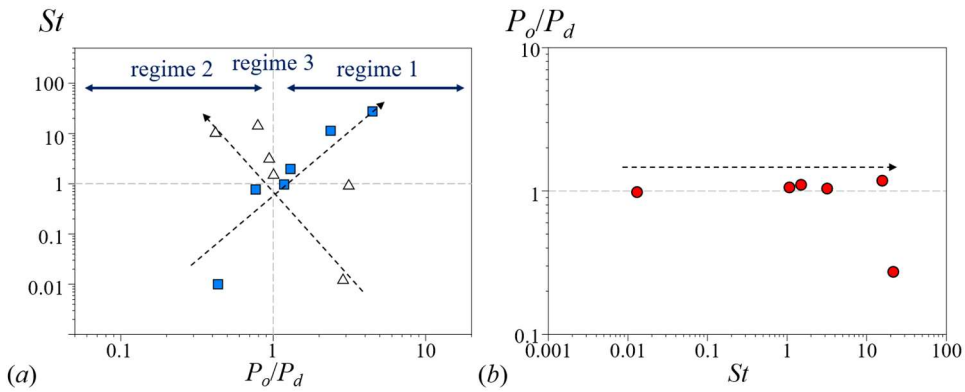

Figure 3.16. The evolution of ratio of P_o to P_d which is the criterion of the preferential concentration regime along *St*: (*a*) with a crossflow; (*b*) without a crossflow. The ● denotes no crossflow; △, $R \sim 3.0$; ■, $R \sim 1.0$.

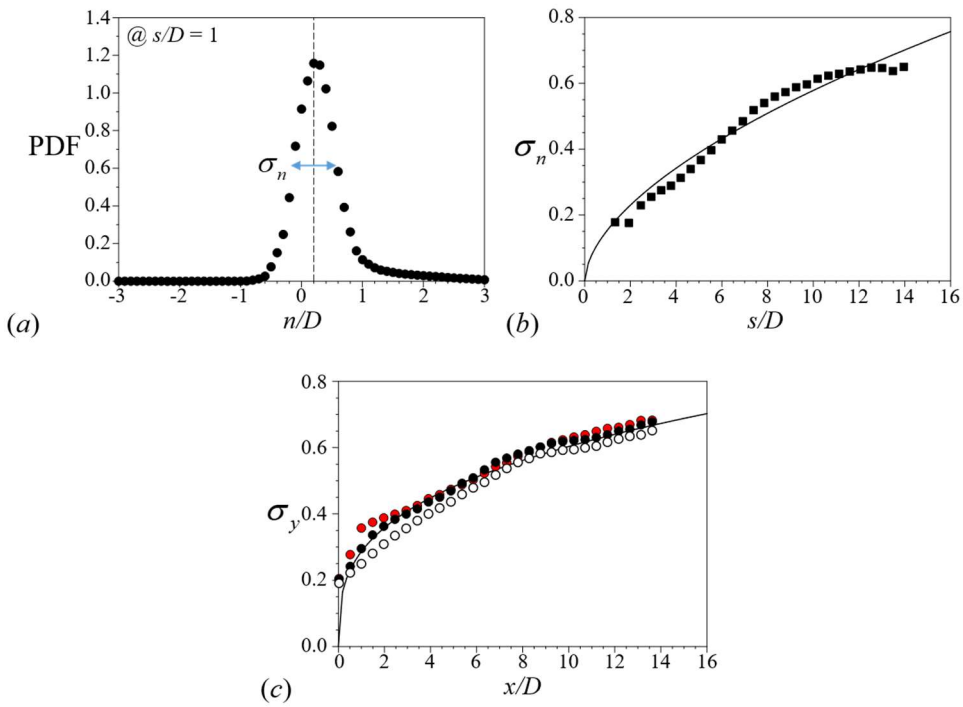

Figure 3.17. Development of empirical particle dispersion model based on standard deviation (σ) of particle concentration: (*a*) probability density function (p.d.f.) of particle concentration profile along *n*-axis at *s/D* = 1.0; (*b*) variation of σ_n along *s*-axis with empirical dispersion model (solid line) along the jet centerline on *y/D* = 0 plane; (*c*) variation of σ_y along *x*-axis with empirical dispersion model (solid line) on the planes of *z/D* = 0, 1.0 and 2.0. In (*c*), ●, at *z/D* = 0; ●, 1.0; ○, 2.0. Shown in the figure is the case for *R* = 1.1 and *St* = 0.965.

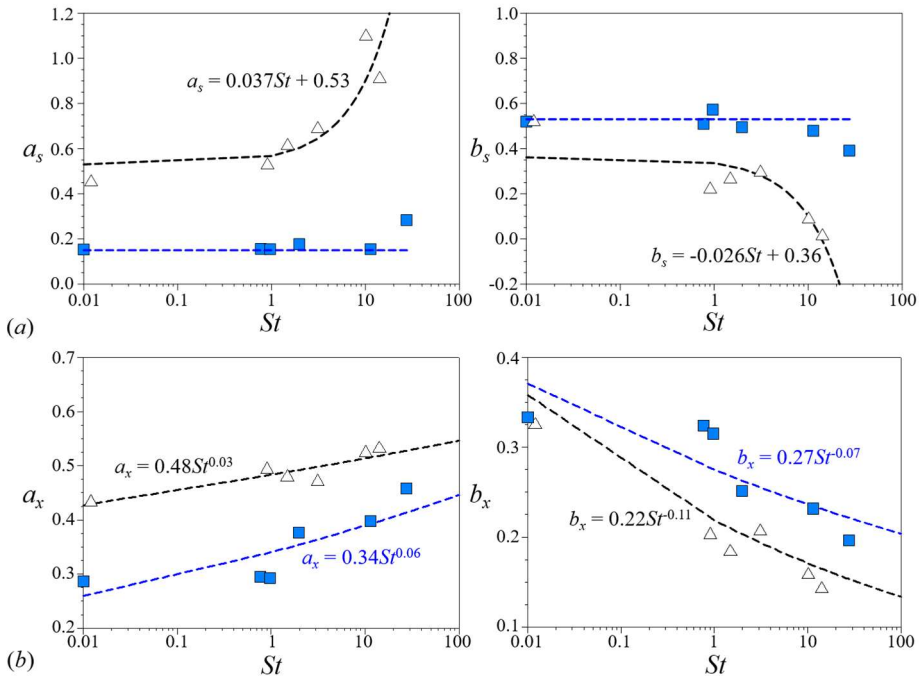

Figure 3.18. Coefficients in the empirical particle dispersion models: (*a*) a_s and b_s for σ_n model along the jet centerline (*s*-axis) on *y/D* = 0 plane; (*b*) a_x and b_x for σ_y model along *x*-axis on *x*-*y* planes. Symbols: △, *R* ~ 3.0; ■, *R* ~ 1.0.

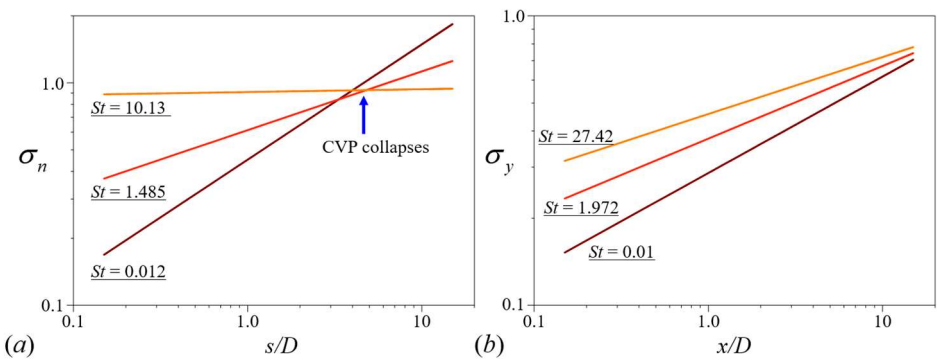

Figure 3.19. Particle concentration standard deviation by empirical particle dispersion models: (a) σ_n along the jet centerline on *y/D* = 0 plane (for *R* ~ 3.0); (b) σ_n along *x*-axis on *x*-*y* planes of *z/D* = 0 – 2.0 (for *R* ~ 1.0).

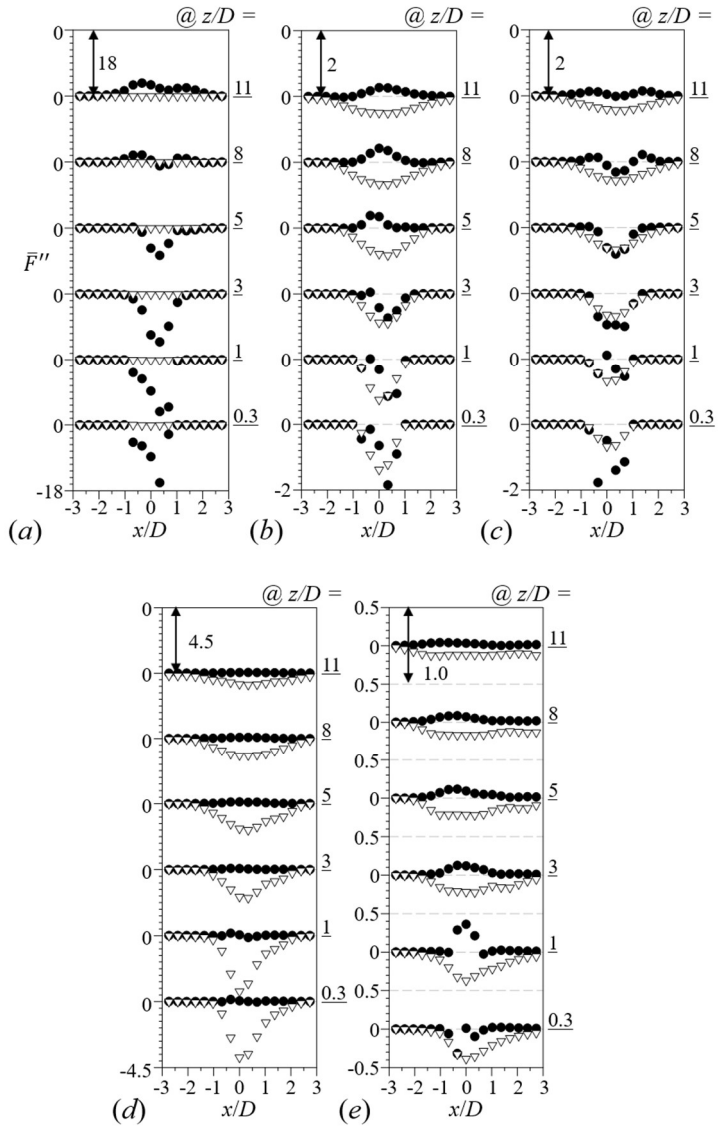

Figure 3.20. Horizontal profiles of forces ($\bar{F}''$) applied to particles along the z-direction (without crossflow): (*a*) *St* = 0.013; (*b*) 1.07; (*c*) 1.5; (*d*) 15.71; (*e*) 21.59. Symbols: ▽, gravitational body force ($\bar{F}''_G$); ●, drag force in vertical direction ($\bar{F}''_{Drag,z}$). Forces are normalized by $\rho_f \bar{u}_m^2 \bar{d}_p^2$.

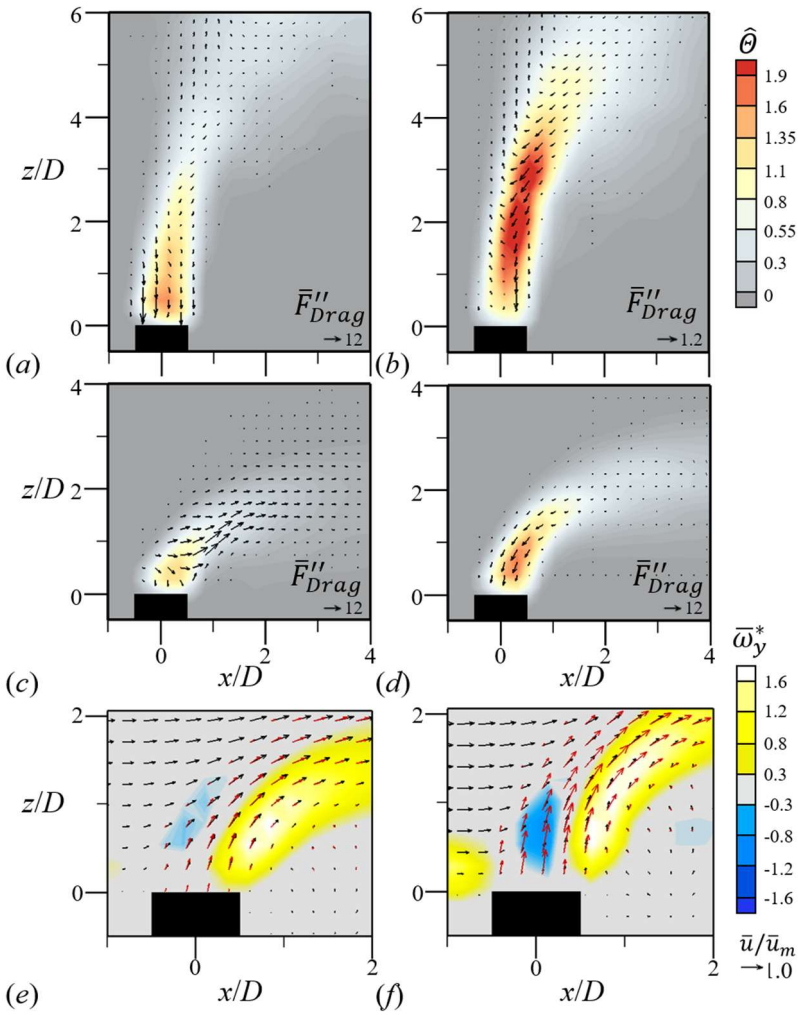

Figure 3.21. Particle concentration ($\hat{\Theta}$) contours and the drag force ($\bar{F}''_{Drag}$) vectors at the center plane ($y/D = 0$): (*a*) $St = 0.012$, $R = 3.3$; (*b*) $St = 1.485$, $R = 3.0$; (*c*) $St = 0.01$, $R = 1.0$; (*d*) $St = 0.965$, $R = 1.1$. Vorticity ($\bar{\omega}^*_y$) contours and velocity vectors (red color, solid particle; black, fluid): (*e*) $St = 0.01$, $R = 1.0$; (*f*) $St = 0.965$, $R = 1.1$.

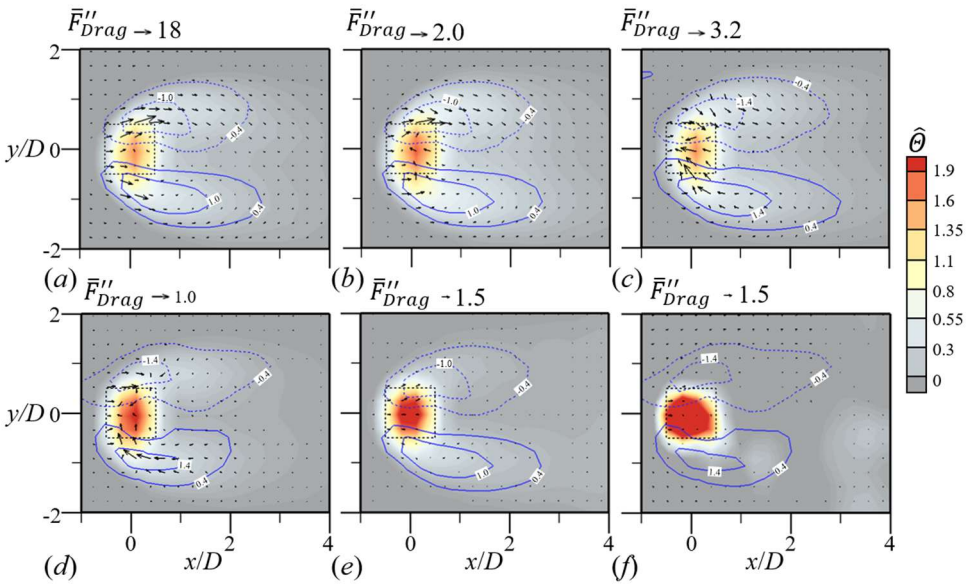

Figure 3.22. Particle concentration contours with drag force ($\bar{F}''_{Drag}$) vectors on z/D = 0.5 plane for the case of R = 1.0 – 1.2: (*a*) St = 0.01; (*b*) 0.771; (*c*) 0.965; (*d*) 1.972; (*e*) 11.33; (*f*) 27.42. In each figure lines denote iso-$\bar{\omega}_z^*$ distribution (dashed line: negative value) of airflow.

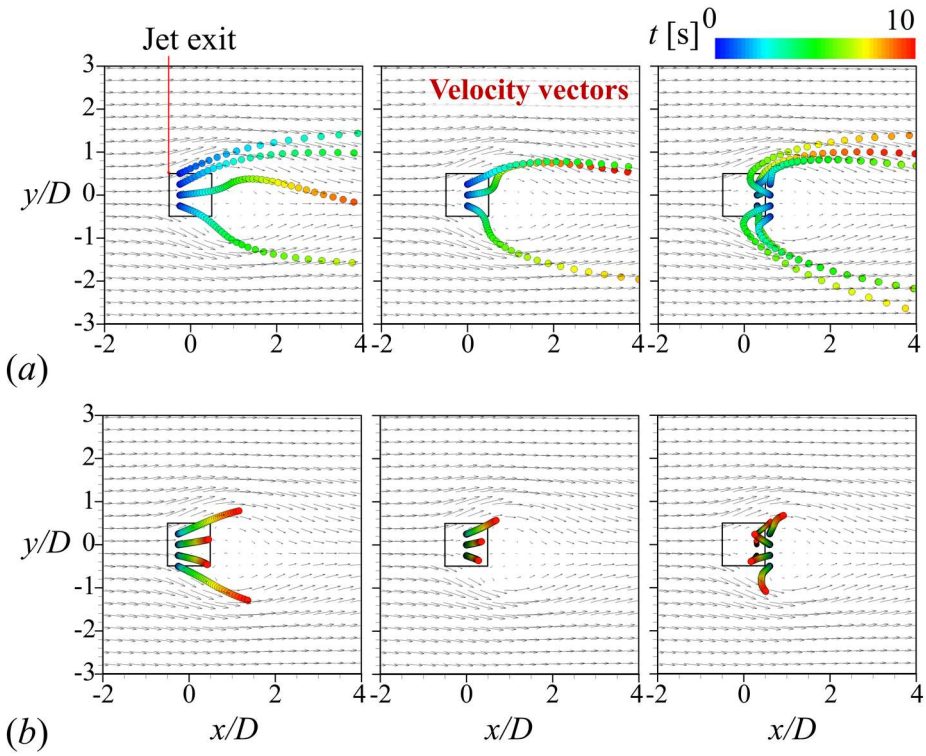

Figure 3.23. Particle trajectories and airflow velocity field at the top-view (z/D = 0.5) for $R \sim 1$: (a) St = 0.01. (b) 0.965. Circle symbols denote the particle trajectories.

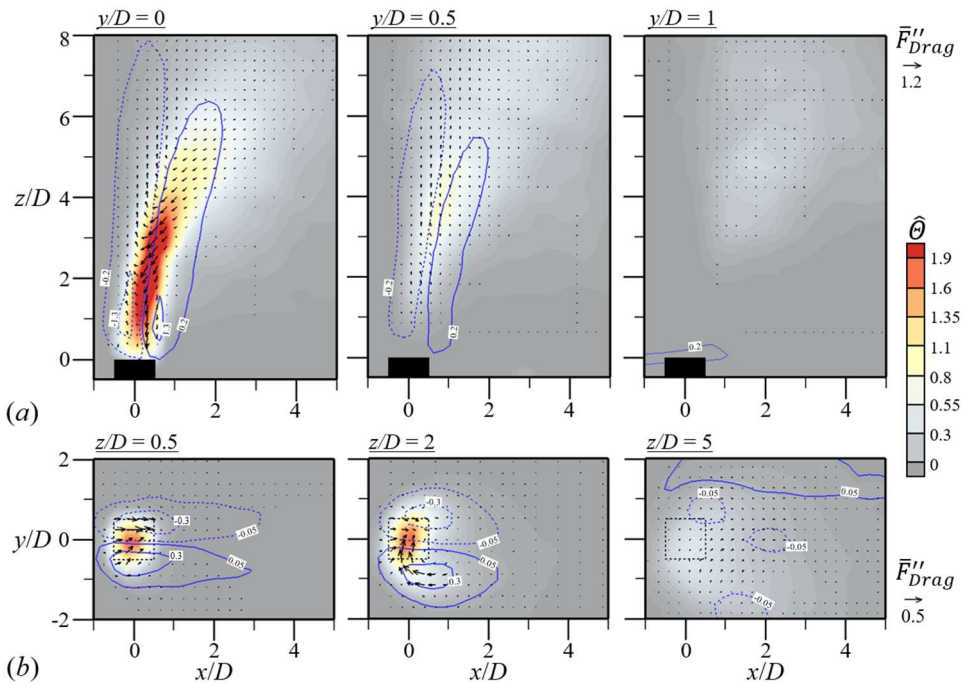

Figure 3.24. Particle concentration contours with drag force ($\bar{F}''_{Drag}$) vectors on (*a*) *x-z* planes (*y/D* = 0, 0.5 and 1.0 (*b*) *x-y* planes (*z/D* = 0.5, 2.0, 5.0) for the case of *R* = 3.0 (*St* = 1.485). In (*a, b*), lines denote the iso-$\bar{\omega}_y^*$ and $\bar{\omega}_z^*$ distributions (dashed line: negative value) of airflow, respectively.

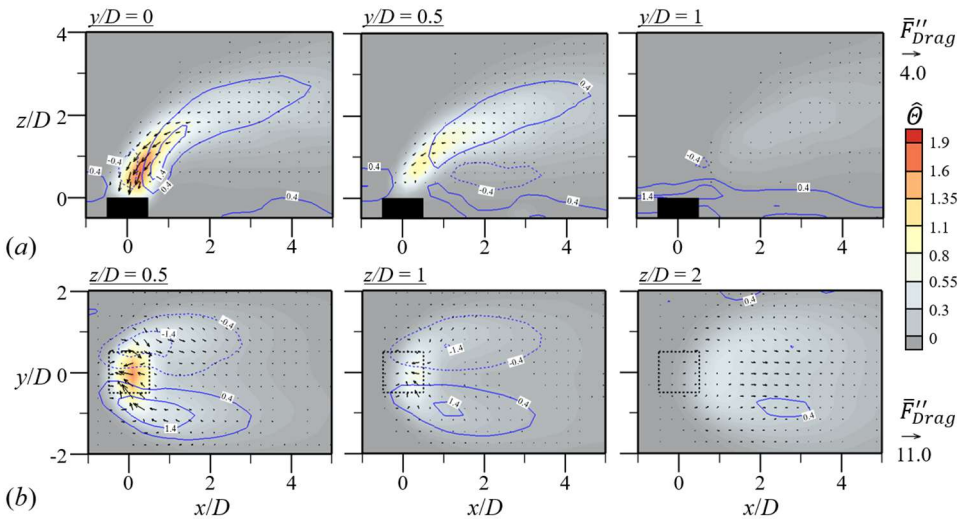

Figure 3.25. Particle concentration contours with drag force ($\bar{F}''_{Drag}$) vectors on (*a*) *x-z* planes (*y/D* = 0, 0.5 and 1.0 (*b*) *x-y* planes (*z/D* = 0.5, 1.0, 2.0) for the case of *R* = 1.1 (*St* = 0.965). In (*a, b*), lines denote the iso-$\bar{\omega}_y^*$ and $\bar{\omega}_z^*$ distributions (dashed line: negative value) of airflow, respectively.

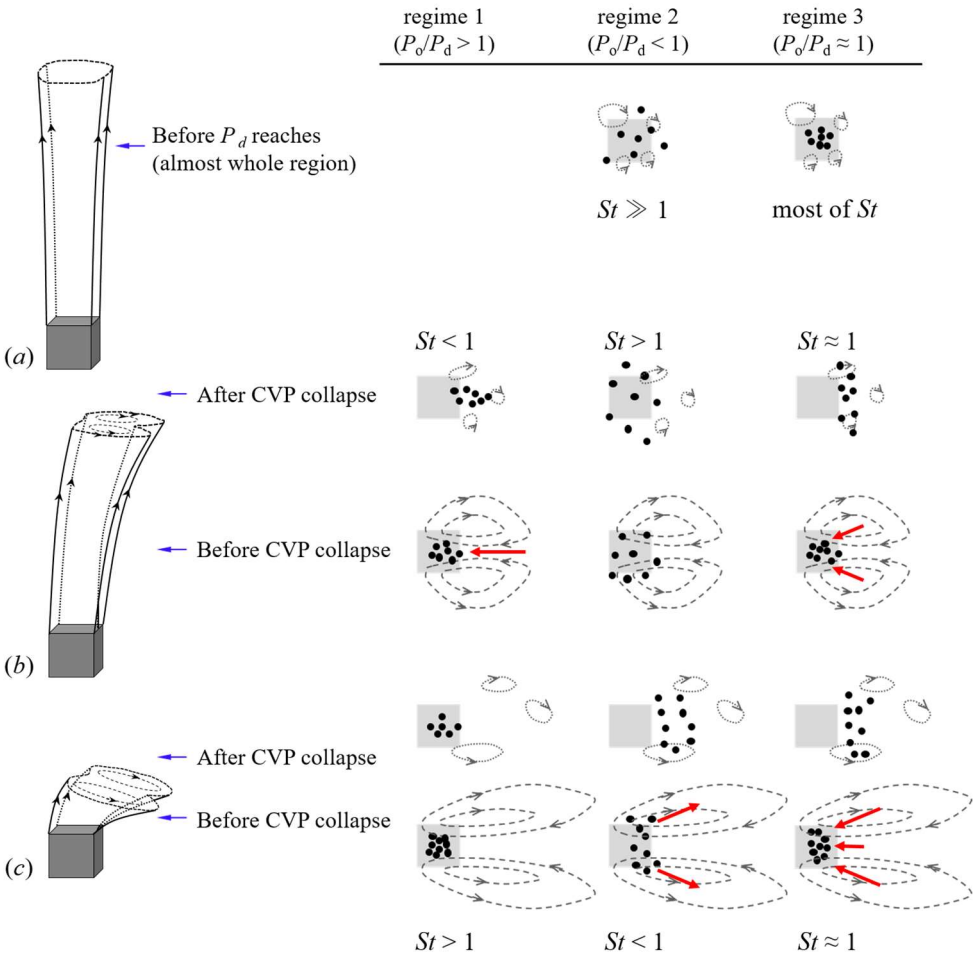

Figure 3.26. Schematics of particle dispersion (in top-view) in the vertical jet with and without crossflow (not drawn to scale): (*a*) no crossflow; (*b*) $R \sim 3.0$ (weak CVP); (c) $R \sim 1.0$ (strong CVP). The red arrows denote the direction of drag force.

Chapter 4
The particle dispersion changed by mist droplets

4.1 Variation of crossflow characteristics by droplet number

In this chapter, the behavior of hydrophilic and hydrophobic particles with a few micro-sized particles of 10 μm or less that are changed by interaction with mist droplets is analyzed based on experimental observations. Since the crossflow accompanied by mist droplets is used in the experiment to introduce the mist droplets in the wind tunnel, the variation of the physical properties of the crossflow with the droplet load should be determined first.

Figure 4.1 shows the time-averaged horizontal crossflow velocity ($\bar{u}_{cr,x}$) profiles along the z axis. Over a wide area from near the crossflow outlet to far downstream, $\bar{u}_{cr,x}$ decreases with increasing measured RH value (~ bulk droplet volume fraction) near the crossflow outlet. This reduction grows progressively larger as the profile moves downstream from the crossflow start point. For the greater RH at the crossflow outlet, an overall lower $\bar{u}_{cr,x}$ is measured for a wide range along the z-axis. From these results, we determined that the greater the amount of droplets in the crossflow, the smaller the crossflow volume flux. Since the rotational rpm of the blower fan is always constant regardless of the physical properties of the air, the mass flux in the crossflow is also assumed to be constant regardless of the droplet amount (RH value):

$$\rho_a \bar{V}_{flux,RH=30\%} = \rho_{a,50\%} \bar{V}_{flux,50\%} = \rho_{a,70\%} \bar{V}_{flux,70\%}, \qquad (4.1)$$

where ρ_a is the air density with RH 30% and room temperature and $\bar{V}_{flux}$ is the

crossflow volume flux near the fan outlet. From eq. (4.1), the air density at 30% humidity (no droplets) at the crossflow outlet and $\bar{V}_{flux}$ for the three RH cases (30%, 50% and 70%) are measurable, so that we can obtain the effective air density for the RH 50% and 70% cases (with mist droplets). $\bar{V}_{flux}$ in each RH case was calculated by integrating $\bar{u}_{cr,x}$ over the *z*-axis near the crossflow outlet; $\int \bar{u}_{cr,x}\, dz$ (see figure 4.1). RH 50%와 70%의 Estimated $\bar{V}_{flux}$ at RH 50% and 70% are 89.6% and 80% of $\bar{V}_{flux,RH=30\%}$, respectively. Therefore, the effective air density with droplets near the crossflow outlet is calculated to be higher than without droplets; $\rho_{a,50\%}$=1.367 kg/m^3 and $\rho_{a,70\%}$=1.53 kg/m^3. With this effective air density, the bulk droplet volume fraction ($\bar{\Phi}_b$) at the crossflow outlet is calculated. For instance,

$$\rho_w \bar{\Phi}_{b,RH=70\%} + \rho_a\left(1 - \bar{\Phi}_{b,RH=70\%}\right) = \rho_{a,RH=70\%} = 1.53\text{kg}/m^3, \qquad (4.2)$$

where ρ_w is the water density for room temperature. Thus, $\bar{\Phi}_b$ values for RH 50% and 70% are estimated 0.014% and 0.03%, respectively.

Before ejecting the jet flow, we first tried to measure the relative humidity field (map) inside the wind tunnel by allowing only crossflow into the wind tunnel. Figure 4.2 shows the RH profiles along the *z*-axis at various *x*-axis coordinates from the start of the crossflow to far downstream. In both $\bar{\Phi}_b$ cases (0.014% and 0.03%), the RH decreases along the *z*-axis, and the RH gradient decreases sharply from $z/D \simeq 6$. In other words, the upper part of the wind tunnel has a relatively constant RH value. Since the RH value is proportional to the mist droplet concentration, it is observed that there are relatively a few droplets uniformly distributed above the partial crossflow ($z/D \gtrsim 6$). In addition, the RH distribution along the z-axis becomes uniform as we go downstream.

4.2 Airflow characteristics change by $\bar{\Phi}_b$

4.2.1 Airflow structure

Before discussing the particle behavior depending on the particle surface condition, the significant changes of the airflow structure in terms of the time-averaged fields are explained in this chapter. Figure 4.3 shows the jet centerlines for various R and $\bar{\Phi}_b$ conditions. As discussed in Chapter 3.1, as R becomes smaller, the crossflow flux influence on the jet becomes greater, causing the jet to be sharply and quickly bent. At lower R = 1.1, the effect of $\bar{\Phi}_b$ on the jet centerline trajectory is negligible, i.e., the jet is perfectly bent in the crossflow-streamwise direction near $z/D \sim 2$, so increasing $\bar{\Phi}_b$ no longer changes the centerline trajectory. On the other hand, at a higher R = 2.85, the centerline trajectory is affected by $\bar{\Phi}_b$. As explained by Muppidi & Mahesh (2005), the jet experiences difficulty to penetrate a stronger crossflow (with higher $\bar{V}_{flux}$) even with the same R. As $\bar{\Phi}_b$ increases (as $\bar{V}_{flux}$ decreases), the more jet flow is able to penetrate the crossflow and rise further up, showing a more vertically standing (less bent) centerline trajectory. Notably, only in the $\bar{\Phi}_b$ = 0.03% case (the highest RH case) does the jet flow become less deflected in the crossflow-streamwise direction. Accordingly, it is predicted that there is a certain $\bar{\Phi}_b$ threshold value beyond which the jet centerline trajectory can change, assuming R is constant, and this threshold value is suggested to be more than 0.014% and less than 0.03%.

Figure 4.4 displays the vertical (in z-axis direction) and horizontal (in x-axis direction) jet velocity ($\bar{u}_{z,c}$ and $\bar{u}_{x,c}$, respectively) at the jet centerline trajectory. As show in figure 4.4(a), $\bar{u}_{z,c}$ does not vary with $\bar{\Phi}_b$; the jet decay constant (B) is

invariant as $\bar{\Phi}_b$ changes. On the other hand, $\bar{u}_{x,c}$ decreases in the $\bar{\Phi}_b$ = 0.03% case profile for both R = 2.85 and 1.1. For R = 2.85, the lowest $\bar{V}_{flux}$ causes the reduction of $\bar{V}_{flux}$ by the same mechanism as the less bent jet centerline trajectory with highest $\bar{\Phi}_b$. Meanwhile, the centerline position of lower R is not altered by $\bar{\Phi}_b$, but $\bar{\Phi}_b$ decreases as $\bar{\Phi}_b$ increases to 0.03%. In lower R, it is also expected that there exists a certain $\bar{\Phi}_b$ threshold value (above 0.014%) at which crossflow can affect the jet such that $\bar{u}_{x,c}$ decreases.

As explained in Chapter 3.1, when the jet meets the crossflow, a coherent vortical structure called the CVP (counter-rotating vortex pair) on the top-views (x-y planes). Figure 4.5 shows multiple top-views at z/D = 0.5, 2.5 and 5.0 with $\bar{\omega}_z^*$ contour for three $\bar{\Phi}_b$ conditions. CVPs always form at the same location whether there are mist droplets in the flow or not, and the CVPs collapse near z/D = 5 as crossflow has very little effect. The maximum $\bar{\omega}_z^*$ value at each top-view position is always the same, independent of $\bar{\Phi}_b$. However, only when $\bar{\Phi}_b$ = 0.03%, the size of the CVP becomes smaller in the z/D = 2.5 plane, where the CVP is developing. The cvp length in the x-axis is approximately 3.5D for $\bar{\Phi}_b$ = 0 and 0.014%, but it is reduced to approximately 3D for $\bar{\Phi}_b$ = 0.03%. This phenomenon is associated with a less deflected jet centerline, i.e., it is affected by crossflow entrainment, which contributes to CVP formation (detailed explanation in Chapter 4.2.2). For the lower R flow, we have also analyzed the $\bar{\omega}_z^*$ observed at various top-view planes (z/D = 0.5, 1.5 and 2.5) (figure 4.6). As shown in figure 4.3, the CVP is already collapsed in the z/D = 2.5 plane, as the jet is completely deflected in the crossflow direction within the range of $1 < z/D < 2$. In addition, since the CVP is part of the 'hairpin vortex' located just above the jet exit, which is generated by the perfect bending of the jet (Mahesh 2013), the magnitude of the CVP is not affected by $\bar{\Phi}_b$ at all, unlike the higher R case.

4.2.2 Airflow entrainment into the jet

To understand how the airflow vortical structure changes with the mist droplet volume fraction (RH of the flow), we analyzed the crossflow entrainment into the jet flow. Prior to the analysis, we first defined the jet boundary (figure 4.7a). The location of the jet boundary was determined based on the concentration field of PTFE particles, which is not affected by humidity or contact with droplets. Since previous studies based on computational fluid dynamics (CFD) estimated the jet boundary using the scalar distribution by diffusion equation, the jet boundary was defined as the location of 1% of the local scalar max concentration (along the jet centerline; *s/D*). However, since this study uses solid particles based on experiments, the definition of jet boundary location in previous studies is not suitable. Therefore, we defined a new jet boundary threshold based on the concentration field of solid particle concentration with $St \ll 1$. The jet is located where the concentration is more than 10% of the maximum concentration value in the entire particle concentration field (yellow area shown in figure 4.7a). This threshold value was also validated based on the airflow velocity field and found to be suitable as a jet boundary. For two-dimensional observation by PIV, based on the airflow velocity field inside the jet boundary, the local jet flux along the jet centerline (*s*-axis) is defined as follows:

$$Q = \int_{N_j} \bar{u}(s,n)\, dn, \tag{4.3}$$

where $\bar{u}$ is the jet flow velocity magnitude defined as $\sqrt{\bar{u}_z^2 + \bar{u}_x^2}$. Figure 4.7(b) shows the local Q evolution along the s-axis calculated using equation (4.3). For R = 2.85, low Q values are measured only in the case of $\bar{\Phi}_b$ = 0.03%, in line with the

results of the jet centerline and CVP size analysis. In particular, Q appears to decrease downstream of $s/D > 8$; Negative $\mathrm{d}Q\ /\ \mathrm{ds}$ is measured downstream where $s/D > 8$ for $R = 2.85$ (figure 4.8). At $s/D = 14$, the flow entrained inside the jet is again discharged to the outside and the Q value becomes similar to the initial Q value near the jet exit. Similarly, in the $\overline{\Phi}_b = 0$ and 0.014% cases, the Q value hardly increases (but does not decrease) downstream where the crossflow contribution becomes smaller. Even upstream of $s/D \leq 8$, the growth rate of Q of $\overline{\Phi}_b = 0.03\%$ is much smaller. The CVP in the higher R case is developed by the entrained flow introduced by the jet 'tilting and folding' progress (Kelso *et al*. 1996; Cortelezzi & Karagozian 2001). Therefore, heavier crossflows can be entrained relatively less into the jet and cause a decrease in CVP size. Thus, CVP strength (Ψ) based on the top-view observation which is defined as

$$\Psi = \int_A |\overline{\omega}_z^*|\, dA, \tag{4.4}$$

where A is the CVP cross-section area (CVP boudnary determined by 5% of the maximum vorticity in each top-view plane) also slightly decreases accroding to the $\overline{\Phi}_b$ growth (figure 4.9). This reduction is consistently observed at all locations where CVP develops (both of $z/D = 0$ and 2.5).

As shown in figure 4.7(b), Q is not affected by the change in $\overline{\Phi}_b$ for $R = 1.1$. Similarly, the value of $\mathrm{d}Q\ /\ \mathrm{ds}$, which estimates the entrainment flux into the jet, does not change with increasing $\overline{\Phi}_b$ (figure 4.8). Regardless of the value of $\overline{\Phi}_b$, Q increases upstream and then slowly decreases downstream after $s/D \simeq 10$. In the perfect jet bending region, where CVP exists ($s/D \lesssim 4$), $\mathrm{d}Q\ /\ \mathrm{ds}$ increases rapidly due to strong mixing and then decreases after mixing is complete. Moreover, similar to the size of the CVP which is independent of the variation of $\overline{\Phi}_b$, no change in Ψ is observed (figure 4.9).

4.3 Particle dispersion patterns

4.3.1 Particle concentration maxima line

This chapter describes the characteristics of particle behavior dispersed by the airflow structure previously analyzed. Figure 4.10 shows the trajectories of the particle concentration maxima lines for various R and $\overline{\Phi}_b$ cases. The particle concentration maxima line is defined as a line connecting the locations where the local maximum concentration is measured along the jet centerline trajectory (s-axis). The method for finding the local maximum concentration is the same as for finding the wake trajectory illustrated in figure 3.5(a). First, plot the concentration profile along the n-axis perpendicular to the s-axis at the local s coordinate. Find the location in that profile where the concentration peak value appears, and that is the local maximum concentration location at that particular s coordinate. As shown in figure 4.10, at lower R = 1.1, the location of the concentration maxima line is always constant regardless of the variation of $\overline{\Phi}_b$, as is the jet centerline. These concentration maxima lines are very close to the jet centerline. No trajectory differences are found between hydrophilic and hydrophobic particles. Similarly, at higher R = 2.85, the trajectories of the concentration maxima line and the jet centerline are very similar to each other in most cases. However, a slight variation is observed in the concentration maxima line trajectory of the silicon particle when $\overline{\Phi}_b$ = 0.014%. This is caused by a moderate number of droplets being ejected and causing some instability within the jet flow, but this trajectory variation is not significant as it does not affect the particle dispersion pattern (more detailed dispersion patterns are discussed in Chapter 4.3.2).

Next, we analyzed the particle concentration ($\hat{\Theta}_m$) decay at the particle concentration maxima lines (figure 4.11). The coordinates of the particle concentration maxima line are defined as (s_p, n_p); s_p is corresponds to concentration maxima line length from the jet exit and n_p is the coordinate in the axis which is perpendicular to the concentration maxima line (figure 4.12a). For higher R (= 2.85), despite the slight variation of the concentration maxima line observed, the $\hat{\Theta}_m$ decay rate for both Si and PTFE particles is always constant regardless of the variation of $\bar{\Phi}_b$ (figure 4.11a). Although the jet centerline trajectory changed in the $\bar{\Phi}_b = 0.03\%$ condition, this did not affect the $\hat{\Theta}_m$ evolution. In other words, both hydrophilic and hydrophobic particles have little interaction with the mist droplets accompanying the airflow within the jet with high R. The jet centerline trajectory changed for the $\bar{\Phi}_b = 0.03\%$ condition. On the other hand, for lower R (= 1.1), the hydrophilic si particle showed a comparatively small $\hat{\Theta}_m$ decay rate at the highest $\bar{\Phi}_b$ condition. This means that hydrophilic particles are more likely to interact with mist droplets as R decreases, resulting in a greater amount of particle dispersion farther downstream of the jet. The concentration discrepancy between the $\bar{\Phi}_b = 0.03\%$ condition and the other lower $\bar{\Phi}_b$ value cases increases at $s/D > 5$. This is the region where the jet bending is completely finished and the crossflow and jet flow are completely mixed without any coherent vortical structure. Despite the increased contact probability between particles and droplets due to strong mixing, the $\hat{\Theta}_m$ decay rate of hydrophobic particles is constant for all $\bar{\Phi}_b$ conditions; hydrophobic particles are not affected by mist droplets.

4.3.2 Particle concentration variation by $\bar{\Phi}_b$

To analyze the spatial particle distribution in the region beyond the centerline maxima line, we compared the concentration profiles along the np axis at several s_p coordinates for three different $\bar{\Phi}_b$ conditions (figure 4.12b & 4.13); this comparison is based on the side-view at jet center-plane (y/D = 0). As observed in figure 4.11, the spatial particle distribution along the s_p and n_p axes for both Si and PTFE particles is not affected by the change in $\bar{\Phi}_b$ (figure 4.12b).

On the other hand, over a wide np-axis range (n_p > -6), silicon particle concentration increases jet downstream with the highest $\bar{\Phi}_b$ for low R (figure 4.13a). At s_p/D = 2 (where mixing in progress with CVP generation), particle dispersion in the jet center-plane is not affected by $\bar{\Phi}_b$. At s_p/D = 5, the concentration of $\bar{\Phi}_b = 0.03\%$ increases in the upper part (n_p < 0) of the concentration maxima line; many particles are concentrated at this location. In the farther region (s_p/D > 5), the concentration of particles with $\bar{\Phi}_b = 0.03\%$ condition increases within the overall jet center-plane (at y/D = 0). To observe the particle dispersion characteristics not only in the jet centerplane (side-view at y/D = 0) but also in the transverse direction (y-axis), we calculated the concentration discrepancy ($\Delta\hat{\theta}$) between the conditions of $\bar{\Phi}_b = 0.03\%$ and $\bar{\Phi}_b = 0\%$ for multiple top-views and jet center-plane (figure 4.14). In the contour of figure 4.14, the blue color indicates the region where the concentration decreases with increasing $\bar{\Phi}_b$, and the red color indicates the opposite. In the high RH & droplet volume fraction region shown in the side view, the particles are not dispersed much under the high $\bar{\Phi}_b$ condition (figure 4.14a); on the other hand, the without mist droplets particles were frequently dispersed in this location as well. This phenomenon is verified in the top-view (figure 4.14b). At z/D = 0.5 (near the jet exit), the leeside region of the jet center is entirely a high humidity region, and the $\Delta\hat{\theta}$ of silicon particles in this region becomes negative. Eventually, as $\bar{\Phi}_b$ increases, the silicon particles disperse slightly on the windward side of the

jet center or rise upward along the jet centerline. Then, they concentrate in a certain area in the *z/D* = 1.5 plane, where the jet deflection is ongoing, or continue to rise upward. It shows a preferential concentration in the high humidity gradient region on the windward side of the jet center and does not disperse to the high humidity zone along the *y*-axis. The leeside high RH region of the jet center, still represented by the blue color, also has a relatively low particle concentration. After the jet is completely deflected (*z/D* = 2.5), the Si particles that are preferentially concentrated at the jet center-plane (*y/D* = 0) by the mist droplet disperse downstream of the jet with less transportation out of the jet center-plane. In other words, under the high $\bar{\Phi}_b$ condition, the hydrophilic Si particles avoid dispersion in the transverse direction inside the CVP and tend to travel along the jet centerline within the jet center-plane.

No obvious spatial (along the n_p axis) concentration profile variation is observed for the hydrophobic PTFE particles under different $\bar{\Phi}_b$ conditions (figure 4.13b). The $\Delta\hat{\theta}$ between the conditions of $\bar{\Phi}_b = 0.03\%$ and $\bar{\Phi}_b = 0\%$ was also measured to be smaller for hydrophobic particles than for hydrophilic particles (figure 4.15). In the top-views where CVP is visible (*z/D* = 0.5 and 1.5), a relatively small magnitude of $\Delta\hat{\theta}$ is produced in the high RH region where is leeside of the jet center. In other words, hydrophobic particles are well dispersed even where the mist droplet population is high. At *z/D* = 1.5 plane, like silicon particles, PTFE particles preferentially concentrate in the high humidity gradient region, but eventually these particles disperse into the high humidity region along the transverse direction (*y*-axis). Therefore, a C-shaped pattern of $\Delta\hat{\theta}$ is observed in this plane. Since these particles behave inside the CVP and are highly dispersed in the transverse direction, the hydrophobic particles' $\Delta\hat{\theta}$ magnitude downstream of the jet after the CVP has completely disappeared (after the jet deflection is completed) is quite

negligible.

4.4 Force analysis for understanding the particle dispersion mechanism

4.4.1 Drag force for particle dispersion

To elucidate the mechanism by which the dispersive properties of Si particles with increasing $\bar{\Phi}_b$ that we have observed so far occur, we estimate the dominant forces on the particles. As discussed in Chapter 3.3, when performing a scale analysis considering solid particles with $St \ll 1$ in air, all terms except the drag force are neglected among the various forces that can be acting on the particles by the background given by Maxey & Riley (1983). Saffman lift force and Magnus lift force are also excluded without exception. Therefore, the most important force term in this chapter is the drag force. In addition, if a solid particle and a mist droplet are in contact, the drag force equation (3.2) may introduce a relative velocity variation. This relative velocity change can lead to an alternation of the drag force.

Figure 4.16 shows the Si particle concentration & RH distribution and also drag force ($\bar{F}''_{Drag}$) vector under $\bar{\Phi}_b = 0.03\%$ condition. Comparing the side-view and the top-views (figure 4.16b), the vertical component of the drag force is much greater than the transverse component in the high humidity region.This implies that the most Si particles within the jet are moving vertically. Furthermore, particles cannot contact the mist droplets because the jet has little entrained crossflow. After the CVP breaks up, $\bar{F}''_{Drag}$ on the particle in both directions become comparable. However, it is difficult for the particle surface conditions to change because the influence of

crossflow is negligible and the humidity is low. The observed features, such as the direction and magnitude of the drag force, are always constant under all $\bar{\Phi}_b$ conditions, regardless of the particle surface condition (both of Si and PTFE particles).

On the other hand, the variation of Si particle drag force by $\bar{\Phi}_b$ is observed in the top-view for lower R = 1.1, z/D = 0 (figure 4.17a). When there are no mist droplets in the airflow ($\bar{\Phi}_b = 0\%$), $\bar{F}''_{Drag}$ on the Si particles is in the crossflow-streamwise direction; the Si particles are dragged toward the outside of the CVP. However, it is noteworthy that the direction of $\bar{F}''_{Drag}$ is reversed within the CVP. That is, $\bar{F}''_{Drag}$ direction becomes similar to the vortex rotation direction. As a result, the Si particles are dragged towards the jet center. The reason for this drag direction reversal is considered to be the contact between the Si particle and mist droplet. It is analyzed that this contact changes the surface conditions of the hydrophilic Si particles, resulting in different dispersion characteristics of the particles. Chen *et al*. (2018) experimentally observed that when a hydrophilic surface is in contact with high humidity air, a liquid-like layer of several nanometers is formed on the surface. Considering the results of these previous studies, we believe that the surface conditions of the Si particles would have changed sufficiently under the condition of $\bar{\Phi}_b = 0.03\%$. As shown in figure 4.17(b), the drag force on the PTFE without mist droplet ($\bar{\Phi}_b = 0\%$) is also directed in the crossflow-streamwise direction in all regions, just like the Si particle. As $\bar{\Phi}_b$ increases to 0.03%, the drag force direction still does not change.

4.4.2 Increased particle body force by contact with droplets

We performed a 2D simulation using a commercial CFD tool (ANSYS FLUENT 2023 R1) to determine the mass of water deposited on a silicon particle when a particle disperses in a mist droplet-laden flow and contacts a droplet (figure 4.18). The simulation was performed for both hydrophilic and hydrophobic particles. The position of the particle was fixed within the simulation geometry and a droplet-laden airflow with a certain flow velocity was implemented around it. In other words, the flow is equivalent to a humid droplet-laden airflow around a cylinder (the circle assumed to be the particle). The flow geometry is a rectangle of size 2000 μm (streamwise) x 1000 μm (spanwise) with a solid particle at its center. The floor and ceiling walls of the rectangular geometry are set to symmetry. The left wall is the velocity-inlet and the right wall is the pressure-outlet. The size ($\bar{d}_p$) of both hydrophilic and hydrophobic particles is set to 6 μm. In the case of hydrophilic particles, the shear stress was fixed to 0, assuming that the surface condition had already changed to a slip condition due to the initial droplet contact. On the other hand, the surface of hydrophobic particles is in a non-slip condition. In order to accurately analyze the flow around the particles, we created a 14 inflation mesh layers of rectangular mesh cells near the particle surface. The first layer thickness of the inflation is 0.2 μm and the growth rate is 1.2. The flow was assumed to be laminar considering that $Re_p < 1$ (see table 2.2). The velocity at the inlet was uniformly set to 0.1 m/s because the experimentally measured relative velocity (u - v) is $\boldsymbol{O}(0.1)$. To simulate the micro-sized droplet-laden flow, the multiphase model used the Eulerian model, which produces in-homogeneously dispersed droplets. Together with this model, evaporation and condensation of 10 μm droplets were considered. The water droplet volume fraction at the inlet was set to 0.03%, the same as the highest $\bar{\Phi}_b$ condition in the experiment. We obtained the steady solution for the airflow with moisture considering gravity. As shown in figure 4.18(a), a high $\bar{\Phi}$

was observed around the hydrophilic (Si) particles, indicating a certain amount of water deposited on the particle surface. However, no water is deposited around the PTFE particles. To calculate the mass of water deposited on the surface of the Si particle, the value of droplet (water) volume fraction ($\bar{\Phi}$) × water density (1000 kg/m^3) was integrated over a radius $3\bar{d}_p$ area around the particle. As a result, the mass of water is calculated to be only 1.03% of the single particle mass. In other words, under the conditions of this study, the effect of increasing the particle mass due to the contact between the droplet and the particle is negligible. In order to increase the particle mass due to the droplet contact and cause it to settle, it would be necessary to increase the atomized droplet number much more significantly, thereby greatly increasing the contact probability.

4.4.3 An experimental observation of contact between particles and mist droplets

Under the condition $\bar{\Phi}_b$ = 0.03%, we expected that the si particle surface condition would have changed with liquid-like layer. Thus, this surface condition change was believed to contribute to the directional reversal of the drag force exerted on the Si particles occurring within the CVP. We carried out a simple additional experiment to validate the hypothesis that hydrophilic particles can absorb and capture mist droplets, shown in figure 4.19(a), which was performed in a wind tunnel with RH = 70%. Samples of PTFE and Si particles were prepared for testing, which consisted of applying a strong adhesive (3M tape) to a slide glass and applying an even layer of each particle type on top (figure 4.19b). The sample was placed at the center of the crossflow exit and at the jet exit (z/D = 1.5, x/D = y/D = 0). Since we

are interested in measuring the intensity of the light reflected by the particles, we made the laser sheet as thick as the width of the particle sample (slide glass) and pointed the laser sheet perpendicular to the sample. The mist droplet-laden crossflow was blown for 1 minute to expose the particles in the sample to the mist-droplet. The intensity of the light reflected from the sample before crossflow blowing was then compared to the intensity of the light one minute later (after crossflow blowing) (figure 4.19b). Checking the raw images, the intensity of the light reflected from the PTFE particles remained almost unchanged, but the intensity of the light reflected from the Si particles decreased slightly after crossflow blowing. To quantitatively evaluate the light reduction, the spatially averaged light intensity reduction rate within the sample area was calculated (figure 4.19c); the spatially averaged light intensity value was defined as (sum of light intensity in each pixel/the number of pixels) within the sample area. PTFE showed a reduction rate of about 2%, while Si showed a light intensity reduction of more than 10%. This decrease in light intensity is believed to be due to the refraction of light in a droplet, which results in a significantly smaller amount of light reflection than in a solid particle. Therefore, more mist droplets were deposited and captured on the Si particles. The amount of these droplets appears to be sufficient to change the relative velocity direction between the particles and the airflow.

4.4.4 Summary of particle dispersion mechanisms

Our observations on the particle dispersion alternation by water droplet is graphically summarized in figure 4.20. Without no mist distribution, Si and PTFE particle both tend to disperse uniformly outside the vortex boundary both before and

after CVP collapse. PTFE retains this dispersion pattern despite increasing $\overline{\Phi}_b$. However, silicon particles are preferentially concentrated in the jet center and in the high humidity gradient region. Notably, the particles in the high humidity region hardly disperse along the transverse (y) direction where the humidity (and $\overline{\Phi}$) is high. In other words, under high $\overline{\Phi}_b$ conditions, they gather in the jet center-plane (y/D = 0) and remain in the same position after the CVP collapses. Therefore, under these conditions, Si particles are dispersed far downstream along the jet centerline, and high Si particle concentrations can be observed even at locations far from the particle source, as shown in figure 4.11(b). In summary, mist droplets in the airflow cause hydrophilic particles to remain mostly within the jet center and do not allow them to disperse outside the CVP.

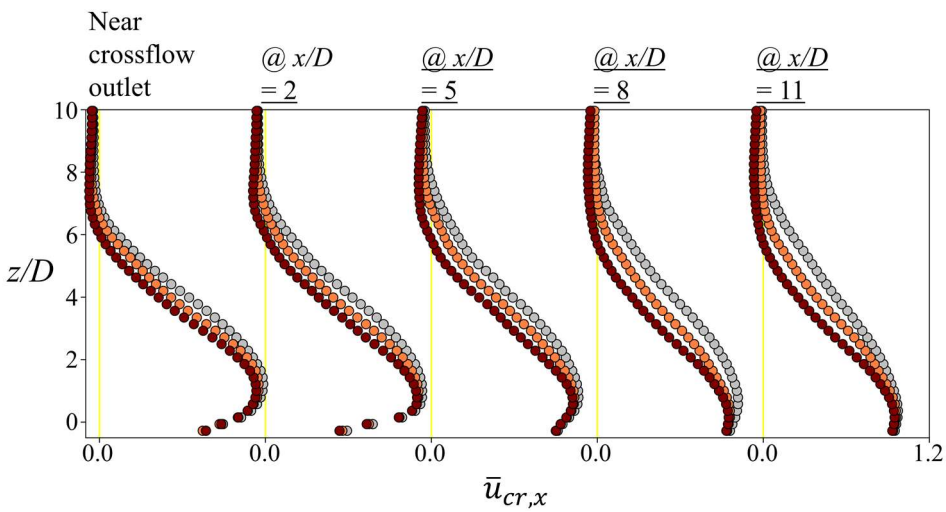

Figure 4.1. The time-averaged horizontal crossflow velocity ($\bar{u}_{cr,x}$) profiles along the *z* direction at several *x* coordinates (*x/D* = -13, 2, 5, 8 and 11). ●, $\bar{\Phi}_b = 0\%$ (RH = 30%); ●, $\bar{\Phi}_b = 0.014\%$ (RH = 50%); ●, $\bar{\Phi}_b = 0.03\%$ (RH = 70%).

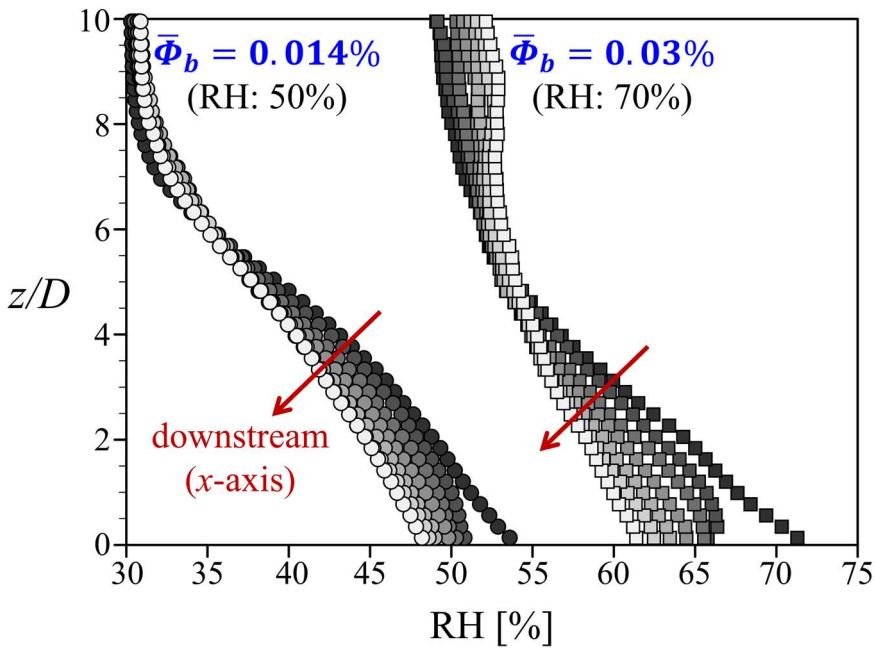

Figure 4.2. RH profiles along the z-axis at various x coordinates from the start of the crossflow to far downstream for two cases: $\bar{\Phi}_b = 0.014\%$ (RH = 50%) & $\bar{\Phi}_b = 0.03\%$ (RH = 70%). The colors of symbols denote the coordinates on the x-axis.

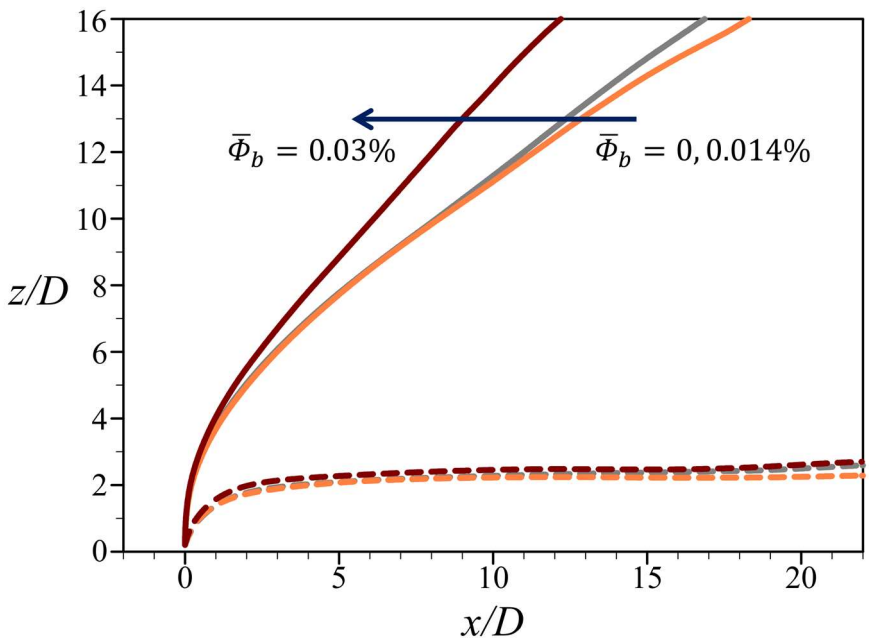

Figure 4.3. Jet centerline trajectories for various R and $\bar{\Phi}_b$ conditions. Gray lines, $\bar{\Phi}_b = 0\%$ (RH = 30%); orange, $\bar{\Phi}_b = 0.014\%$ (RH = 50%); dark red, $\bar{\Phi}_b = 0.03\%$ (RH = 70%).

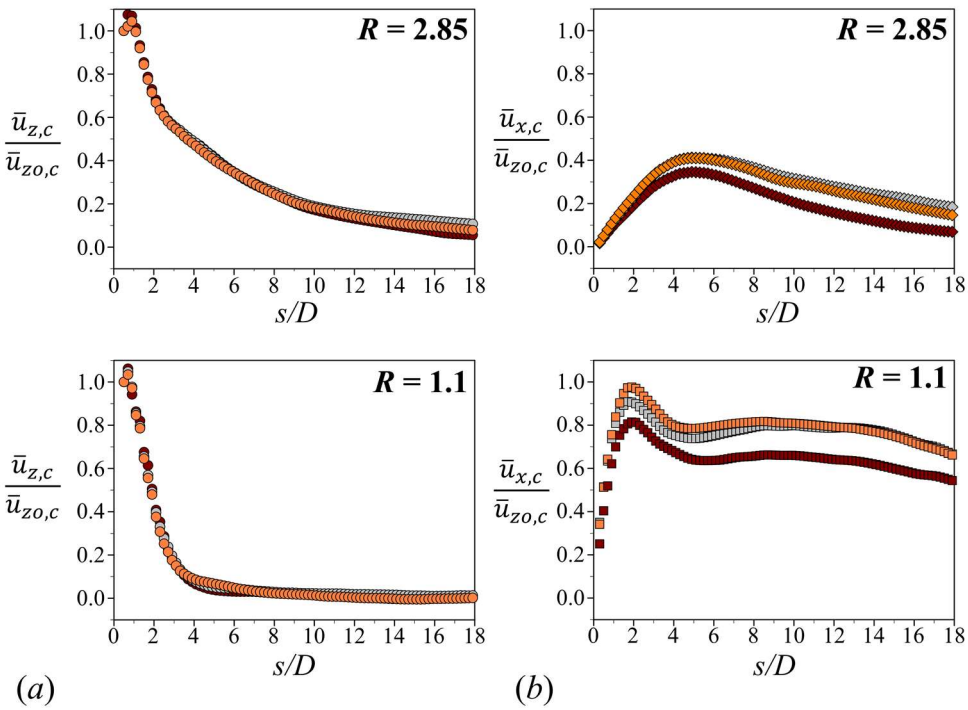

Figure 4.4. The time-averaged vertical (in z-axis direction) and horizontal (in x-axis direction) jet velocity ($\bar{u}_{z,c}$ and $\bar{u}_{x,c}$, respectively) at the jet centerline trajectory: (*a*) $\bar{u}_{z,c}$: ●, $\bar{\Phi}_b = 0\%$ (RH = 30%); ●, $\bar{\Phi}_b = 0.014\%$ (RH = 50%); ●, $\bar{\Phi}_b = 0.03\%$ (RH = 70%). (*b*) $\bar{u}_{x,c}$: ■, $\bar{\Phi}_b = 0\%$ (RH = 30%); ■, $\bar{\Phi}_b = 0.014\%$ (RH = 50%); ■, $\bar{\Phi}_b = 0.03\%$ (RH = 70%).

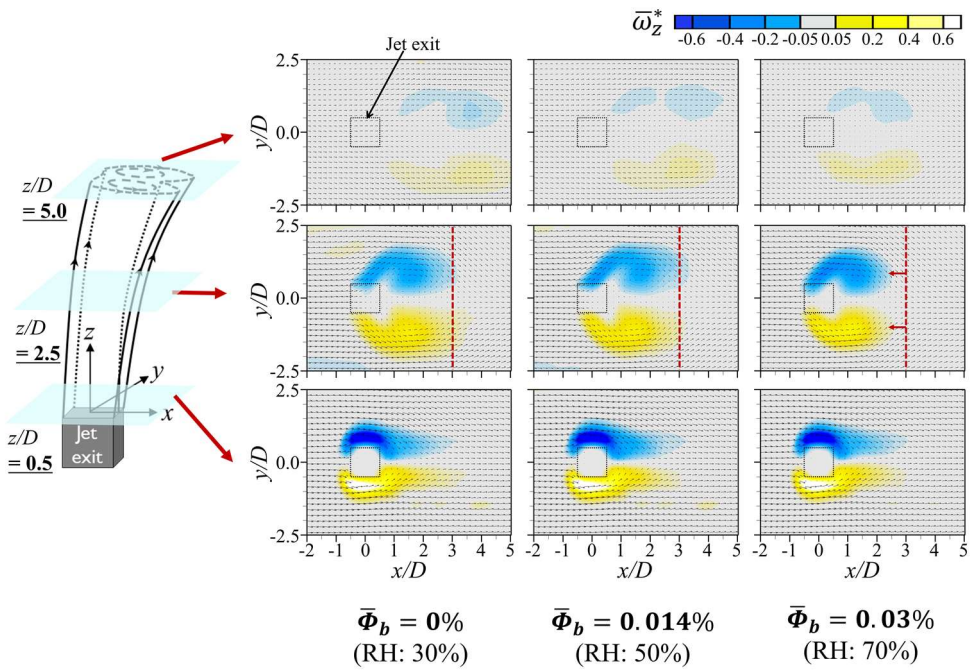

Figure 4.5. Vorticity ($\bar{\omega}_z^* = \bar{\omega}_z D/\bar{u}_m$) contours and velocity vectors in the time-averaged air jet flow with crossflow (R = 2.85) under three $\bar{\Phi}_b$ conditions (0%, 0.014% and 0.03%) on multiple x-y planes at z/D = 0, 2.5 and 5.0.

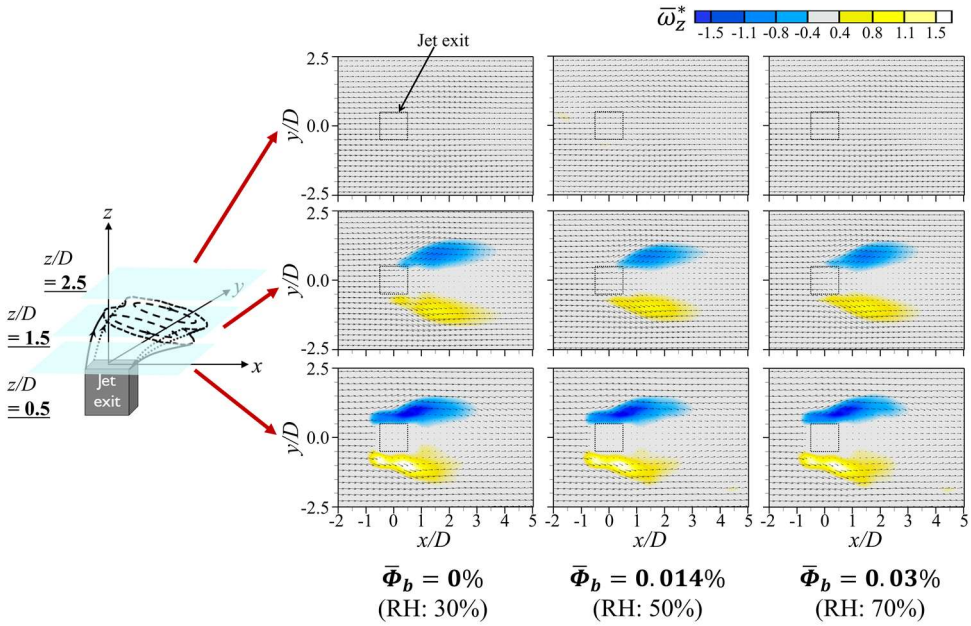

Figure 4.6. Vorticity ($\overline{\omega}_z^* = \overline{\omega}_z D/\overline{u}_m$) contours and velocity vectors in the time-averaged air jet flow with crossflow (R = 1.1) under three $\overline{\Phi}_b$ conditions (0%, 0.014% and 0.03%) on multiple x-y planes at z/D = 0, 1.5 and 2.5.

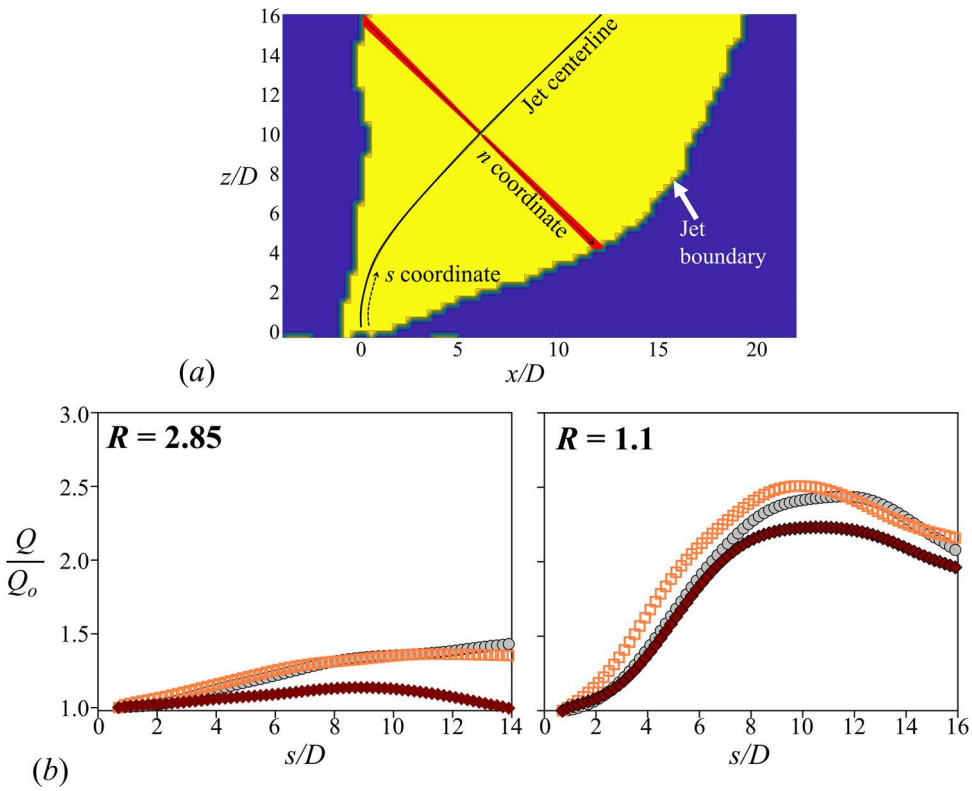

Figure 4.7. (*a*) Jet boundary illustration. (*b, c*) Local jet flux (Q) normalized by initial flux (Q_o) evolution along the s-axis (jet centerline) for R = 2.85 and 1.1. In (*b, c*), ●, $\bar{\Phi}_b = 0\%$ (RH = 30%); □, $\bar{\Phi}_b = 0.014\%$ (RH = 50%); ♦, $\bar{\Phi}_b = 0.03\%$ (RH = 70%).

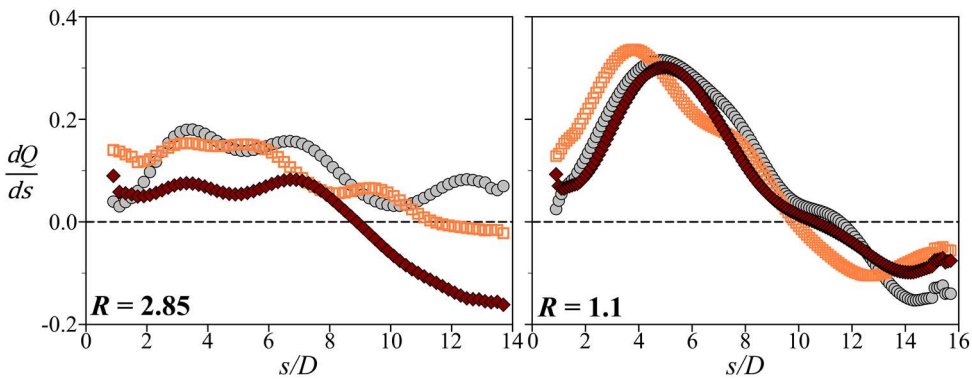

Figure 4.8. dQ/ds profiles along the jet centerline (s-axis) for R = 2.85 and 1.1. ●, $\bar{\Phi}_b = 0\%$ (RH = 30%); □, $\bar{\Phi}_b = 0.014\%$ (RH = 50%); ♦, $\bar{\Phi}_b = 0.03\%$ (RH = 70%).

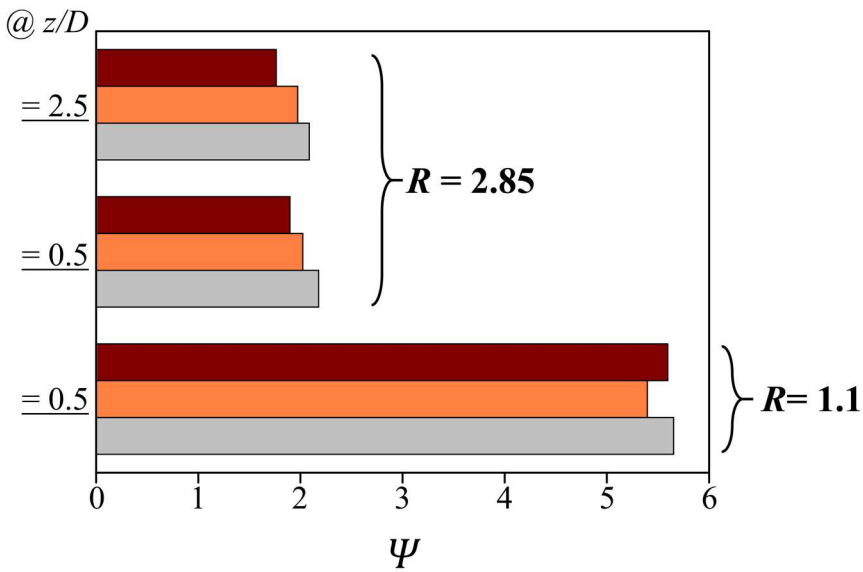

Figure 4.9. A bar graph of the CVP strength (Ψ) calculated on the top-views at *z/D* = 0.5 and 2.5 for *R* = 2.85 and 1.1. Light gray, $\bar{\Phi}_b = 0\%$ (RH = 30%); orange, $\bar{\Phi}_b = 0.014\%$ (RH = 50%); $\bar{\Phi}_b = 0.03\%$ (RH = 70%);

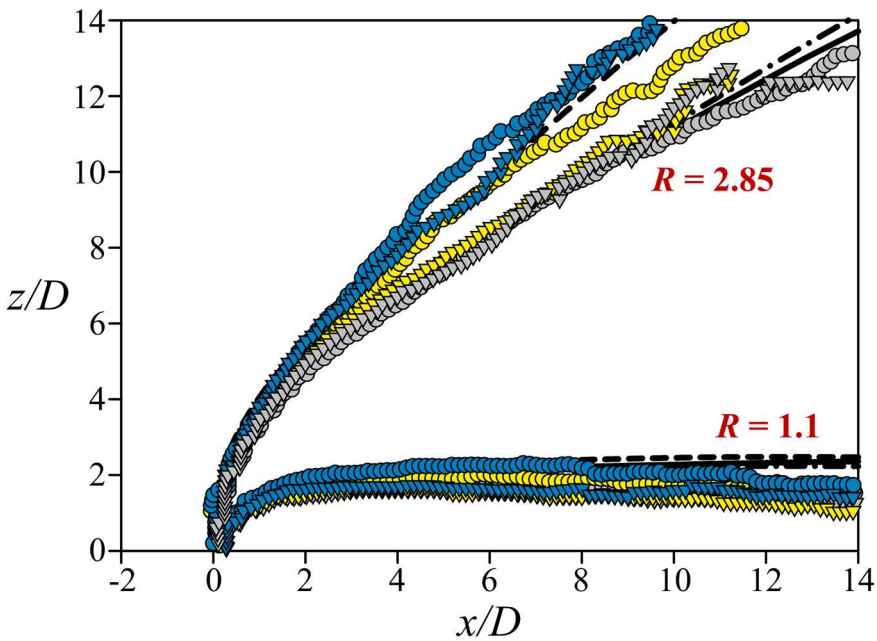

Figure 4.10. The trajectories of the particle concentration maxima line (symbols) and jet centerline (lines). For particle concentration maxima lines, Si particle: ●, $\bar{\Phi}_b = 0\%$ (RH = 30%); ● (yellow), $\bar{\Phi}_b = 0.014\%$ (RH = 50%); ●, $\bar{\Phi}_b = 0.03\%$ (RH = 70%) & PTFE particle: ▼, $\bar{\Phi}_b = 0\%$ (RH = 30%); ▼ (yellow), $\bar{\Phi}_b = 0.014\%$ (RH = 50%); ▼, $\bar{\Phi}_b = 0.03\%$ (RH = 70%). For jet centerlines, solid line, $\bar{\Phi}_b = 0\%$ (RH = 30%); dash-dot line, $\bar{\Phi}_b = 0.014\%$ (RH = 50%); short dashed line, $\bar{\Phi}_b = 0.03\%$ (RH = 70%).

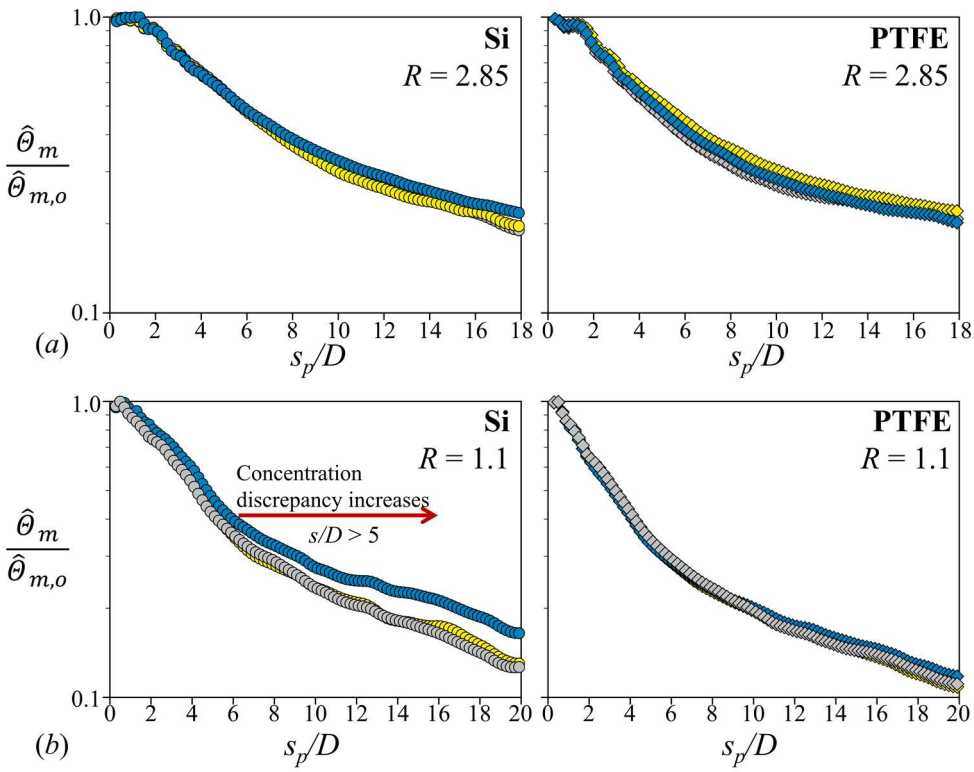

Figure 4.11. Particle concentration ($\hat{\Theta}_m$) decay at the particle concentration maxima lines (along s_p-axis) for Si and PTFE particles: (*a*) R = 2.85. (*b*) 1.1. In (a, b), Si particle: ●, $\bar{\Phi}_b = 0\%$ (RH = 30%); ● (yellow), $\bar{\Phi}_b = 0.014\%$ (RH = 50%); ●, $\bar{\Phi}_b = 0.03\%$ (RH = 70%) & PTFE particle: ♦, $\bar{\Phi}_b = 0\%$ (RH = 30%); ♦ (yellow), $\bar{\Phi}_b = 0.014\%$ (RH = 50%); ♦, $\bar{\Phi}_b = 0.03\%$ (RH = 70%).

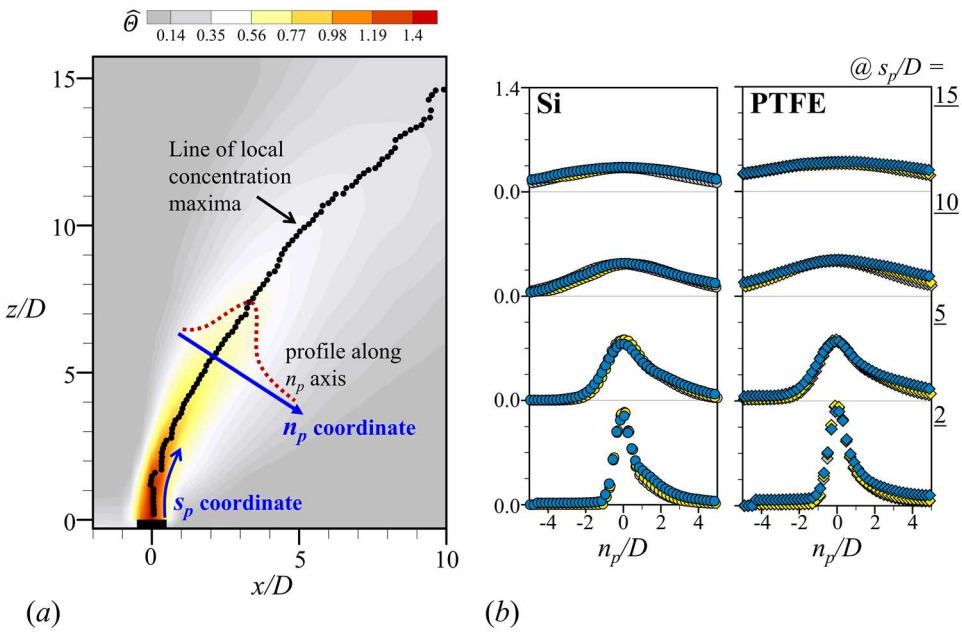

Figure 4.12. The particle concentration distribution ($\hat{\Theta}$) on the jet center-plane (side-view at $y/D = 0$) for $R = 2.85$: (*a*) $\hat{\Theta}$ contour for Si particles with $\bar{\Phi}_b = 0.03\%$ (RH = 70%). (*b*) $\hat{\Theta}$ profiles along the n_p axis at several s_p coordinates for both Si and PTFE particles. In (*a*), black circles denote the local concentration maxima line. The illustrations of s_p & n_p axes and a $\hat{\Theta}$ profile along the n_p axis at a specific s_p coordinate. In (*b*), Si particle: ●, $\bar{\Phi}_b = 0\%$ (RH = 30%); ● (yellow), $\bar{\Phi}_b = 0.014\%$ (RH = 50%); ●, $\bar{\Phi}_b = 0.03\%$ (RH = 70%) & PTFE particle: ♦, $\bar{\Phi}_b = 0\%$ (RH = 30%); ♦ (yellow), $\bar{\Phi}_b = 0.014\%$ (RH = 50%); ♦, $\bar{\Phi}_b = 0.03\%$ (RH = 70%).

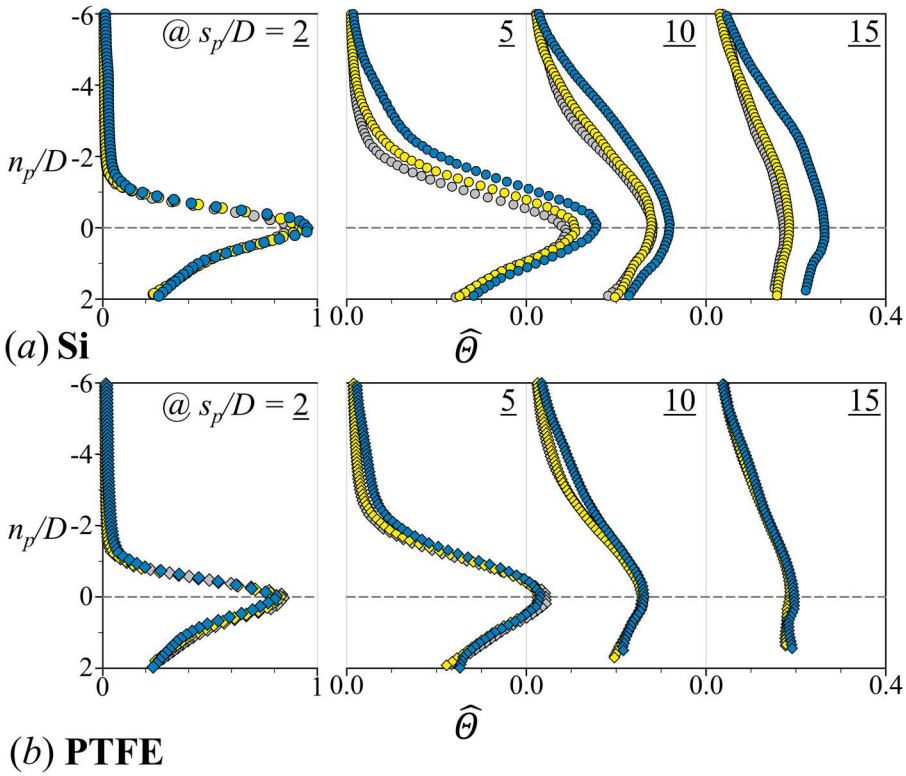

Figure 4.13. The Particle concentration ($\widehat{\Theta}$) profiles on the jet center-plane (side-view at $y/D = 0$) for $R = 1.1$ along the n_p axis at the several s_p coordinates ($s_p = 2$, 5, 10 and 15): (*a*) Si; ●, $\overline{\Phi}_b = 0\%$ (RH = 30%); ● (yellow), $\overline{\Phi}_b = 0.014\%$ (RH = 50%); ●, $\overline{\Phi}_b = 0.03\%$ (RH = 70%). (b) PTFE; ♦, $\overline{\Phi}_b = 0\%$ (RH = 30%); ♦ (yellow), $\overline{\Phi}_b = 0.014\%$ (RH = 50%); ♦, $\overline{\Phi}_b = 0.03\%$ (RH = 70%).

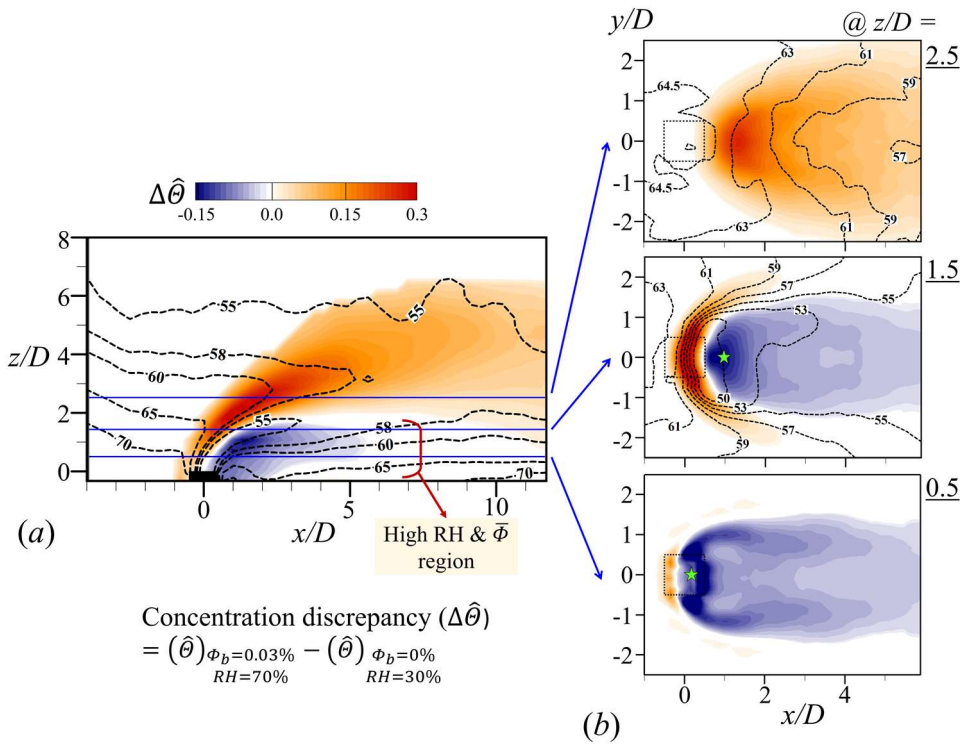

Figure 4.14. Si particle concentration discrepancy ($\Delta\hat{\Theta}$) contours on the (*a*) side-view (*y/D* = 0) and (*b*) several top-views (*z/D* = 0.5, 2.5 and 5.0). Dashed-line contours denote RH distributions of airflows. ★ denotes the location of jet center.

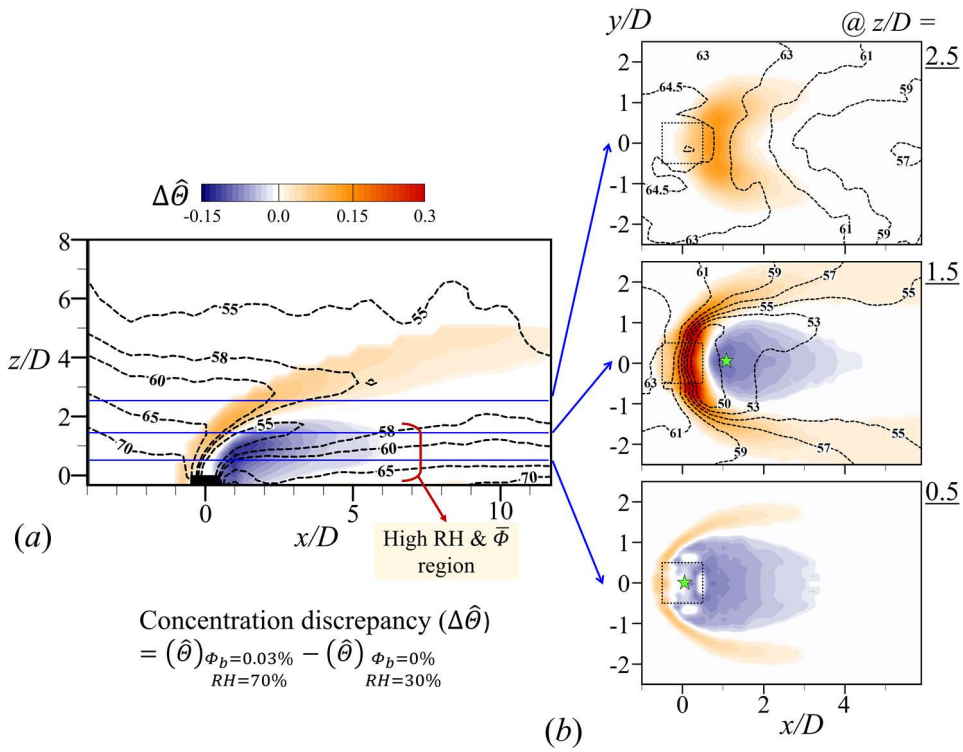

Figure 4.15. PTFE particle concentration discrepancy ($\Delta\hat{\Theta}$) contours on the (*a*) side-view (*y/D* = 0) and (*b*) several top-views (*z/D* = 0.5, 2.5 and 5.0). Dashed-line contours denote RH distributions of airflows. ★ denotes the location of jet center.

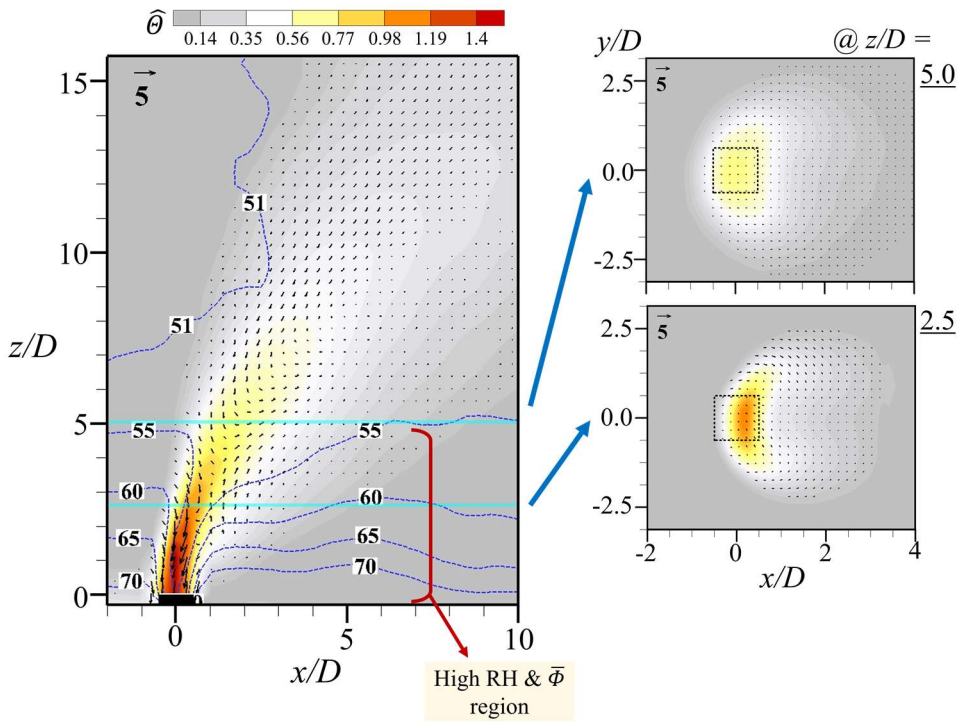

Figure 4.16. Si particle concentration contours with drag force ($\bar{F}''_{Drag}$) vectors on the jet center-plane (at *y/D* = 0) and x-y planes (at *z/D* = 2.5 and 5.0) for the case of *R* = 2.85 and $\bar{\Phi}_b = 0.03\%$ (RH = 70%). On the jet center-plane, the line contour denotes the RH distribution of the airflow.

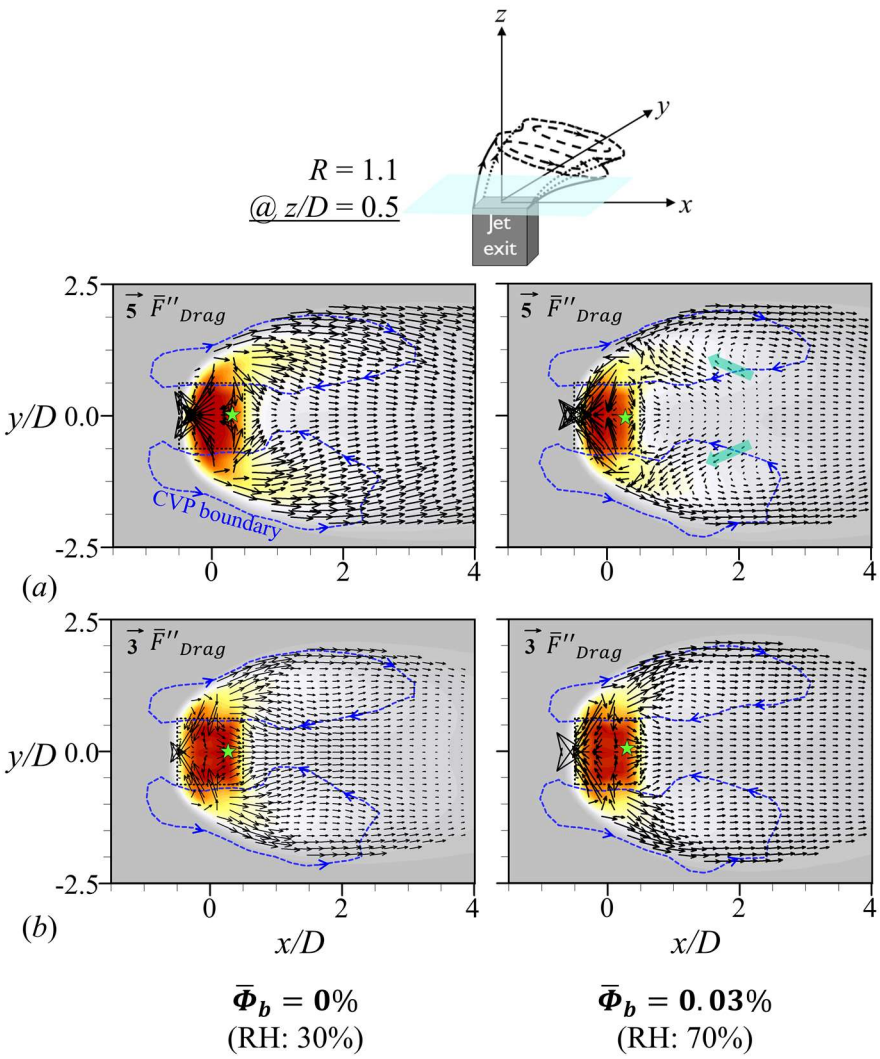

Figure 4.17. Particle concentration contours with drag force ($\bar{F}''_{Drag}$) vectors on an *x*-*y* plane at *z/D* = 0.5 for *R* = 1.1: (a) Si particle and (b) PTFE particle. In (a, b), lines denote an iso-$\bar{\omega}_z^*$ (5% of maximum $\bar{\omega}_z^*$ at each plane) distribution of airflow. ★ denotes the location of jet center.

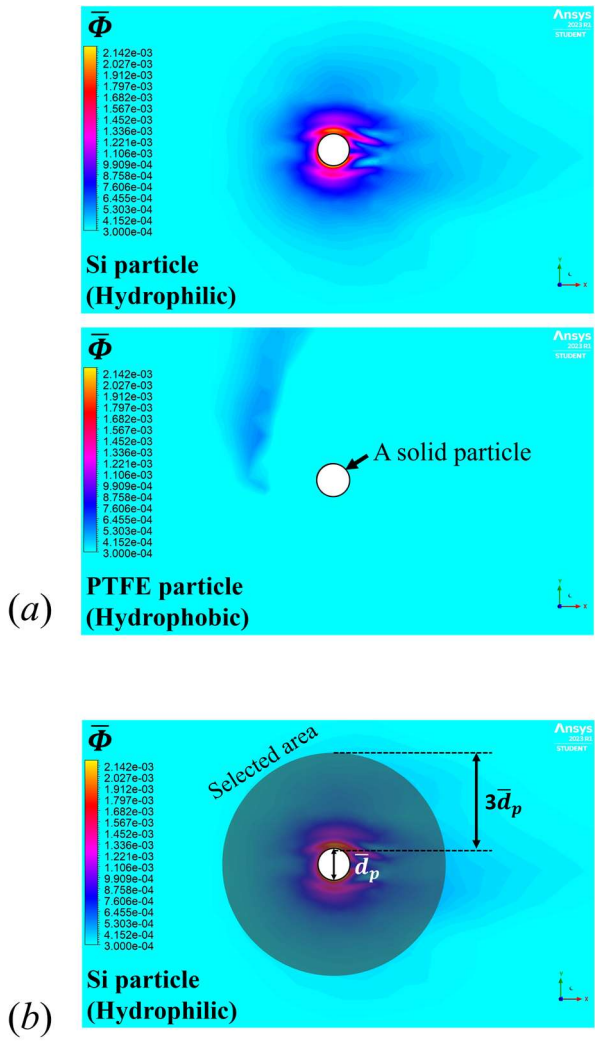

Figure 4.18. CFD (ANSYS-Fluent) for estimation of increased particle mass owing to the water droplet deposition on the particle surface: (a) liquid-phase (water droplet) volume fraction $\bar{\Phi}$ in the airflow around the Si and PTFE particles. (b) Selected area for calculation of water mass deposited on the Si particle surface.

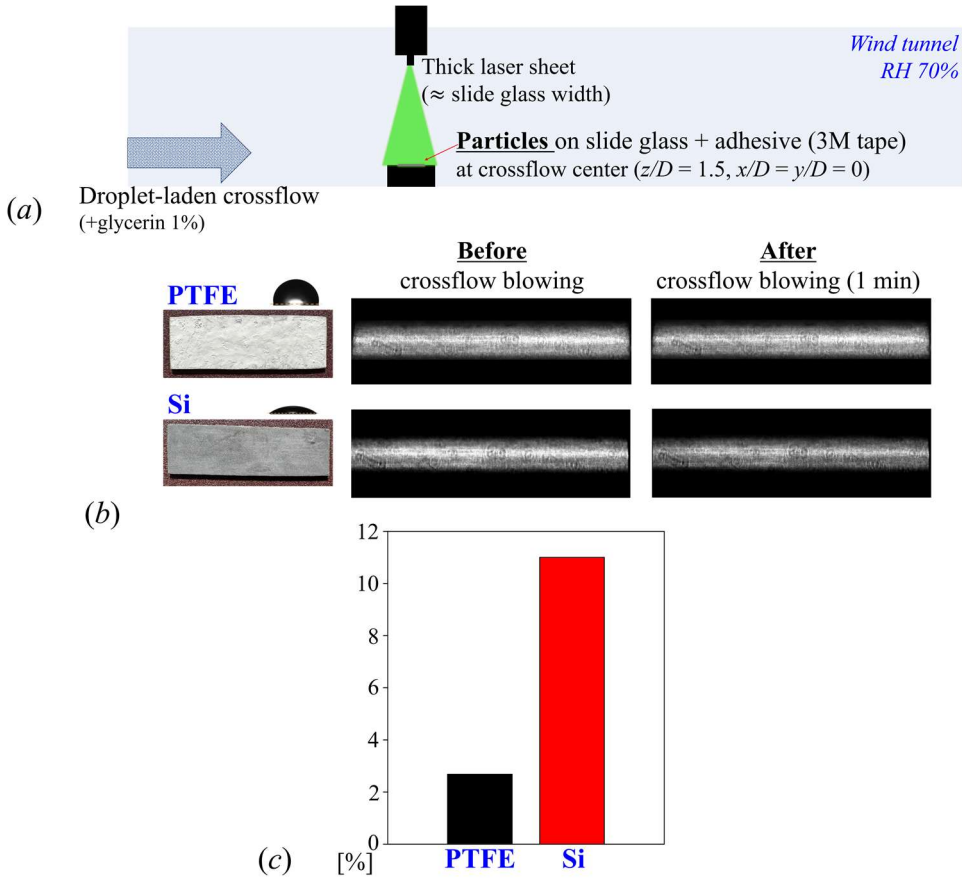

Figure 4.19. An experimental observation of contact between solid particles and mist droplets: (a) Test configuration. (b) Samples of the two particle types and obtained raw images. (c) Comparison of the light intensity reduction rate [%] between PTFE and Si particles.

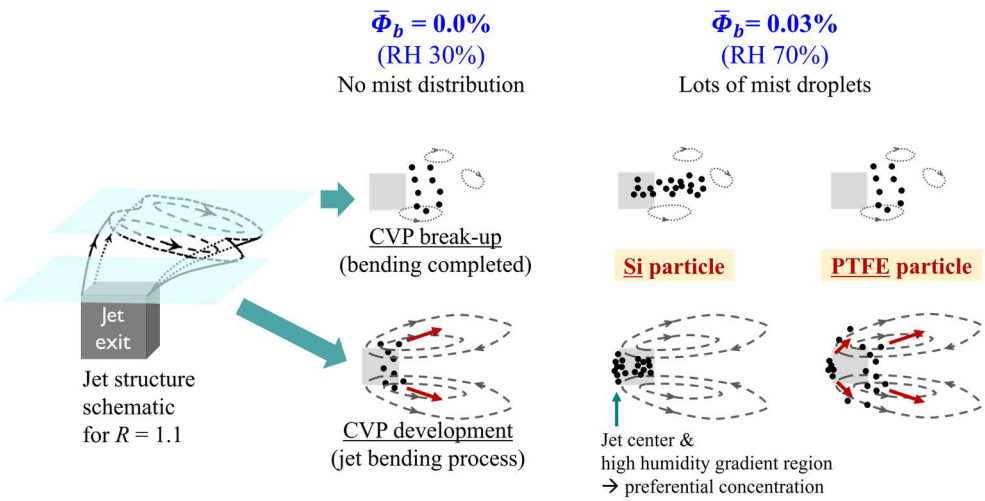

Figure 4.20. Schematics of Si and PTFE particle dispersion (in top-views) in the vertical jet with crossflow for R = 1.1 under two $\bar{\Phi}_b$ conditions: $\bar{\Phi}_b = 0\%$ (RH = 30%) & $\bar{\Phi}_b = 0.03\%$ (RH = 70%)

Chapter 5
Concluding remarks

In the present dissertation, the particle dispersion in a particle-laden jet with a crossflow was investigated experimentally, focusing on the particle inertia effect and airflow physical characteristics. In the experiments, we set the Stokes number, particle surface condition, airflow velocity ratio and mist droplet volume fraction in the airflow as variables and varied them over a wide range. In other words, this study provides a comprehensive understanding of the mechanisms by which solid particle dispersion patterns are determined within a particle-laden jet with crossflow, as well as methodologies for changing particle behavior as a function of particle surface conditions and airborne moisture content. The particle dispersion patterns resulting from these various experimental condition controls were measured optically using a high-speed camera and continuous laser, and then the particle dispersion characteristics were quantified using a series of image processing techniques. The jet flow structures and relative particle distribution levels were measured separately, using PIV and PN, respectively. They were analyzed together to understand their relations, including an estimation of the drag force distribution. In summary, the following two topics were discussed and analyzed based on the theories of fluid dynamics:

1. The particle dispersion mechanisms by various Stokes number and flow velocity ratios
2. The particle dispersion pattern change by mist droplets in the airflows

For the first topic (Chapter 3), we experimentally investigated particle-laden jets with and without crossflow (Re_D = 1170 – 5200) while varying the particle Stokes number (St = 0.01 – 27.42) and velocity ratio (R ~ 1.0 (strong crossflow) – ∞ (no crossflow)), and focusing on the subsequent changes in the particle dispersion pattern. The evolution of the jet flow structure from the jet exit, as represented by the deflected transverse vorticity with a strong CVP, are identified with respect to the velocity ratio. Together with the force variation caused by the vortex evolution (i.e. spatially varying coherency of the CVP) according to R and St, for the first time, we were able to classify three particle dispersion patterns caused by the large-scale vortical interaction. In regime 1 the particles reside quite longer in the jet-center plane even after the dissipation (lose of coherency) of CVP. In regime 2 the particles are dispersed along the lateral direction before the collapse of the CVP. Finally, in regime 3 the particles are confined in the vortex pairs, and are then transported outward as soon as the CVPs collapse. Because of the specific condition of partial crossflow, the CVP of the present study maintains its coherency in a short range, but the particle dispersion trend in relation to the dynamics of the CVP can be extended to the cases with full crossflow, with which the coherent CVP is retained for a longer distance. For each regime, we further developed empirical particle dispersion models to describe the effect of interactions with the CVP, which are expressed as a power law. The models are based on the standard deviation of concentration p.d.f. along the jet evolution on x–z (jet center) and x–y (cross-section of CVP) planes, respectively. These models support the particle dispersion regimes, a main contribution of the present study, to supplement the theoretical analysis of particle dispersion mechanisms depending on St and R.

Next, to observe the particle dispersion pattern change by water mist droplets, we experimentally investigated dispersion patterns of both hydrophilic (Si) and hydrophobic (PTFE) particles in the particle-laden jet with crossflow under three

mist droplet volume fraction in the crossflow (Chapter 4). To analyze the interaction of droplets and solid particles inside CVPs, which are complex vortical structures, experiments were performed for two different velocity ratios (R = 2.85 and 1.1) with CVPs of different characteristics. Stokes number and particle Reynolds number were set to be much less than 1 for both Si and PTFE particles. The airflow structure was not changed significantly with mist droplet volume fraction, but only in the higher velocity ratio case did the crossflow flux entrained into the jet decrease significantly at the highest droplet volume fraction where the RH went up to 70%. This resulted in a decrease in CVP size and, similarly, a slight decrease in CVP strength. However, despite this change in flow structure, the particle concentration decay rate along the particle concentration maxima line inside the jet was not affected by the mist droplet content in the air for both particle types. On the other hand, in the lower velocity ratio case, although the airflow vortical structure did not change with the increase of mist droplet volume fraction, the dispersion characteristics of hydrophilic particles altered. In other words, when the mist droplet loading in the air is large, the hydrophilic particles inside the jet change their drag direction towards the jet center due to contact with the droplets at the time of CVP formation; when there are no mist droplets in the air, the particles always receive drag force in the crossflow-streamwise direction regardless of the surface conditions. Therefore, most of the hydrophilic particles stay near the jet center and move downstream due to interaction with the droplets. Additionally, when the jet is fully deflected, a high humidity gradient region is formed on the windward side of the jet center, where both hydrophilic and hydrophobic particles are preferentially concentrated. Hydrophobic particles will eventually disperse along the transverse direction towards the region with a higher droplet volume fraction outside the CVP, but hydrophilic particles will not disperse outside the CVP and will remain in the high humidity gradient region. Therefore, hydrophilic particles continuously concentrate mostly in the jet center-

plane, and the resulting large amount of particles can be transported along the jet centerline for a long distance if the mist droplet fraction in the air is large. However, since PTFE particles are dispersed along the transverse direction from the upstream regardless of the presence of airborne droplets, it is not possible to change hydrophobic particle behavior through airborne mist droplets. To more directly verify the validity of our findings, we propose as future work to observe the interaction between micro-sized droplets and solid particles at very small scales, such as the Taylor micro-scale or Kolmogorov scale.

Although the movement of individual particles—which is outside the purview of this study—may not be covered by our findings, we believe that they are very helpful for comprehending and forecasting the long-term migration of particles in an open environment. For instance, it is possible to create physical models that may easily be utilized to monitor and estimate the location of the particle source based on the fundamental understanding of particle dispersion via coherent vortical structures in a complex geometry. It becomes more important to track the sources of contamination and estimate the propagations, which can be aided by the particle dispersion models developed in the present study, whether they are biological ones like germs or bacteria in confined situations or fine dust particles in open environments.

Bibliography

Abdelsamie, A. H. & Lee, C. 2012 Decaying versus stationary turbulence in particle-laden isotropic turbulence: Turbulence modulation mechanism. *Phys. Fluids* **24**, 015106.

Acarlar, M. & Smith, C. 1987 A study of hairpin vortices in a laminar boundary layer. Part 2. Hairpin vortices generated by fluid injection. *J. Fluid Mech.* **175**, 43-83.

Ahn, J., 2022 Large eddy simulation of film cooling: a review. *Energies* **15**, 8876.

Anderson, S. L. & Longmire, E. L. 1995 Particle motion in the stagnation zone of an impinging air jet. *J. Fluid Mech.* **299**, 333-366.

Andreopoulos, J. 1982 Measurements in a jet-pipe flow issuing perpendicularly into a cross stream. *J. Fluids Eng* **104**, 493-499.

Bagchi, P. & Balachandar, S. 2003 Inertial and viscous forces on a rigid sphere in straining flows at moderate reynolds numbers. *J. Fluid Mech.* **481**, 105-148.

Bassenne, M., Moin, P. & Urzay, J. 2018 Wavelet multiresolution analysis of particle-laden turbulence. *Phys. Rev. Fluids* **3**, 084304.

Birzer, C. H., Kalt, P. A. & Nathan, G. J. 2012 The influences of particle mass loading on mean and instantaneous particle distributions in precessing jet flows. *Int. J. Multiphas. Flow* **41**, 13-22.

Cecala, A. B., O'brien, A. D., Schall, J., Colinet, J. F., Fox, W. R., Franta, R. J. & Schultz, M. J. 2012 Dust Control Handbook for Industrial Minerals

Mining and Processing. Available at: https://stacks.cdc.gov.

Chauvat, G., Peplinski, A., Henningson, D. S. & Hanifi, A. 2020 Global linear analysis of a jet in cross-flow at low velocity ratios. *J. Fluid Mech.* **889**, A12.

Cheong, M., Birzer, C. & Lau, T. 2016 Laser attenuation correction for planar nephelometry concentration measurements. *Exp. Tech.* **40**, 1075-1083.

Chen, L., He, X., Liu H., Qian, L & Kim, S.H. 2018 Water adsorption on hydrophilic and hydrophobic surfaces of silion. *J. Phys. Chem. C* **122**, 11385-11391.

Choi, D. & Park, H. 2018 Flow around in-line sphere array at moderate reynolds number. *Phys. Fluids* **30**, 097104.

Coimbra, C. & Rangel, R. 1998 General solution of the particle momentum equation in unsteady stokes flows. *J. Fluid Mech.* **370**, 53-72.

Cortelezzi, L. & Karagozian, A. R. 2001 On the formation of the counter-rotating vortex pair in transverse jets. *J. Fluid Mech.* **446**, 347-373.

Dou, Z., Bragg, A. D., Hammond, A. L. Liang, A., Collins, L. R. & Meng, H. 2018 Effects of Reynolds number and Stokes number on particle-pair relative velocity in isotropic turbulence: a systematic experimental study. *J. Fluid Mech*. **930**, 271-292.

Elghobashi, S. 2006 An updated classification map of particle-laden turbulent flows. In proceedings of the IUTAM Symposium on Computational Multiphase Flow (ed. S. Balachandar & A. Prosperetti), Springer

Fellouah, H., Ball, C. & Pollard, A. 2009 Reynolds number effects within the development region of a turbulent round free jet. *Int. J. Heat Mass*

Transfer **52**, 3943-3954.

Ferreira, M. A. & Ganapathisubramani, B. 2020 PIV-based pressure estimation in the canopy of urban-like roughness. *Exp. Fluids* **61**, 1-13.

Fessler, J.R. & Eaton, J. K. 1997 Particle response in a planar sudden expansion flow. *Exp. Ther. Fluid Sci.* **15**, 413-423.

Fric, T. & Roshko, A. 1994 Vortical structure in the wake of a transverse jet. *J. Fluid Mech.* **279**, 1-47.

Fu, Y., Wang, T. & Gu, C. G. 2013 Experimental and numerical analyses of gas-solid-multiphase jet in cross-flow. *Proc. Inst. Mech. Eng. Part G-J. Aerosp. Eng.* **227**, 61-79.

Gibert, M., Xu, H. & Bodenschatz, E. 2012 Where do small, weakly inertial particles go in a turbulent flow? *J. Fluid Mech.* **698**, 160-167.

Goswami, P. S. & Kumaran, V. 2011 Particle dynamics in the channel flow of a turbulent particle–gas suspension at high stokes number. Part 1. Dns and fluctuating force model. *J. Fluid Mech.* **687**, 1-40.

Guha, A. 2008 Transport and deposition of particles in turbulent and laminar flow. *Annu. Rev. Fluid Mech.* **40**, 311-341.

Hickey, A. J. & Martonen, T. B. 1993 Behavior of hygroscopic pharmaceutical aerosols and the influence of hydrophobic additives. *Pharm. Res.* **10**, 1-7.

Hu, M., Peng, J. F., Sun, K., Yue, D. L., Guo, S., Wiedensohler, A. & Wu, Z. J. 2012 Estimation of size-resolved ambient particle density based on the measurement of aerosol number, mass, and chemical size distributions in the winter in beijing. *Environ. Sci. Technol.* **46**, 9941-9947.

Hwang, W. & Eaton, J. K. 2006 Homogeneous and isotropic turbulence modulation by small heavy ($St \sim 50$) particles. *J. Fluid Mech.* **564**, 361-393.

Izadi, T., Mehrabian, M. A., Sadrizadeh, S., Olofsson, U & Abouali, O. 2022 The effect of ventilation system with and without under-platform exhaust of the concentration of braking micro-particles inside the subway system. *Tunn. Undergr. Space Technol.* **128**, 104638.

Kalt, P. A., Birzer, C. H. & Nathan, G. J. 2007 Corrections to facilitate planar imaging of particle concentration in particle-laden flows using mie scattering, part 1: Collimated laser sheets. *Appl. Opt.* **46**, 5823-5834.

Kalt, P. A. & Nathan, G. J. 2007 Corrections to facilitate planar imaging of particle concentration in particle-laden flows using mie scattering. Part 2: Diverging laser sheets. *Appl. Opt.* **46**, 7227-7236.

Keffer, J. F. & Baines, W. D. 1963 The round turbulent jet in a cross-wind. *J. Fluid Mech.* **15**, 481-496.

Kelso, R. M., Lim, T. & Perry, A. 1996 An experimental study of round jets in cross-flow. *J. Fluid Mech.* **306**, 111-144.

Kibria, M. G., Zhang, F., Lee, T. H., Kim, M. J. & Howlader, M. M. R. 2010 Comprehensive investigation of sequential plasma activated Si/Si bonded interfaces for nano-integration on the wafer scale. *Nanotechnology* **21**, 134011.

Kim, N., Kim, H. & Park, H. 2015 An experimental study on the effects of rough hydrophobic surfaces on the flow around a circular cylinder. *Phys. Fluids* **27**, 085113.

Kim, M., Lee, J. H. & Park, H. 2016 Study of bubble-induced turbulence in upward laminar bubbly pipe flows measured with a two-phase particle image velocimetry. *Exp. Fluids* **57**, 55.

Kwon, S. J. & Seo, I. W. 2005 Reynolds number effects on the behavior of a non-buoyant round jet. *Exp. Fluids* **38**, 801-812.

Lau, T. C. & Nathan, G. J. 2014 Influence of stokes number on the velocity and concentration distributions in particle-laden jets. *J. Fluid Mech.* **757**, 432-457.

Lau, T. C. & Nathan, G. J. 2016 The effect of stokes number on particle velocity and concentration distributions in a well-characterised, turbulent, co-flowing two-phase jet. *J. Fluid Mech.* **809**, 72-110.

Lawson, N., Rudman, M., Guerra, A. & Liow, J.-L. 1999 Experimental and numerical comparisons of the break-up of a large bubble. *Exp. Fluids* **26**, 524-534.

Lee, J. & Park, H. 2020 Bubble dynamics and bubble-induced agitation in the homogeneous bubble-swarm past a circular cylinder at small to moderate void fractions. *Phys. Rev. Fluids*. **5**, 054304.

Levy, M. L., Carroll, W. & Izquierdo Alonso, J. L., Keller, C., Lavorini, F. & Lehtimäki, L. 2019 Understanding dry powder inhalers: key technical and patient preference attributes. *Adv. Ther.* **36**, 2547-2557.

Li, W. J., Shao, L. Y., Wang, Z. S., Shen, R. R., Yang, S. S. & Tang, U. 2010 Size, composition, and mixing state of individual aerosol particles in a south china coastal city. *J. Environ. Sci.* **22**, 561-569.

Liu, X., Jian, Y., Zhang, N. & Li, J. 2016 Gas penetrating flow through

dynamic particle clusters. *Powder Technol.* **297**, 409-414.

Liu, Y., Shen, L., Zamansky, R. & Coletti, F. 2020 Life and death of inertial particle clusters in turbulence. *J. Fluid Mech.* **902**, R1.

Longmire, E. K. & Eaton, J. K. 1992 Structure of a particle-laden round jet. *J. Fluid Mech.* **236**, 379-407.

Mahesh, K. 2013 The interaction of jets with crossflow. *Annu. Rev. Fluid Mech.* **45**, 379-407.

Marchioli, C. & Soldati, A. 2002 Mechanisms for particle transfer and segregation in a turbulent boundary layer. *J. Fluid Mech.* **468**, 283-315.

Martinez-Urrutia, A., Arroiabe, P. F., Ramirez, M., Marinez-Agirre, M. & Bou-Ali, M. M. Contact angle measurement for LiBr aqueous solutions on different surface materials used in absorption systems. *Int. J. Refrig.* **95**, 182-188.

Maxey, M. R. 1987 The gravitational settling of aerosol-particles in homogeneous turbulence and random flow-fields. *J. Fluid Mech.* **174**, 441-465.

Maxey, M. R. & Riley, J. J. 1983 Equation of motion for a small rigid sphere in a nonuniform flow. *Phys. Fluids* **26**, 883-889.

Mi, J., Nobes, D. S. & Nathan, G. J. 2001 Influence of jet exit conditions on the passive scalar field of an axismmetric free jet. *J. Fluid Mech.* **432**, 91-125.

Mi, J., Xu, M. & Zhou, T. 2013 Reynolds number influence on statistical behaviors of turbulence in a circular free jet. *Phys. Fluids* **25**, 075101.

Monchaux, R., Bourgoin, M. & Cartellier, A. 2010 Preferential concentration

of heavy particles: A Voronoï analysis. *Phys. Fluids* **22**, 103304.

Muppidi, S. & Mahesh, K. 2005 Study of trajectories of jets in crossflow using direct numerical simulations. *J. Fluid Mech.* **530**, 81-100.

Muppidi, S. & Mahesh, K. 2007 Direct numerical simulation of round turbulent jets in crossflow. *J. Fluid Mech.* **574**, 59-84.

Muppidi, S. & Mahesh, K. 2008 Direct numerical simulation of passive scalar transport in transverse jets. *J. Fluid Mech.* **598**, 335-360.

Namer, I. & Ötügen, M. 1988 Velocity measurements in a plane turbulent air jet at moderate reynolds numbers. *Exp. Fluids* **6**, 387-399.

Nathan, G. J., Mi, J., Alwahabi, Z. T., Newbold, G. J. R. & Nobes, D. S. 2006 Impacts of a jet's exit flow pattern on mixing and combustion performance. *Prog. Energy Combust. Sci.* **32**, 496-538.

Peterson, S. D. & Plesniak, M. W. 2002 Short-hole jet-in-crossflow velocity field and its relationship to film-cooling performance. *Exp. Fluids* **33**, 889-898.

Plesniak, M. W. & Cusano, D. M. 2005 Scalar mixing in a confined rectangular jet in crossflow. *J. Fluid Mech.* **524**, 1-45.

Plesniak, M. W. & Yi, J. 2002 Dispersion of a particle-laden air jet in a confined rectangular crossflow. *Powder Technol.* **125**, 168-178.

Poelma, C., Westerweel, J. & Ooms, G. 2007 *Particle Image Velocimetry: A Practical Guide.* Springer.

Pope, S. B. 2003 *Turbulent Flows.* Cambridge University Press.

Portuguez, E., Alzina, A., Michaud, P., Hourlier, D. & Smith, A. 2017 Study of the contact and the evaporation kinetics of a thin water liquid bridge

between two hydrophobic plates. *Adv. Mater. Phys. Chem.* **7**, 99-112.

Raffel, M., Willert, C. E. & Kompenhans, J. 2007 Particle image velocimetry: A practical guide. Springer-Verlag.

Reeks, M. 1983 The transport of discrete particles in inhomogeneous turbulence. *J. aerosol sci.* **14**, 729-739.

Rosenfeld, M., Kwak, D. & Vinokur, M. 1991 A fractional step solution method for the unsteady incompressible Navier-Stokes equations in generalized coordinate systems. *J. Comput. Phys.* **94**, 102-137.

Rubinow, S. & Keller, J. B. 1961 The transverse force on a spinning sphere moving in a viscous fluid. *J. Fluid Mech.* **11**, 447-459.

Saffman, P. 1965 The lift on a small sphere in a slow shear flow. *J. Fluid Mech.* **22**, 385-400.

Sakai, E., Takahashi, T & Watanabe, H. 2014 Large-eddy simulation of an inclined round jet issuing into a crossflow. *Int. J. Heat Mass Transf.* **69**, 300-311.

Sau, A., Sheu, T. W., Hwang, R. R. & Yang, W. 2004 Three-dimensional simulation of square jets in cross-flow. *Phys. Rev. E* **69**, 066302.

Sau, R. & Mahesh, K. 2008 Dynamics and mixing of vortex rings in crossflow. *J. Fluid Mech.* **604**, 389-409.

Schiller, L. & Neumann, A. 1933 Self-sustained oscillations in the wake of a sphere. *Zeit. Ver. Deut. Ing* **77**, 318-320.

Slater, S., Leeming, A. & Young, J. 2003 Particle deposition from two-dimensional turbulent gas flows. *Int. J. Multiphas. Flow* **29**, 721-750.

Smith, S. H. & Mungal, M. G. 1998 Mixing, structure and scaling of the jet

in crossflow. *J. Fluid Mech*. **357**, 83-122.

Squires, K. D. & Eaton, J. K. 1991 Preferential concentration of particles by turbulence. *Phys. Fluids* A **3**, 1169-1178.

Steinfeld, A. 2005 Solar thermochemical production of hydrogen - a review. *Sol. Energy* **78**, 603-615.

Su, L. & Mungal, M. 2004 Simultaneous measurements of scalar and velocity field evolution in turbulent crossflowing jets. *J. Fluid Mech.* **513**, 1-45.

Suresh, P., Srinivasan, K., Sundararajan, T. & Das, S. K. 2008 Reynolds number dependence of plane jet development in the transitional regime. *Phys. Fluids* **20**, 044105.

Swanson, J. –G. & Langefeld, O. 2012 Fundamental research in water spray systems for dust control. *Trans. Inst. Mining Met. A* **124**, 78–82.

Tagawa, Y., Mercado, J. M., Prakash, V. N., Calzavarini, E., Sun, C. & Lohse, D. 2012 Three-dimensional lagrangian voronoï analysis for clustering of particles and bubbles in turbulence. *J. Fluid Mech.* **693**, 201-215.

Tang, L., Wen, F., Yang, Y., Crowe, C., Chung, J. & Troutt, T. 1992 Self-organizing particle dispersion mechanism in a plane wake. *Phys. Fluids* A **4**, 2244-2251.

Tong, C. & Warhaft, Z. 1994 Turbulence suppression in a jet by means of a fine ring. *Phys. Fluids* **6**, 328-333.

Tóth, B., Anthoine, J. & Riethmuller, M. L. 2009 Two-phase PIV method using two excitation and two emission spectra. *Exp. Fluids* **47**, 475-487.

Vuorinen, V. & Keskinen, K. 2016 DNSlab: A gateway to turbulent flow simulation in Matlab. *Comput. Phys. Comm.* **203**, 278-289.

Wang, G., Zheng, X. & Tao, J. 2017a Very large scale motions and PM10 concentration in a high-re boundary layer. *Phys. Fluids* **29**, 061701.

Wang, X., Zheng, X. & Wang, P. 2017b Direct numerical simulation of particle-laden plane turbulent wall jet and the influence of stokes number. *Int. J. Multiphas. Flow* **92**, 82-92.

Wen, F., Kamalu, N., Chung, J. N., Crowe, C. T. & Troutt, T. R. 1992 Particle dispersion by vortex structures in plane mixing layers. *J. Fluids Eng.-Trans. ASME* **114**, 657-666.

Wen, Y., Leng, J., Shen, X., Han, G., Sun, L & Yu, F. 2020 Environmental and health effects of ventilation in subway stations: a literature review. *Int. J. Environ. Res. Public Health* **17**, 1084.

Westerweel, J. & Scarano, F. 2005 Universal outlier detection for piv data. *Exp. Fluids* **39**, 1096-1100.

Wood, A. M., Hwang, W. & Eaton, J. K. 2005 Preferential concentration of particles in homogeneous and isotropic turbulence. *Int. J. Multiphas. Flow* **31**, 1220-1230.

Xu, M., Pollard, A., Mi, J., Secretain, F. & Sadeghi, H. 2013 Effects of reynolds number on some properties of a turbulent jet from a long square pipe. *Phys. Fluids* **25**, 035102.

Ye, L., Liu, C. & Zhu, H. 2019 Experimental investigation on effect of cross-flow Reynolds number on film cooling effectiveness. *AIAA J.* **57**, 4804-4818.

Yu, H., Wu, C., Wu, D. & Yu, J. Z. 2010 Size distributions of elemental carbon and its contribution to light extinction in urban and rural locations in the

pearl river delta region, China. *Atmos. Chem. Phys*. **10**, 5107-5119.

Yuan, L. L. & Street, R. L. 1998 Trajectory and entrainment of a round jet in crossflow. *Phys. fluids* **10**, 2323-2335.

Zaichik, L. I. & Alipchenkov, V. M. 2005 Statistical models for predicting particle dispersion and preferential concentration in turbulent flows. *Int. J. Heat Fluid Flow* **26**, 416-430.

Zhang, D., Wang, W., Sun, H. & Bernitsas, M. M. 2021 Influence of turbulence intensity on vortex pattern for a rigid cylinder with turbulence stimulation in flow induced oscillations. *Ocean Eng*. **237**, 109349.

Zhang, J., Xu, M., Pollard, A. & Mi, J. 2013 Effects of external intermittency and mean shear on the spectral inertial-range exponent in a turbulent square jet. *Phys. Rev. E* **97**, 053009.

Zhong, H & Kotsonis, M. 2019 Effect of velocity ratio on the interaction between plasma synthetic jets and turbulent cross-flow. *J. Fluid Mech.* **865**, 928-962.

직교류 내 고체입자 포함 제트 유동에서의 입자 분산에 대한 실험연구

서울대학교 대학원
기계항공공학부
박주연(PARK JOOYEON)

요약

직교류 내 고체입자 포함 제트 유동은 제조 시설과 같은 산업 현장이나, 화산이나 화재 현장과 같이 자연에서도 흔히 발생하는 유체역학적 현상이다. 직교류 내 제트 유동 내에서는 복잡한 와류 구조들이 생성되기 때문에, 이러한 와류 구조에 의한 고체입자 분산 메커니즘에 대한 이해는 다양한 유형의 유동 구조들에 적용 가능하다. 본 연구에서는 제트 출구 근처에서 국부적으로 불어오는 직교류 내 고체입자 포함 제트 유동에 대해 와류 구조와의 상호작용을 통한 고체입자 분산(농도)를 실험적으로 관찰하였다. 요약하자면, 본 논문은 1) 직교류 내 고체입자 포함 제트 유동 내에서 발생하는 다양한 고체입자 분산 패턴들뿐만 아니라 2) 유동 내 미세 액적 함량에 따른 입자 거동 제어 방법론까지 포함한 '고체입자와 공기 유동 사이의 상호작용'에 대한 종합적인 분석으로 구성되어 있다. 먼저, 고체입자 분산 패턴과 분산 메커니즘들은 다양한 유동 속도비(제트/직교류 R = 1.0 – 3.5)와 입자 Stokes number(St = 0.01 – 27.42)에 대하여 관찰되었다. 직교류가 없을 때는, 수평 방향을 따라 지

배적인 와류 구조가 존재하지 않기 때문에 대부분의 입자가 수직방향으로 상승하며 제트 중심 밖으로 분산되지 않는다. 반면, 직교류가 있는 경우에는, 제트 출구 위에서 counter-rotating vortex pair (CVP)가 형성되며 CVP의 세기는 R이 감소할수록(제트가 더 꺾일수록) 증가한다. R이 작을수록 CVP에 의해 입자에 작용하는 항력의 크기가 증가하고, 특히, St가 1 미만으로 매우 작은 입자들은 이러한 항력이 입자 거동에 가장 중요하게 작용한다. 따라서, CVP가 발달하는 시기에 많은 양의 입자들이 CVP에 의해서 제트 중심 바깥으로 분산된다. St가 1에 가까운 경우에는, 항력 방향의 전환에 의해서 입자들이 CVP 내부 (특히 제트 중심)에 머물게 된다. 다양한 Stokes number와 R에 대해 관찰된 분산 패턴들은 최종적으로 3가지 유형으로 분류가 되었고, 분산 메커니즘들은 경험적 입자 분산모델까지 확장된다. 이러한 입자 분산 특성 규명 연구에 이어서, $St < 1$의 입자가 공기 중 미세 액적과 상호작용할 때 발생하는 입자 분산 특성 변화를 실험적으로 관찰하였다. 해당 실험에서는 친수성(Si)과 소수성(PTFE) 입자의 거동 변화를 직교류 내 다양한 미세 액적 부피분율 조건(0%, 0.014% & 0.03%)에 대하여 분석하였다. $R = 2.85$인 유동에서는 Si와 PTFE 입자 모두 미세 액적의 양과 관계없이 항상 일정한 거동 특성을 보였다. 높은 속도비의 유동에서는 jet 내부로의 적은 직교류 유량 때문에 약한 CVP가 발생하므로 입자들이 미세 액적과 상호작용할 확률이 현저히 낮아지기 때문이다. 반면에 $R = 1.1$인 경우, 유동 내 미세 액적 분율이 높을 때 Si 입자가 제트 중심쪽에 우위적으로 집중되어 먼 위치까지 분산되는 입자 양의 증가한다. 이러한 현상은 입자와 액적사이의 상호작용에 의하여 입자가 제트 중심쪽으로 항력을 받게 되어, CVP 외부로 거의 분산되지 않기 때문에 발생하는 현상이다. PTFE 입자는 낮

은 R의 유동에서도 미세 액적의 영향을 받지 않아 분산 특성이 변하지 않았다.

주요어 : 고체입자 포함 제트, 직교류, 와류 구조, 스토크스 수, 속도비, 습도

학번 : 2017-24246

Acknowledgements

During my six and a half years in the Multiphase Flow and Flow Visualization laboratory (MFFV Lab), I have learnt so much, not just academically, but also in all facets of my social life. I consider myself incredibly fortunate to have developed precious relationships.

Firstly, Professor Hyungmin Park. Thank you for giving me the opportunity to work in the MFFV Lab and guiding me to perform high-quality studies. I admire your leadership, paper direction, and insight, and I am much honored to have studied the field of 'multiphase flows' with you. I wouldn't have been able to have my work published where I desired without your support and helpful feedback, and I wouldn't have enjoyed my research as much. You have been and continue to be my role model since the beginning.

To Ph.D. alumni, Dr. NY Kim, JH Lee, LF Piao, HS Kim, JB Lee, BG Lee, JJ Lee and DH Choi. I am thankful to you for teaching me a variety of experimental techniques and lab life tips, as well as for keeping the ambiance in the lab always energetic. Your incredible integrity is a lesson to me, and the previous literature review meetings I attended with you were really beneficial to me. Furthermore, I will never forget the weight training, basketball, and soccer games we had together after work.

To Master alumni, HS Kim and HY Maeng. In the short period we spent together in the laboratory, we had so many moments of happiness. I was impressed by how hard you all worked on the challenging experiments. Also, I appreciate you for making me laugh every day with your humor.

YE Kang, a long-term collaborator on many studies. I was lonely in the

start of my 'particle-laden flow' research, but not with you. Thank you for following me attentively, and I enjoyed learning from you because you actively shared your thoughts. I believe it is difficult to be a lab chief and conduct research at the same time, but I am confident you will succeed. Best wishes for the future!

My ’94 friends, YW Kim, HS Choi, KS Choi and JE Yeo. I was very glad to share all of my emotions with you, both good and negative, when I was doing my study - thank you for your trustworthy conversations and assistance. We've been together for a long time and had our ups and downs, but I believe they've strengthened our bond. My graduation mate, Yewon. I am so happy I graduated with you. Let us strive to be better researchers in the future. Thank you for sticking by me despite my quirks, my friends.

To Ph.D. student members, JB Lee, JY Choi, HG Sung and HJ Lee. Continue to work as hard as you are now, and you will see the fruits of your labor when you receive your Ph.D. I have no doubt that you will continue to do well. You are the future of MFFV Lab, and I wish you all the best.

To master student members, JM Sim, DI Kim, JH Kim and DE Lee. To my lab mates who are just starting to realize research, I wish you all the best in your future, whether you go on to a Ph.D. course or not. Even though it was a short time, I had a lot of fun doing many lab activities with you and thank you for bringing such a vibrant energy to the lab.

New faces, EH Joo, HY Choi, MH Kang and WJ Jung. Even though you are just getting settled into the lab, I was really impressed with how hard you are working on your experiments, and I support your enthusiasm.

My family, who have always believed and supported me. Their constant financial and emotional support has enabled me to complete my PhD. I believe that my parents offered me unconditional love and raised me to be a

self-respecting person, which is why I was able to keep getting up when I felt unhappy or discouraged during my studies. Now I'm going to repay your affection.

Lastly, my husband, Gervasius Jo, for inspiring me to go to graduate school. I am someone who receives a lot of energy from other people, and you have always been a source of positive energy for me. Thank you for being my biggest supporter, as is my family. I am extremely fortunate to have you as my husband. I would also like to thank my in-laws, who love everything about me.